공학박사 학위논문

# Study on Optical Properties and Chiral Sensing Mechanisms of Two-Dimensionally Aligned Chiral Nanoparticles for Biomolecules

## 2차원 정렬된 카이랄 나노 입자의 광학 특성과 그를 이용한 생체분자 카이랄성 센싱 메커니즘 분석

2023년 8월


서울대학교 대학원

재료공학부

김 령 명

# Study on Optical Properties and Chiral Sensing Mechanisms of Two-Dimensionally Aligned Chiral Nanoparticles for Biomolecules

지도 교수 남 기 태

이 논문을 공학박사 학위논문으로 제출함

2023년 8월

서울대학교 대학원

재료공학부

김 령 명

김령명의 박사 학위논문을 인준함

2023년 8월

위 원 장 김 미 영 (인)

부위원장 남 기 태 (인)

위 원 이 명 재 (인)

위 원 박 성 규 (인)

위 원 유 은 아 (인)

# Abstract

# Study on Optical Properties and Chiral Sensing Mechanisms of Two-Dimensionally Aligned Chiral Nanoparticles for Biomolecules

Ryeong Myeong Kim

Department of Materials Science and Engineering

The Graduate School

Seoul National University

Ultra-sensitive detection and precise characterization of molecular chirality has been important issue in broad range of fields including biology, physics, chemistry, and even pharmaceutics due to their ability to guide and control various phenomena in nature[1–6]. Understanding on specific light-matter interactions of chiral biomolecules with polarized have advanced spectroscopic techniques to analyze such interactions by measuring chirality-dependent transmission, absorption, and scattering[7–19]. Representatively, circular dichroism (CD) which measures absorption difference between left circularly polarized (LCP) and right circularly polarized (RCP) light[13–17] and optical rotatory dispersion (ORD)[7,9,11,20] which analyze rotation of initial optical axis have been demonstrated as non-invasive and simple detection techniques for molecular chirality. However, large scale mismatch between few-nm

sized molecules and hundreds-nm scale light which diminishes strength of light-matter interactions decrease the limit-of-detection for molecular chirality[21,22].

Recent advances in nanophotonic chiral sensing systems which utilize localized surface plasmon resonance (LSPR) of the chiral plasmonic materials have been demonstrated as it can concentrate the chiral energy of light (*i.e.,* optical helicity density) to the molecular scale to boost up light-matter interactions and CD response of molecules[8,23–55]. Even they successfully lowered the limit of detection for molecular chirality, the lack of mechanistic understanding and low sensitivity due to the weak and non-uniform enhancement of optical helicity density by chiral plasmonic structures results in reproducibility issues and ultimately limits the practical utilization of nanophotonic chiral sensing platforms[21,22,56]. Therefore, mechanistic investigation on nanophotonic chiral sensing and development of chiral nanostructure which can uniformly amplify optical helicity density is important for real application of nanophotonic systems for chirality detection. Through this study, we propose that the utilization of collective resonance (CR)[57,58] from two-dimensionally (2D) aligned chiral plasmonic nanoparticles (helicoids[59–66]), 2D helicoid crystal, and monitoring change in CD response of 2D aligned chiral plasmonic nanostructures depending on molecular chirality can be a promising strategy to solve above mentioned limitations. In this thesis, we present a new chiral sensing platform that can greatly amplify chiral light-matter interactions to the level of naked-eye chirality detection using plasmonic coupling (*i.e.,* CR) among helicoids and chiral perturbation theory that can interpret principle of nanophotonic chiral sensing through the understanding on chiral-light matter interactions in terms of energy re-distribution[67,68].

Recent development of strategy to colloidally synthesize helicoids with tailored chiroptic properties using biomolecules paves the way to practically utilize

the chiral plasmonic nanostructures for various applications[59–67,69–90]. In addition, the chiroptic property of a colloidal chiral plasmonic particle which came from LSPR of nanoparticles can be amplified and tailored by using coupled resonance among nanoparticles[57,58,85,88,91–93]. As a representative method for amplified plasmon resonance, 2D aligning plasmonic nanoparticles with a period of incident light wavelengths can induce hybridization between LSPR and diffraction mode, which can induce collective resonance of nanoparticles[57,58]. To establish new strategies for amplifying chiroptic response of existing helicoids, we have first developed methodology for 2D aligning colloidal nanoparticles and studied collective resonance feature of 2D helicoid crystal in Chapter 2. Importantly, study on the hybridization tendency depending on the energy level of LSPR and diffraction mode provide an important insight in achieving optimal chiroptic response in 2D helicoid crystal. Chapter 3 describes the simulational and theoretical study on chiroptical property of 2D helicoid crystal as a chiral sensing platform, Chapter 4 describes molecular chirality sensing experiment using collective resonance of 2D helicoid crystal, and Chapter 5 describes the 2D helicoid crystal for practical chiral sensing platforms from the perspectives of universal analyte selection and integration in commercialized optic system as a sensor chip.

Recent studies on 2D aligned plasmonic nanoparticles revealed new mode of plasmonic resonance called collective resonance[57,58] which originates from the mode hybridization between diffraction and LSPR. Specifically, diffracted light by periodic nanostructures is guided and induces collective excitation of plasmon of periodically spaced plasmonic nanoparticles. The collective resonance exhibits improved quality in plasmon resonance, enabling effective confinement of incident light along 2D surface and thus is considered useful strategy to boost up light-matter interactions and improve sensitivity of plasmonic sensors. However, the collective resonance and resulting CD response in 2D aligned chiral plasmonic nanostructures

is in realm of unknown due to the hardness in fabrication of 2D and periodically aligned chiral plasmonic nanostructures. In this thesis, we have developed methodology to 2D align colloidally synthesized helicoids and analyzed CD response of the fabricated nanostructure for effective confinement of chiral field of light (optical helicity density). The simple and easy control of collective resonance feature which originates from mode hybridization between LSPR and diffraction mode enabled generation of collective resonance mode which can induce strong chiroptic response in 2D helicoid crystal. Specifically, 180-nm sized helicoids aligned with 400 nm periodicity showed optimal chiroptic response at the 60-deg slanted incidence of circularly polarized light (CPL). These results revealed that the chiral counterpart of collective resonance can be induced and chiroptic response of chiral nanoparticles can be improved through the mechanistic control of collective resonance by tailoring mode hybridization between LSPR and diffraction mode.

Chiral plasmonic nanostructures as a chiral sensing platform has been studied for decades [8,23–50,94]. Existing studies on the chiral plasmonics for chiral sensor focus on the enhancement of molecular CD by improved optical helicity by chiral plasmonic nanostructures. However, the mere enhancement of optical helicity density by chiral plasmonic nanostructures and spectral mismatch between molecular CD and plasmon resonance wavelengths yields reproducibility issues in sensor properties[21,22]. In this thesis, strong chiroptic response and resulting optical helicity density of 2D helicoid crystal were explored for application of 2D helicoid crystal as ultra-sensitive chiral sensing platform. The chiroptic properties of helicoids, which have nearly isotropic (*i.e.,* 432 rotational symmetry[80]) chiral morphology, are sustained even in 2D aligned geometry by inducing overlap of transverse electric (TE) and transverse magnetic (TM) mode at the collective resonance wavelengths. In addition, the circular polarized light (CPL)-like phase difference of TE/TM mode was identified by electromagnetic (EM) simulation

which results in real-time spinning of optically induced electric dipole of each helicoids in 2D helicoid crystal. Furthermore, these collective spinning of electric dipole induced collective spinning of scattered electric field along the surface where the helicoids are 2D aligned, demonstrating that the collective resonance of 2D helicoid crystal generates uniform chiral scattered field (*i.e.,* uniform and strong optical helicity density). In order to practically apply uniform and strong optical helicity density for chiral sensing, new theory of chiral perturbation which can correlate molecular chirality and optical helicity density not in terms of molecular CD enhancement but for the chiral molecular energy back-action on CD response of chiral plasmonic nanostructures. These results robustly support that the uniform and strong optical helicity of 2D helicoid crystal is key factor for sensitive chiral sensing since they can enhance chiral light matter interaction, leading to increased chiral back-action of molecules to plasmonic structures.

Current research on chiral sensing by chiral plasmonic nanostructures has been theoretically demonstrating sensor characteristics due to issues in reproducibility, rather than providing experimental evidence of these sensor properties[21]. When the molecular orientation, local concentration and position are varies, the resulting optical responses differ. In this context, we experimentally confirmed reliability of the newly developed theoretical interpretation on chiral sensing based on 2D helicoid crystal. In this thesis, we demonstrated enantioselective CD response of 2D helicoid crystal for amino-acids, proline molecules. In order to induce collective resonance in 2D helicoid crystal, transmission-based optical sensing set-up which can monitor real-time CD response of 2D helicoid crystal for the introduction of L- and D-proline molecules was utilized. Through this, we confirmed that the collective CD response including wavelengths and intensity enantioselectively changes depending on the chirality of proline molecules. In addition, the degree of change in CD response was maintained for various

concentration and volume of proline molecules, reaching the limit of detection to few-mM and few-μL range. Furthermore, the enantioselective CD response results in enantioselective change in polarization resolved color[65] of 2D helicoid crystal, facilitating naked-eye determination of molecular chirality.

The strong and uniform optical helicity density of 2D helicoid crystal enabled detection of chirality changes, accompanied in DNA-RNA hybridization and protein conformation changes on 2D helicoid crystal. In this thesis, the expandability and practical applicability of collective CD of 2D helicoid crystal for the detection of various types of biomolecules such as microRNA (mRNA) and protein complexes. In order to conduct chiral sensing experiment on mRNA and protein complexes, each biomolecule were fixed on the 2D helicoid crystal using the specific bio-molecular interactions and the change in collective CD was monitored when the structure of each biomolecules is changed by attaching the binding counterparts such as, DNA and protein structure change inducers. Through this, we confirmed that the collective CD response including wavelengths and intensity changes when the chirality of mRNA and protein complexes alter, confirming enantiosensitivity of 2D helicoid crystal regardless of types of molecules. Furthermore, the 2D helicoid crystal was integrated into commercialized surface plasmon resonance (SPR) sensing systems, which uses reflection-type optic system, showing collective CD response and their enantioselective CD changes.

In conclusion, fabrication of 2D helicoid crystal and characterization of collective resonance and CD for the chiral sensing platform has been achieved in the perspective of experiment, simulation, and theory. In addition, integration of newly discovered structure, chiroptic responses, and theory for the detection of molecular chirality including, amino-acid, nucleotide, and proteins has been demonstrated in various sensing systems using micro volume of analyte, transmission, and reflection.

We believe the development of new system of chiral plasmonic nanoparticles for the detection of molecular chirality ultimately opens new paradigm of chiral plasmonic structures for real and practical chiral sensing applications.

**Keywords: Chirality, 2D aligned chiral plasmonic nanoparticles (2D helicoid crystal), helicoids, 432 symmetry, circular dichroism, collective resonance, collective circular dichroism, optical helicity densitiy, chiral perturbation theory.**

**Student Number: 2018-28151**

# Contents

# List of Figures

# List of Table

# Chapter 1. Introduction

## 1.1 Importance of Chirality

Chirality generally refers to the structural property of objects that are not superimposable on their mirror image. Chirality exists in a wide range of domains within the natural world, not only in biomolecules but also in many other areas. Representative examples of chiral biomolecules include amino acids, DNA, and proteins. Specifically, the chirality of a molecule arises from the arrangement of three different molecules seen from an axis defined by a central carbon atom or a molecular group that is tetrahedrally distributed (Figure. 1.1)[95]. When this arrangement exhibits a mirror-image configuration that cannot be superimposed through simple rotations, translations, or transformations, it signifies the presence of chirality. The chirality of molecules serves as an important indicator for inducing unique interactions in the natural world. These distinctive interactions of chiral molecules not only induce energetically preferred bindings based on the chiral nature of the interacting substances in organic-organic interactions but can also extend to organic-inorganic interactions. Chirality can influence interactions at scales beyond the molecular level, including DNA, proteins, organisms, and even the hands of living organisms (Figure 1.1)[96]. A notable example of the specific chirality-mediated interactions in biological systems can be observed during the developmental process of the shell in *L. stagnalis*[97], where the chirality of the formed inorganic structures is influenced by the chiral nature of the molecules present during the cellular expression stage (Figure 1.2). While it may be challenging to discern the impact of chirality in the early stages composed of a small number of molecules, the manifestation of molecular chirality begins from the eight-cell stage, leading to the twisted forms at the cellular level. Furthermore, this cellular-level chirality ultimately results in the helical shape of the fully grown snail shell, visually exhibiting both its own chirality and the initial molecular chirality.

In summary, chirality plays a significant role in various domains of the natural world, influencing unique interactions and phenomena. Understanding and studying the manifestations and effects of chirality contribute to advancing our knowledge in fields such as chemistry, biology, materials science, and beyond.

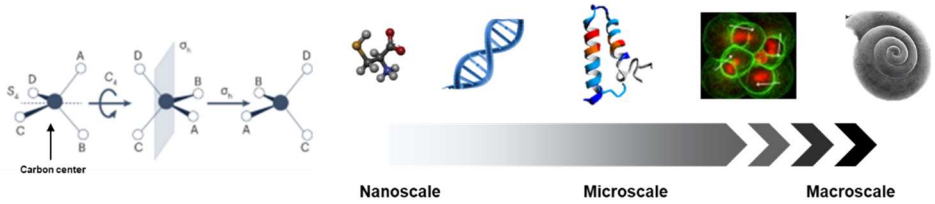


Figure 1. 1 Illustration of diverse biological molecules and substances in nature demonstrating chirality. This unique property is ubiquitous across different scales, ranging from nanoscale molecular structures up to macroscale entities.

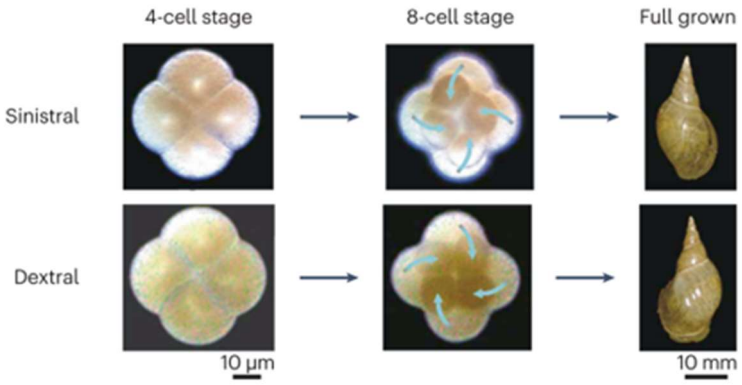


Figure 1. 2 Structural development of *L. stagnalis* as a case study, where the chirality of the inorganically formed structures is directly impacted by the chiral nature of the biomolecules present during the cellular expression stage.

In addition, it is worth noting that the development of chiral structures, facilitated by the presence of molecular chirality, can give rise to intriguing optical phenomena in the visible light range, particularly when these structures are composed of highly optically active molecules. One illustrative example can be found in certain species of butterflies, such as *Heliconius cydno* and *H. melpomene malleti*[98], which exhibit intricate chiral patterns on their wings. These regular chiral arrangements impart distinct polarization-dependent interactions with incident light, leading to variations in the reflection and absorption properties depending on whether the light is left-handed or right-handed circularly polarized (Figure 1.3). Consequently, these butterflies exhibit vibrant colors that can be visually discerned based on their chiral characteristics. Importantly, the structural chirality displayed by these organisms is not confined to mere optical peculiarities, but it is also believed to play a significant role in communication and object recognition within their respective ecosystems. Thus, the impact of chirality in biological systems extends beyond its fascinating optical attributes, as it is increasingly recognized as a fundamental element influencing diverse aspects of living organisms' activities and behaviors.

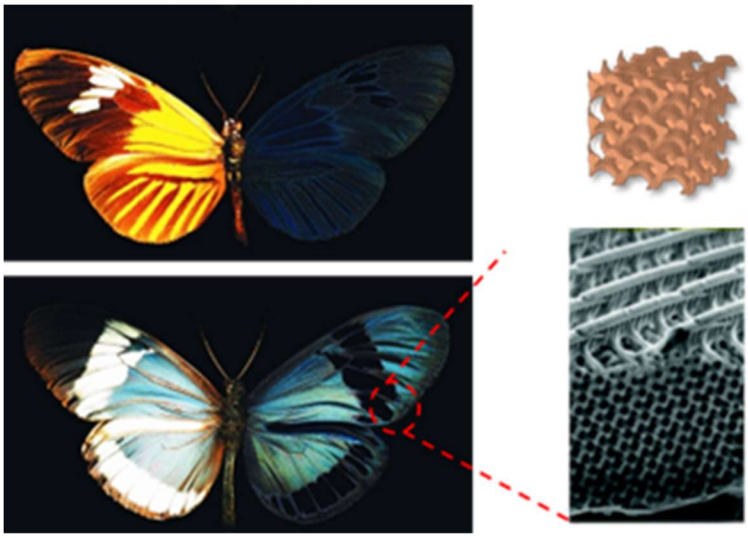

Figure 1. 3 Comparative display of the polarized iridescent patterning observed in the butterfly species, *Heliconius cydno* (left-top), juxtaposed with its counterpart, *H. melpomene malleti* (left-bottom), which distinctly lacks polarized iridescence in its wing structure. Schematic illustrations and Scanning Electron Microscope (SEM) image of chiral structures of exoskeletons in butterfly wings (right).

The understanding of chirality in living organisms has extended to the comprehension of biological phenomena and behaviors, leading to advancements in various fields encompassing optics, pharmacy, life sciences, and chemistry, with the aim of beneficially applying chirality for humanity[3,4,15]. However, as exemplified by the case of thalidomide in the late 1900s, the lack of accurate analysis of chirality and a precise understanding of chiral interactions within organisms resulted in tragic consequences[99]. Thalidomide was generally known as a drug molecule used for the treatment of morning sickness and sleep disorders in pregnant women. However, depending on its chirality, (R)-thalidomide served its intended role as a therapeutic agent, while (S)-thalidomide caused unexpected birth defects in babies (Figure 1.4)[4]. Thalidomide is not the only molecule in pharmaceuticals that exhibits chirality; about 60 % of drug molecules possess chirality (Figure 1.5)[4]. Through such cases, the significance of chirality in pharmacy has been emphasized, and it has become increasingly important to understand the precise chirality of molecules and their chiral interactions within living organisms when utilizing them as drugs.

As evident from these examples, the understanding of chirality extends beyond simple molecular chirality to the regulation of biological phenomena and behaviors. Its importance continues to grow, leading to an increasing demand for the accurate analysis of chirality and the development of techniques to synthesize desired forms of chiral molecules that can be precisely tailored to control biological phenomena and behaviors.

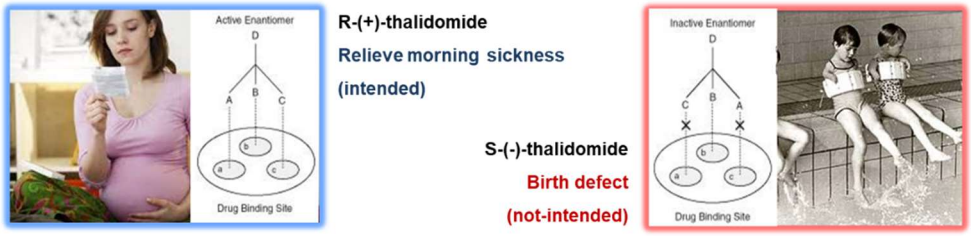


Figure 1. 4 A schematic illustration showcasing the profound influence of chirality on the biological impact of Thalidomide. (R)-Thalidomide functions as an effective remedy for morning sickness in pregnant women, while its mirror image, (S)-Thalidomide, induces teratogenic effects leading to congenital malformations in neonates.

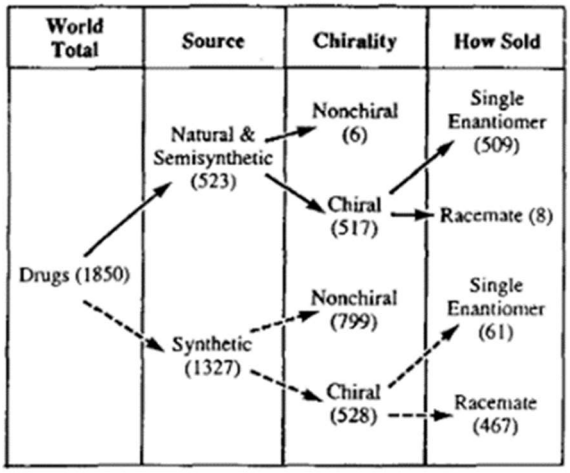


Figure 1. 5 A chart illustrating the proportion of currently prescribed drugs that exhibit chirality. This graph underscores the significant role that chirality plays in modern pharmaceuticals, with a high percentage of drugs demonstrating this characteristic.

## 1.2 State of Art for Chirality Determination

As noted in Chapter 1.1, chiral materials exhibit unique interactions with polarized light, displaying distinctive polarization colors or inducing changes in absorption and optical signals. These characteristics depend on the size and type of the structure, determining how they interact with different wavelengths of light and the extent of their interaction, which can be used as an indicator for determining the chirality of biomolecules. In the following section, we will discuss the analysis of chiral biomolecules using the polarization-specific interactions of chiral structures and recent research to enhance these interactions.

The analysis of chirality has commonly relied on their polarized-specific interactions. Substances with chiral structures exhibit different interactions depending on the arrangement of their structures, causing fluctuations in the flow of electrons when incident circularly polarized light possesses a certain directionality [7–18]. This led to the development of circular dichroism (CD), which analyzes the difference in absorption induced by left- and right-circularly polarized light when investigating chiral molecules. Additionally, chiral molecules exhibit optical activity, where they possess a rotatory power that can rotate the polarization axis when illuminated with linearly polarized light consisting of equal amounts of left- and right-circularly polarized components. Based on this phenomenon, optical rotatory dispersion (ORD) has been used, which analyzes the rotation induced by chiral molecules and determines the magnitude of rotation to assess the chirality of molecules (Figure 1.6). Both methods provide convenient and rapid detection of molecular chirality. However, they require short wavelengths of light to be used, corresponding to the size of the molecules, in order to enhance their interactions. This necessitates high concentrations of molecular samples and long measurement times[22]. Moreover, as

the wavelength of light decreases, the energy of the light increases, potentially causing damage to molecules that receive high-energy light over an extended period. Therefore, CD and ORD-based analyses are nearly impossible for molecules with limited quantities, such as important new drugs in actual drug development projects, as these methods do not allow for the recovery of the molecules after chirality analysis. Therefore, strategy that can enhance the interaction between molecules and incident circularly polarized light can overcome the limitations of existing chiral sensing techniques.

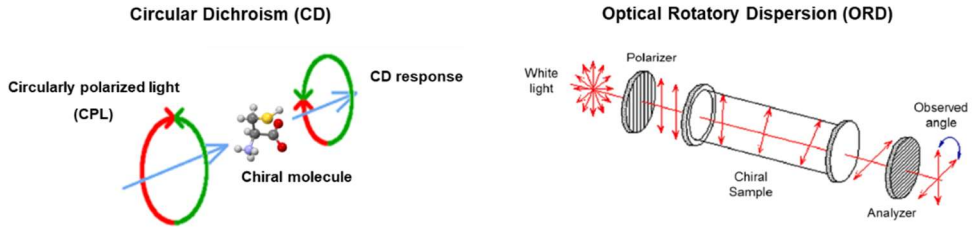


Figure 1. 6 Schematic illustration showing the fundamental principles of circular dichroism (CD) and optical rotatory dispersion (ORD).

To achieve this, the physical description of the interaction between chiral molecules and circularly polarized light was explored. The *Cohen* group re-examined the physical equation (Eq 1. 1) originally known as a simple conservation quantity of light, discovered by *Lipkin* in 1964[50], and revealed its significance as *optical helicity density* (*h*) (also known as *optical chirality* (*C*)), which represents how helical and intense the light is formed in the presence of molecules[8].

$$h = -\frac{\varepsilon 0}{2\omega} Im(\mathbf{E} \cdot \mathbf{H}^*) \propto |\mathbf{E}|\left|\mathbf{H}_{\boldsymbol{\pi/2}}\right|\left|cos\theta_{\mathbf{E},\boldsymbol{H\pi/2}}\right|, \qquad \text{(Eq 1. 1)}$$

Specifically, for circularly polarized light rotating in a specific direction, an electric field and a magnetic field with a phase difference of π/2 nearly exist in a parallel state (Figure 1.7). The imaginary operator in Eq 1. 1 has an effect of shifting the magnetic field term of the equation by π/2. Therefore, Eq 1.1, discovered by *Lipkin*, can be considered a quantity indicating how closely the polarization formed in a vacuum resembles circularly polarized light. Along with the invention of the optical helicity concept, the induction of molecular dipole moments was achieved to physically describe the chiral-specific interaction of molecules under the irradiation of circularly polarized light. Most molecules can form dipole moments due to the vibration of electrons under light irradiation as shown in Eq 1. 2, $\mathbf{p}$ and $\alpha$ denotes electric dipole moment and electric polarizability, respectively[100].

$$\mathbf{p} = \alpha\mathbf{E}, \qquad \text{(Eq 1. 2)}$$

For chiral molecules, when illuminated with circularly polarized light, their dipole moments can be expressed with the introduction of a chiral polarizability (*G*) term (Eq 1. 3)[101,102], and the light-dependent absorption of molecules based on this dipole moment can be represented as shown in Eq 1. 4. Simplifying the calculation of the actual measured CD signal of molecules based on Eq 1. 4 yields Eq 1. 5.

$$\mathbf{p} = \alpha\mathbf{E} + iG\boldsymbol{H}, \quad \text{(Eq 1. 3)}$$

$$A_{\pm(LCP,\ RCP)} = \langle \mathbf{E}^* \cdot \mathbf{p} + \mathbf{H}^* \cdot \mathbf{m} \rangle = \frac{1}{2}\{\alpha|\mathbf{E}|2 + 2G\mathrm{Im}(\mathbf{E} \pm \cdot \mathbf{H}^* \pm)\}, \quad \text{(Eq 1. 4)}$$

$$\Delta A(CD) = A_+ - A_- \propto G\{\mathrm{Im}(\mathbf{E}_+ \cdot \mathbf{H}^*{}_+) - \mathrm{Im}(\mathbf{E}_- \cdot \mathbf{H}^*{}_-)\}$$

$$= -\frac{2\omega G}{\varepsilon 0}(h_+ - h_-), \quad \text{(Eq 1. 5)}$$

The *Cohen* group focused on the Im(**E**·**H**$^*$) term present in Eq 1. 5 and demonstrated that the molecular CD ($CD_{molecule}$) and the dissymmetry factor (*g*-factor), which describes absolute chiroptic response of chiral structures, can be summarized in terms of optical helicity (Eq 1.6). Therefore, amplifying optical helicity can enhance the CD signal of molecules and establish a physical basis for lowering the detection limit of conventional chiral sensing techniques.

$$g_{molecule} = 2\frac{A_+ - A_-}{A_+ + A_-} = -\frac{4\omega G}{\varepsilon 0}(h_+ - h_-) =$$

$$-\frac{8\omega G}{\varepsilon 0}h_+ \quad (\because\ h_+ = h_+ - h_- \text{ for CPL}), \quad \text{(Eq 1. 6)}$$

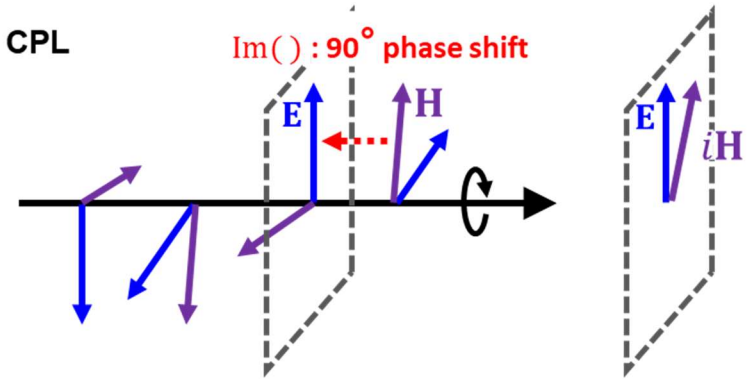


Figure 1. 7 Schematic illustration showing the electric and magnetic field distribution in circularly polarized light (CPL).

Based on the understanding of optical helicity, attempts have been made to enhance the amplification of molecular CD by utilizing increased optical helicity. One notable approach involves the use of plasmonic materials, which can efficiently concentrate the energy of light within a localized region. Plasmonic materials are based on the phenomenon of localized surface plasmon resonance (LSPR), which arises from the resonance of free electrons under the illumination of light, allowing for efficient energy concentration on the surface. This localized energy concentration can increase the electric field present in the optical helicity density, leading to the amplification of optical helicity. Based on this principle, chiral sensing based on the amplification of optical helicity using achiral plasmonic structures has been proposed (Figure 1.8)[23,48]. However, due to the dipolar nature of the formed LSPR, not only the optical helicity of one sign but also the optical helicity of the opposite handedness is simultaneously amplified. As a result, the amplified CD signals of the molecules are cancelled out by the two-directional optical helicity, making it impossible to achieve macroscopic CD enhancement. Therefore, it was necessary to treat the molecules on specific positions of plasmonic structures that exhibit a specific sign of optical helicity in order to realize the amplification of molecular CD. To overcome this limitation, chiral plasmonic materials that can generate significant differences in their own optical helicity have gained attention. Chiral plasmonic structures can induce a strong interaction difference with respect to linearly polarized light, allowing for the retention of optical helicity without its loss even when multiple signs of optical helicity are induced on the structure during spatial integration. By utilizing the optical helicity of chiral plasmonic structures, the *Kadodwala* group successfully demonstrated the effective enhancement of CD signals for single-layer proteins (Figure 1.9)[49]. They proved that using chiral plasmonic nanostructures with high chiroptic response can enhance chiral sensitivity.

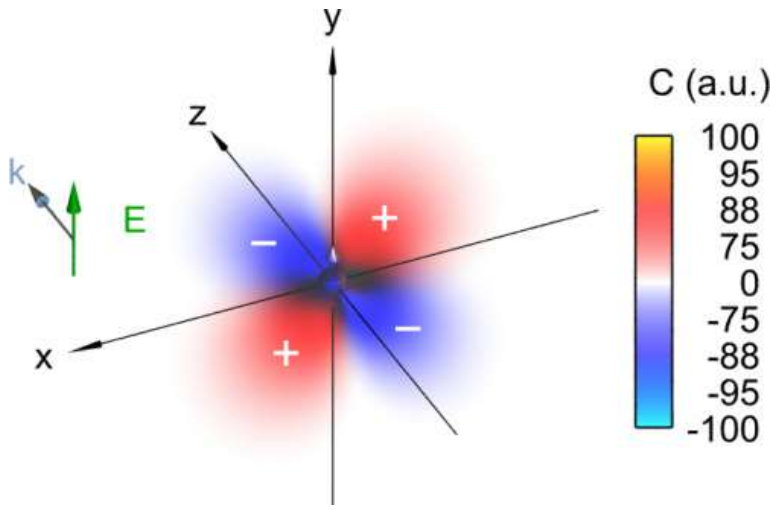


Figure 1. 8 Visualization of the spatial distribution of optical chirality in proximity to a dipole under the influence of an external field in achiral plasmonic nanoparticles.

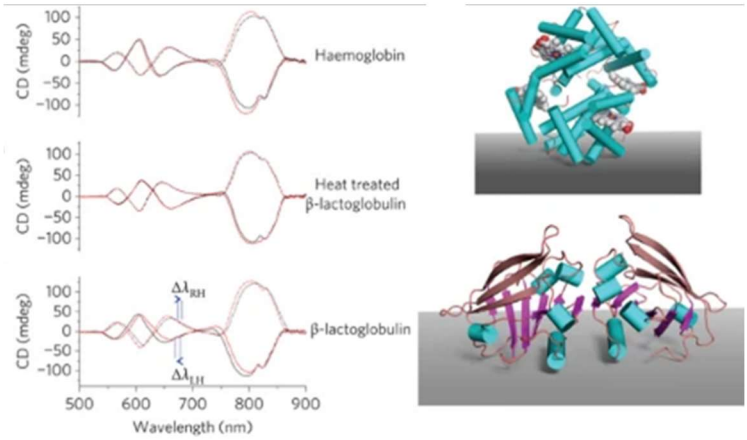


Figure 1. 9 Demonstration of protein adsorption effects on the circular dichroism (CD) spectra of a chiral metasurface (left panel). Changes in peak shifts, $\Delta\lambda_{RH}$ and $\Delta\lambda_{LH}$, are observed upon protein adsorption, revealing optical dissymmetry in opposing nanostructures. Specific interactions with Haemoglobin (upper panel) and β-lactoglobulin (lower panel) are illustrated, with these proteins adopting distinct, arbitrary structures when oriented near a surface (right panel).

## 1.3 Chiral Plasmonic Nanoparticles (Helicoids)

In order to achieve high sensitivity in the implementation and practical application of chiral sensors, the development of plasmonic structures with high chiroptic response is crucial. Our group has synthesized various-shaped nanoparticles through the seed-mediated growth of plasmonic nanostructures[59–63,65,66,72,75,76,80,82–89,95,103–106], controlling the environment during the nanoparticle growth process using cetyltrimethylammonium bromide (CTAB) as the surfactant, L-ascorbic acid (AA) as the reducing agent, gold (Au) precursor ions, and organic molecular additives (Figure 1.10). Particularly, by injecting chiral amino acids and peptides during the synthesis process, we induced selective growth of the nanoparticles based on the chirality expressed on high-index facets and the chiral interactions between organic molecules[6,80,89,107–161]. As a result, we developed a synthetic approach where the chiral nature of the molecules can be implemented within nanoparticles of sizes around 200 nm (Figure 1.11)[65].

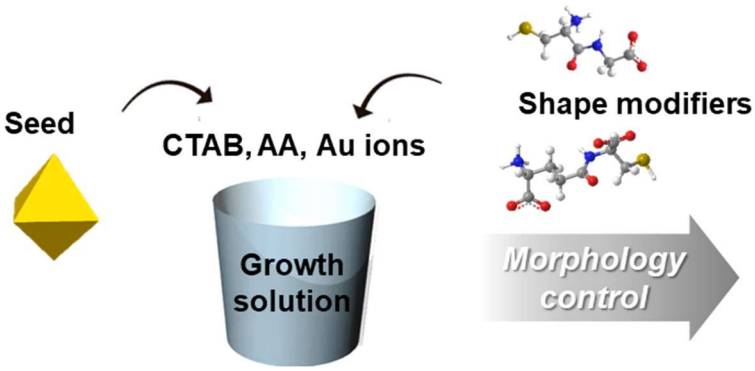


Figure 1. 10 Schematic illustration showing seed-mediated synthesis of gold nanoparticles with controlled morphology.

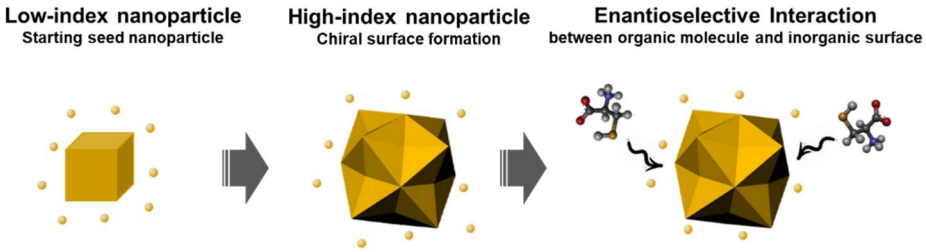


Figure 1. 11 Schematic illustration showing synthesis of chiral plasmonic nanoparticles by utilizing chiral amino acids and peptides as a shape modifier.

The synthesized nanoparticles were named the 432-helicoid series, characterized by their crystallographic structure in three dimensions[162], exhibiting 4-fold rotational symmetry along the <100> direction, 3-fold rotational symmetry along the <111> direction, and 2-fold rotational symmetry along the <110> direction, with helical morphologies (Figure 1.12)[65,80]. By employing different seed nanoparticle shapes[163] (cube, octahedron, rhombic dodecahedron, and plate) and additives (amino-acid, peptide, nucleotides) during the helicoid fabrication process, we were able to synthesize chiral plasmonic nanoparticles with diverse forms and exhibit various chiroptic responses (Figure 1.13)[63–66]. Among them, Helicoid III (helicoids) showed a high chiroptic response with a g-factor of 0.2, demonstrating an absorption difference of around 10% between left-handed circularly polarized (LCP) and right-handed circularly polarized (RCP) light depending on the incident polarization. The strong chiroptic response of these helicoids exhibits optimal optical characteristics for their application as chiral sensors, and their synthesis based on aqueous systems offers the significant advantage of easy and large-scale production of sensor devices.

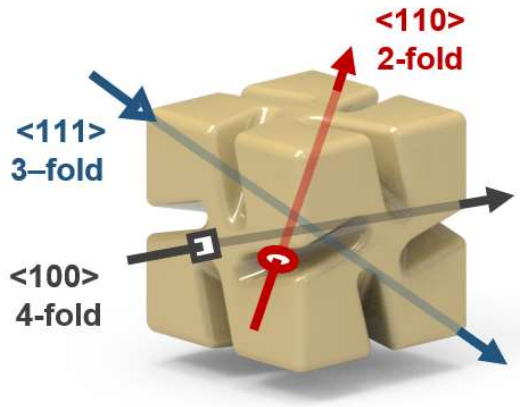


Figure 1. 12 Illustration of 432 Helicoid III, exhibiting 4-fold rotational symmetry along the <100> direction, 3-fold rotational symmetry along the <111> direction, and 2-fold rotational symmetry along the <110> direction, with helical morphologies.

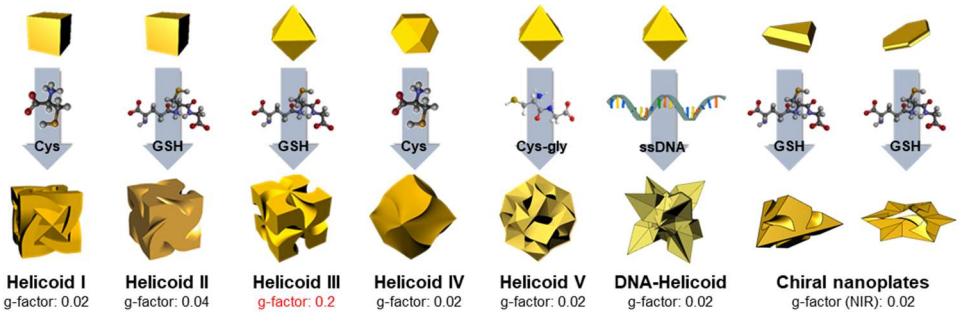


Figure 1. 13 Schematic illustration of 432 helicoid series, synthesized in various growth conditions. Change in seed nanoparticles and chiral molecules induce different chiral morphological evolution and chiroptic responses.

However, there are two main limitations in applying most chiral plasmonic materials, including helicoids, as chiral sensors[21]. Firstly, the amplification of optical helicity density based on localized surface plasmon resonance (LSPR) cannot uniformly amplify only the desired handedness of optical helicity, resulting in the loss of most optical helicity during spatial integration. Therefore, it is practically challenging to achieve strong circular dichroism (CD) enhancement. Secondly, while the conventional theory of molecular CD amplification is based on the amplification of the molecular absorption signal, the amplification of optical helicity by plasmonic materials is spectrally separated from the molecular absorption wavelength in the visible range, making it impossible to achieve amplification. Thus, in order to apply these helicoids as chiral sensors, the development of systems that can achieve uniform amplification of optical helicity and the need for new concepts in theoretical approaches to describe the enhanced sensitivity toward molecular chirality using chiral plasmonic nanostructures.

## 1.4 Collective Resonance (CR) and Perturbation Theory

As mentioned in Chapter 1.3, to utilize chiral plasmonic materials as effective chiral sensors, there is a need for the development of systems capable of inducing a uniform optical helicity density and new theories to explain the enhancement of chiral sensitivity based on chiral plasmonic materials. In this chapter, we will discuss recent research efforts aimed at addressing these challenges.

Firstly, as a solution to the formation of non-uniform optical helicity density based on LSPR, there is an example that utilizes two-dimensionally (2D) aligned plasmonic nanostructures[57,164]. Collective resonance is a new plasmonic mode that arises from the hybridization of diffracted light by regularly arranged plasmonic nanoparticles and the LSPR energy of the nanostructures[58]. Efficient delivery of incident light to the 2D aligned plasmonic material is made possible through the diffraction of light, allowing for simultaneous LSPR of the 2D aligned nanoparticles and intense and uniform concentration of light energy on the surface. This collective resonance, based on energy hybridization, can be modulated by adjusting the energy levels of the hybridized diffraction and LSPR modes. Specifically, the energy level of LSPR can be controlled by varying the size and shape of the assembled nanoparticles, while the energy level of the diffraction mode can be adjusted by the nanoparticle spacing and the angle of incident light[58]. This approach enables the induction of collective resonance with diverse forms and offers the advantage of identifying conditions for strong collective resonance.

The *Vogel* group has fabricated structures capable of inducing collective resonance through the two-dimensional assembly of achiral plasmonic nanoparticles[164]. These structures not only exhibited LSPR of the nanoparticles but also induced collective resonance, resulting in the uniform amplification of the

electric field when the nanoparticles were aligned in a 2D space. Furthermore, the researchers aimed to induce the enhancement of molecular circular dichroism (CD) by incorporating the chiral molecules into the system. The formation of collective resonance facilitated the amplification of not only the strong electric field but also the optical helicity density. Consequently, they achieved a greater amplification of molecular CD signals compared to LSPR-based CD enhancement (Figure 1.15). However, this methodology still fell short in achieving a uniform optical helicity density due to the dipolar nature of the achiral structures themselves, which limited the extension of collective resonance to a uniform optical helicity density. Thus, they only achieved slightly higher chiral sensitivity compared to LSPR. Although attempts were made to induce collective resonance in 2D-aligned chiral plasmonic structures, the formation of collective resonance with strong chiroptic response has not been reported in the literature.

In elucidating the second quandary, a perturbation theory has been established, offering a physical explication for the phenomenon of energy modulation in plasmonic materials, instigated by proximate molecules[68]. Predominantly, molecules intrinsic to the natural environment exhibit the capacity to engage in photon-molecular interactions within the resonance wavelength band of plasmonic constituents. This photon-molecular interplay engenders a dipolar configuration within the molecule. Utilizing Eq. 1.2 as the foundational framework, it's possible to characterize this molecular dipole moment. Predicated upon this comprehension of the dipolar molecule, one can physically derive the extent of potential interaction between a molecule and photonic energy. As indicated by Eq. 1.7, the variation in photonic energy induced by a molecule is proportional to the molecule's polarizability, denoted as $\alpha$. Drawing upon this physical apprehension, a perturbation theory has been promulgated which describes the energy modulation in plasmonic substances in a system where plasmonic materials and molecules coexist. According to this perturbation theory, the decrement in energy of plasmonic

materials, instigated by molecules, incites a red shift in the resonance wavelength of plasmonic substances. This concept adheres to the formula $E=hc/\lambda$ and has precipitated the development of molecular detectors predicated upon plasmonic materials. To elucidate further, photonic energy, when intensely concentrated proximate to plasmonic materials, provokes an amplified photon-matter interaction with substances adjacent to these plasmonic entities. This magnified interaction permits molecules to deplete the energy of both light and plasmonic materials more efficaciously, thus enabling the implementation of such a system. This perturbation theory, coupled with Eq. 1.3, proposes that chiral polarizability $G$, which is contingent upon circularly polarized light and emanates from chiral molecules, can induce alterations in energy in plasmonic materials, in a manner analogous to electric polarizability, which is subject to the molecule's chirality. However, our comprehension of the chiral light-matter interaction between circularly polarized light and chiral molecules currently lacks depth. This deficiency has impeded the establishment of a precise correlation between the chirality of a molecule and energy perturbation. Consequently, the formulation of a chiral perturbation theory, which could potentially elucidate the properties of chiral sensors anchored on chiral-light matter interaction and chiral plasmonic materials, remains a work in progress.

## 1.5 Scope of Thesis

The overarching objective of this thesis is to engineer highly sensitive chiral sensing platforms, deploying chiral plasmonic nanostructures characterized by intense and uniform optical helicity density. The work ambitiously straddles the fabrication and optical characterization of two-dimensional (2D) aligned chiral plasmonic nanoparticles, the development of theoretical underpinnings for their precise deployment in chiral sensing, and the experimental progression towards functional chiral sensor platforms.

The thesis is meticulously structured into four main chapters. Chapter 2 is dedicated to the experimental fabrication and subsequent optical characterization of 2D aligned chiral plasmonic nanoparticles. Chapter 3 delves into theoretical explorations pertaining to these nanostructures, specifically focusing on their prospective utility in chiral sensing applications. Chapters 4 and 5 encapsulate the practical validation and potential applicability of these 2D aligned chiral plasmonic nanoparticles across a spectrum of chiral biomolecular sensing and optical systems.

In Chapter 2, we propose to enhance the chiroptic response of pre-existing chiral plasmonic nanostructures by incorporating helicoids, structures already known for their potent chiroptic responses. We endeavor to design an improved system capable of inducing collective resonance, honing in on a 2D aligned plasmonic nanoparticles system. The strategy includes developing a novel methodology for the fabrication of a uniform 2D helicoid crystal and gaining insights into the optical properties inherent in such constructs.

In Chapter 3, we seek to decipher the theoretical foundations of the robust chiroptic property of the fabricated 2D helicoid crystal, prior to launching into empirical exploration of its chiral sensor attributes. This involves un

dertaking an electromagnetic simulation-based chiroptic property analysis, whi ch conclusively identifies a strong and uniform optical helicity as a crucial determinant of enhanced chiral sensitivity, underpinned by the development o f chiral perturbation theory.

In Chapters 4 and 5, the experimental examination of the chiral sensiti vity of the 2D helicoid crystal is documented. Chapter 4 entails the assessm ent of chiral sensitivity using a proline molecule solution, a simple chiral a mino acid. It convincingly demonstrates that shifts in the Circular Dichroism (CD) signal of the 2D helicoid crystal are contingent on the molecule's chira lity, thereby enabling highly sensitive detection.

Chapter 5, as a natural extension of the previous chapter, expands the potential array of detectable chiral biomolecules to include nucleotides and p roteins. The focus here is not only on detecting these biomolecules but also on discerning chirality changes induced by structural alterations of nucleotide s and proteins affixed to the 2D helicoid crystal. This ambitious endeavor c ulminates in the real-time detection of chirality at a monolayer molecular lev el. In the latter part of Chapter 5, the 2D helicoid crystal is integrated into a commercialized Surface Plasmon Resonance (SPR) sensing system, bypassi ng the limitations of a transmission-based custom optical system. This facilit ates the use of the fabricated structure as a sensor chip, enabling detection of previously elusive chiralities. The collective resonance and CD signal of t he 2D helicoid crystal were observed to exhibit enantioselective shifts in res ponse to molecular chirality. This empirical evidence reaffirms the versatility and high chiral sensitivity of the 2D helicoid crystal.

We contend that our pioneering work in re-engineering and transformi ng currently available chiral plasmonic nanoparticles into advanced detection systems for molecular chirality is poised to revolutionize the field. By enhan cing the existing technology and morphing it into a sophisticated and finely-

tuned tool capable of distinguishing the minutiae of molecular chirality, we are pioneering a new frontier in the study and application of chiral plasmonic structures. This is not a theoretical exercise but rather a practical undertaking with profound implications. Our work paves the way for superior chiral sensing applications, not just in controlled laboratory conditions but extending its reach into practical, real-world scenarios. This undertaking has the potential to significantly enhance the sensitivity and specificity of molecular chirality detection, leading to more precise results and greater scientific understanding. Ultimately, this advancement represents a paradigm shift that moves us closer to practical and effective chiral sensing applications, thereby making a notable contribution to the field of chirality detection.

# Chapter 2. Fabrication of 2D Helicoid Crystal and Its Optical Properties

## 2.1 Fabrication of 2D helicoid crystal using nano-patterned poly(dimethylsiloxane)(PDMS)

In order to fabricate a two-dimensional (2D) helicoid crystal with optimal lattice fidelity, we exploited an approach combining interfacial self-assembly and mechanical rubbing. This innovative strategy facilitated the accurate positioning of individual helicoid nanoparticles into each nanowell of a polydimethylsiloxane (PDMS) template. PDMS was chosen as the material of choice due to its intrinsic properties such as optical transparency, excellent biocompatibility, and the ability to mimic inverse structures (Figure 2.1)[165].

Our process commenced with the creation of a PDMS template featuring a nanostructured well array, specifically designed to encapsulate helicoid nanoparticles. We engineered a hexagonal array of circular wells, each with a diameter of 100 nm and situated at a pitch of 400 nm, on PDMS substrates. This configuration was realized using a molding process that employed a silicon (Si) master substrate in conjunction with hydrosilylation-curing PDMS (h-PDMS) and Sylgard 184-PDMS. To prevent unwanted PDMS adhesion, the Si master substrate underwent a passivation process using (tridecafluoro-1,1,2,2-tetrahydrooctyl)trichlorosilane (SIT8174.0, Gelest) prior to molding. This was followed by the preparation of the h-PDMS liquid prepolymer, a complex mixture composed of vinylmethylsiloxane (VDT-731, Gelest), 1,3,5,7-tetravinyl-1,3,5,7-tetramethylcyclotetrasiloxane (SIT7900.0, Gelest), platinum divinyltetramethyldisiloxane (SIP6831.2, Gelest), and methylhydrosiloxane (HMS-301, Gelest). The prepared h-PDMS was then spin-coated onto the Si

master substrate at a two-step speed of 500 rpm for 5 seconds, followed by 3000 rpm for 45 seconds. The coated substrate was cured at 60 °C for 30 minutes. This was succeeded by the application of a degassed mixture of 184-PDMS (with a 10:1 ratio of curing base to agent), which was thermally treated at 60 °C for two hours.

The final product, a nanowell-patterned PDMS substrate, was meticulously detached from the Si master substrate and cut to yield a 1 $cm^2$ sample, replete with over $10^8$ nanowells. As evidenced by the Figure 2.2, the fabricated PDMS substrate exhibited a highly uniform well-structure, and the occurrence of diffraction effects underscored the precise and regular architecture of the PDMS.

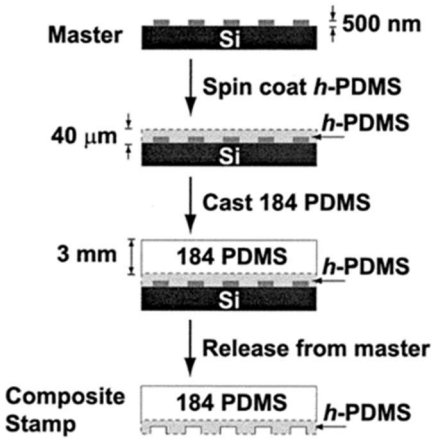


Figure 2. 1 Schematic illustration showing inverse-patterning of nanopatterned silicon substrate with PDMS.

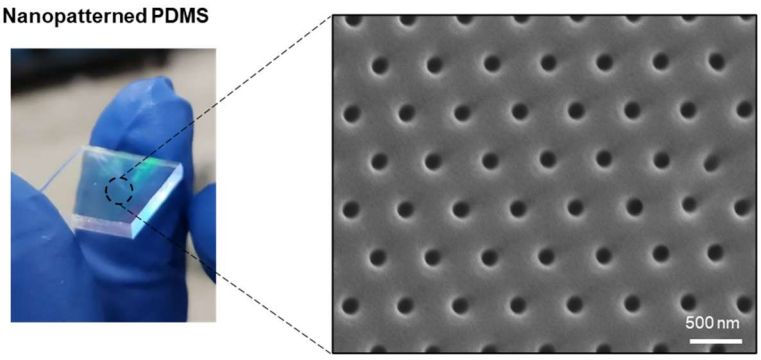


Figure 2. 2 Photograph of nano well patterned PDMS substrate (left). Scanning electron microscope (SEM) image of nano well patterned PDMS substrate with hexagonally patterned nano well sized 100 nm diameter.

In the process outlined in Extended Data Figure 2. 3, the formation and incorporation of as-synthesized helicoids into a nanopatterned Polydimethylsiloxane (PDMS) substrate is comprehensively detailed. The process initiates with the creation of a helicoid suspension (1 mL) housed in a Teflon cell, known for its chemical inertness. Subsequently, an interface between water and an organic layer is meticulously produced by adding n-hexane (2 mL) to the top of the suspension, facilitating phase separation. This interface then receives an addition of 1-Dodecanethiol (5 μL), a well-known organic thiol, facilitating the initiation of the self-assembly process. The following step employs an advanced NE-300 syringe pump from New Era Pump Systems, which introduces absolute ethanol (5 mL) at a controlled rate of 100 μL/s, leading to the gradual assembly of the helicoids at the water-hexane interface. Strategic removal of the n-hexane layer leads to a dense monolayer of helicoids existing at the water-air interface. This layer exhibits a characteristic bulk gold color, reflecting the closely packed formation of the nanoparticles (NPs). Utilizing a technique known as dip-coating, this dense helicoid layer is methodically transferred onto the nanopatterned PDMS substrate. Upon achieving a uniform coverage of helicoids over the PDMS substrate, this resultant composite is positioned onto a glass slide, pre-coated with a thick layer of PDMS (~5 mm). To facilitate selective insertion of helicoids into the PDMS nanowells, mechanical shear stress is applied to the substrate through oblique rubbing with a Teflon-coated stick. Post this embedding process, the substrate – now metamorphosed into a 2D helicoid crystal – undergoes careful washing with n-hexane and absolute ethanol in succession, to ensure the removal of any residual NPs adhered to the flat surface of the PDMS. The final stage involves a rinse with deionized water (DW) followed by storage at ambient conditions (25 °C) for further characterization and application.

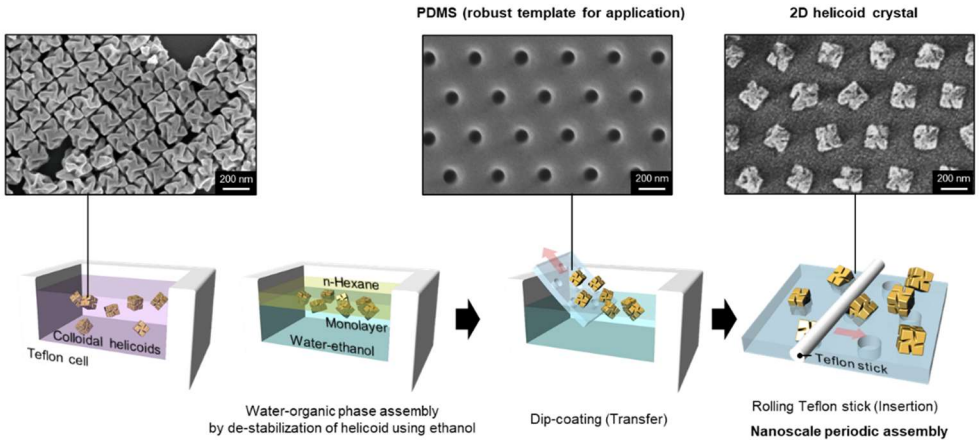


Figure 2. 3 Schematic illustration (bottom) and scanning electron microscopy (SEM) image showing the procedure of helicoid insertion and fabrication of 2D helicoid crystal with high lattice fidelity. Pre-synthesized helicoids are densely assembled by using water-organic phase assembly and inserted in nano well of PDMS by using mechanical shearing of Teflon coated sticks.

Scanning electron microscopy (SEM) and dark-field optical microscopy (DFOM) analyses reveal the presence of uniformly assembled 2D helicoid crystals. As shown in Figure 2. 4, we can clearly confirm the morphology of helicoid nanoparticles is not destroyed after fabrication of 2D helicoid crystal. A low-magnification DFOM image showcases distinct bright scattering spots, which correspond to individual helicoids within the 2D superlattice (Figure 2.5). The resulting fast Fourier transform (FFT) image further validates the long-range and uniform ordering of the 2D helicoid crystals. The incorporation yield of helicoids was quantified as approximately 98% based on meticulous evaluations conducted on 13,480 wells. The notable advantage of this method lies in its ability to fabricate large-area substrates with precisely aligned plasmonic nanoparticles. By achieving a uniform assembly of 2D helicoid crystals, we can ensure a consistent and predictable arrangement of the nanoparticles over the extensive substrate. This controlled alignment enables enhanced control and manipulation of the optical properties of the nanoparticles, facilitating the design and development of advanced nanophotonic devices and applications.

In summary, this method offers the advantage of fabricating large-area substrates with precisely aligned plasmonic nanoparticles. The uniform assembly of 2D helicoid crystals enables enhanced control over the optical properties of the nanoparticles, leading to promising advancements in nanophotonic devices and applications. The scientific procedures of SEM, DFOM, and quantitative analysis were employed to demonstrate the uniform arrangement and high incorporation yield of the helicoids, validating the effectiveness of this fabrication method.

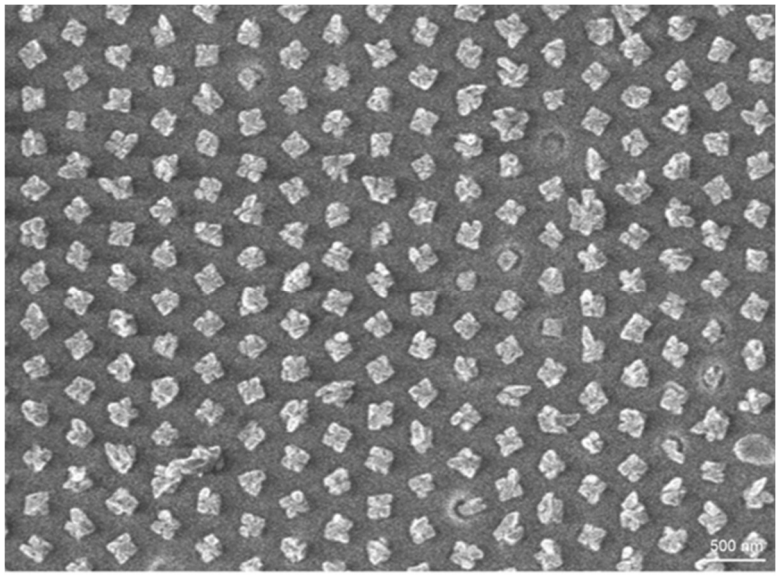


Figure 2. 4 Scanning electron microscope (SEM) image of 2D helicoid crystals.

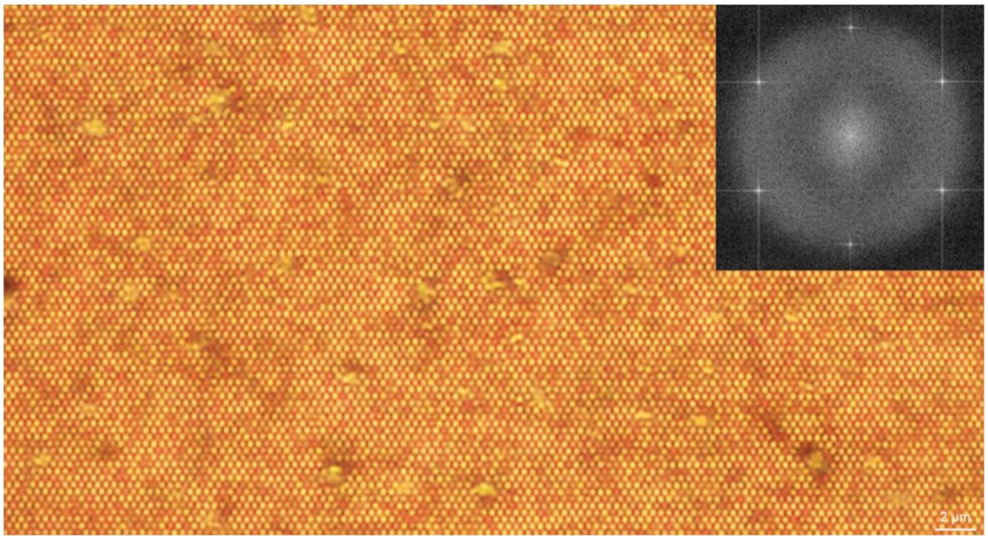


Figure 2. 5 Dark field optical microscope (DFOM) image and Fast Fourier transformation (FFT) image of 2D helicoid crystal.

## 2.2 Characterization of collective resonance and CD response of 2D helicoid crystal

In two-dimensional (2D) assemblies of plasmonic nanoparticles, an intriguing optical phenomenon known as collective resonance can be observed. Collective resonance refers to a plasmonic mode that emerges from the hybridization of diffractive effects originating from the assembled nanostructure and the localized surface plasmon resonance (LSPR) intrinsic to the individual plasmonic nanoparticles. This coupling results in an intense, highly localized energy field, promoting a significant two-dimensional spatial confinement of light energy[58]. The manifestation of collective resonance within such assembled plasmonic nanostructures is a dynamic process, with its characteristics being sensitive to the energy levels of the nanoparticle's LSPR and the diffractive mode. By judiciously altering the size and morphological features of the assembled nanoparticles, it is possible to modulate the wavelength and intensity of the collective resonance, providing a pathway towards its active control. Furthermore, the diffraction mode's energy, and hence the resulting collective resonance, can be altered by varying the periodicity of the assembled particles and adjusting the angle of incident light (Figure 2. 6). This points towards the versatility of such structures in harnessing and manipulating light at the nanoscale. Previously, the *Vogel* group has leveraged these phenomena to manipulate the absorption signals by altering the periodicity of achiral plasmonic nanoparticles in a 2D assembly (Figure 2. 7)[164]. This has demonstrated the potential for controlling and tuning the collective resonance for diverse applications.

Building upon the fundamental principles of collective resonance, we initiated an extensive analysis of the Circular Dichroism (CD) signals produced by the fabricated two-dimensional (2D) helicoid crystal structure. Our uniquely

synthesized 2D helicoid crystal demonstrated a localized surface plasmon resonance (LSPR) of the constituting nanoparticles at a wavelength of 600 nm. Concurrently, a separate diffraction mode was discernible near a wavelength of 400 nm.

With these distinct energy levels at hand, our energy hybridization model implied that the cooperative resonance signal originating from the 2D helicoid crystal could manifest at wavelengths greater than 600 nm. This hypothesis was validated during our rigorous CD analysis where we observed a redshift in the CD signal. This shift, from 600 nm to 635 nm, was a clear consequence of the collective resonance induced by the 2D helicoid crystal structure, indicating an augmented response (Figure 2. 8).

Drawing upon these preliminary observations and our understanding of the collective resonance phenomenon, we endeavored to design and fabricate a 2D helicoid crystal system that could elicit a robust chiroptic response. Our approach involved a meticulous analysis of the collective resonance and CD signals as functions of variables such as the variations in the LSPR due to different helicoid sizes, the periodicity of the 2D helicoid crystal, and the angle of incident light. Our comprehensive investigation aims to deepen our understanding of the intricate interrelationships between these parameters, enabling us to manipulate and control these factors in a systematic manner. By achieving this, we strive to engineer 2D helicoid crystal systems that offer customizable chiroptic responses, setting the stage for a new era in the field of plasmonic nanostructures.

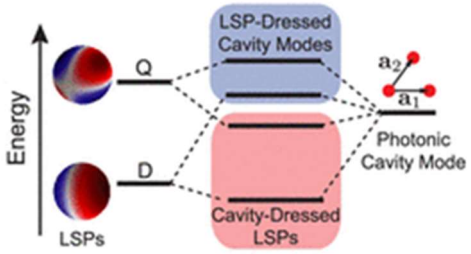


Figure 2. 6 Collective resonance which originates from the hybridization of LSPRs and diffraction (photonic cavity) mode.

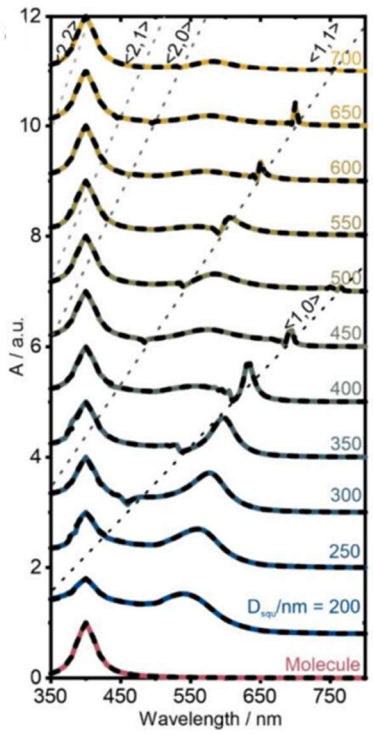


Figure 2. 7 Calculated absorption spectra of 2D aligned achiral plasmonic lattices with various periodicity ($D_{squ}$) of nanoparticles.

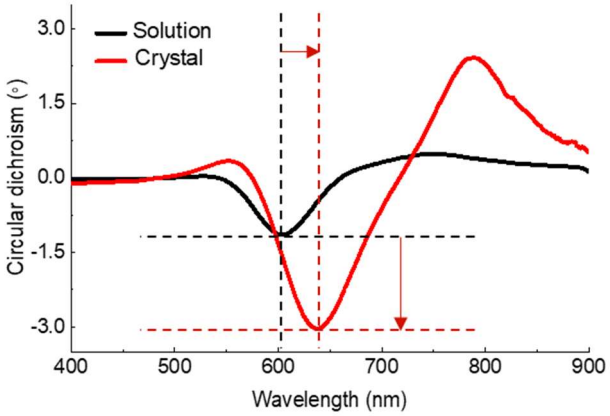


Figure 2. 8 Circular dichroism response of helicoids in solution and 2D helicoid crystal.

### 2.2.1 Controlling LSPR of helicoids

In our pursuit to induce robust chiroptic responses through collective resonance in a two-dimensional (2D) helicoid crystal system, our initial step was to devise a controlled synthesis approach to regulate the localized surface plasmon resonance (LSPR) of the helicoids that constitute the 2D helicoid crystal. It is a well-established fact that the resonant wavelength of the LSPR of plasmonic nanoparticles is contingent upon the size and morphology of the synthesized particles[61,166]. A prototypical example of this phenomenon can be seen in the seed-mediated growth process, wherein subtle adjustments in the initial seed particles yield nanoparticles of varying dimensions.

Exploiting this principle, we meticulously modulated the concentration of the octahedron seed nanoparticles employed during the synthesis of the helicoids. This allowed us to generate a suite of nanoparticles, each exhibiting a unique LSPR energy profile.

Our rigorous analysis revealed that a decrement in the initial seed concentration resulted in the synthesis of helicoids with progressively diminished dimensions, as confirmed via Scanning Electron Microscopy (SEM) characterization (Figure 2.9). An intriguing trend was noted in these aqueously synthesized helicoid nanoparticles - as their size increased, the dip of the CD signal exhibited a redshift, while maintaining a similar degree of chiroptic response across all sizes (Figure 2.10).

Building upon these helicoids, we ventured into the assembly of the 2D helicoid crystal structure. The ensuing CD analysis of this intricate structure provided invaluable insights into how certain LSPR characteristics of the helicoids

contribute towards the induction of a strong chiroptic response in the 2D helicoid crystal via collective resonance. This intricate understanding paves the way for a more strategic design of plasmonic nanostructures with tailor-made optical properties.

xpanding upon the aforementioned results, we noticed that the two-dimensional (2D) helicoid crystals assembled using these nanoparticles exhibited an overall redshift in their response compared to the helicoids in solution. Despite the individual helicoids sharing a similar CD signal profile, we observed a considerable divergence in the CD signals from the 2D helicoid crystal. This discrepancy was largely attributed to the disparate tendencies towards plasmon hybridization exhibited by these structures, an observation corroborated by the data represented in Figure 2.11.

Capitalizing on this compelling observation, we embarked on an analytical study, quantitatively comparing the CD signals emanating from the solution-phase helicoids and their 2D crystal counterparts across a range of helicoid sizes. Through this rigorous comparison, we were able to deduce that the collective resonance exhibited by helicoids measuring approximately 180 nm in size contributed significantly towards enhancing the CD signal emanating from the 2D helicoid crystal (Figure 2.12).

This finding, implicating the direct role of the helicoid size in determining the chiroptic response, further underlines the potential of precise dimensional control as a potent tool for tuning the optical properties of 2D helicoid crystal structures. By controlling the size of the constituent helicoids, we can effectively manipulate collective resonance, leading to the engineering of plasmonic nanostructures with customized chiroptic responses. This in-depth understanding

of the plasmonic behavior in helicoid crystal structures presents a pivotal advancement in the field of plasmonics, enabling novel strategies for the design and synthesis of plasmonic nanostructures.

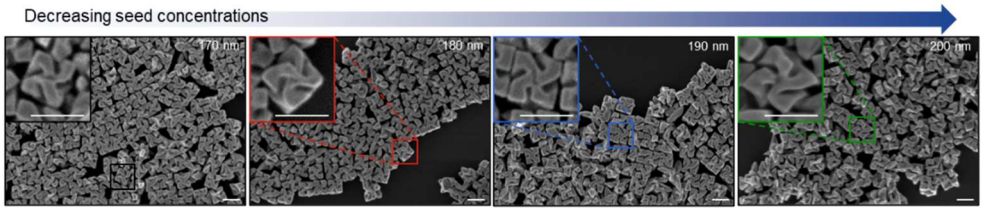


Figure 2. 9 Scanning electron microscope (SEM) image of helicoids synthesized with various seed nanoparticle concentrations.

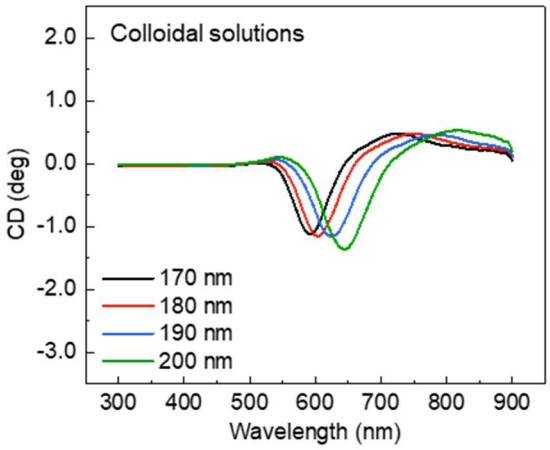


Figure 2. 10 Circular dichroism (CD) response of solution helicoids with various size.

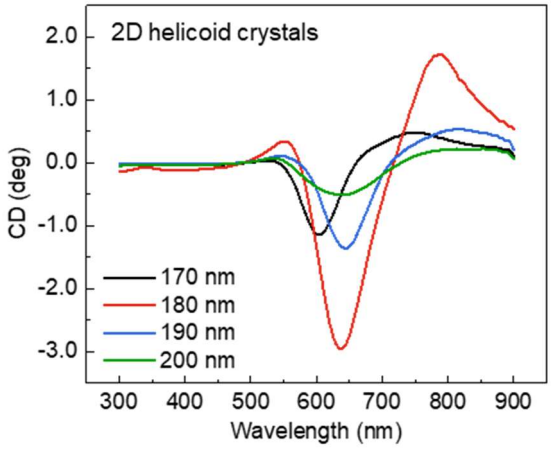


Figure 2. 11 Circular dichroism (CD) response of 2D helicoid crystals with differently sized helicoids.

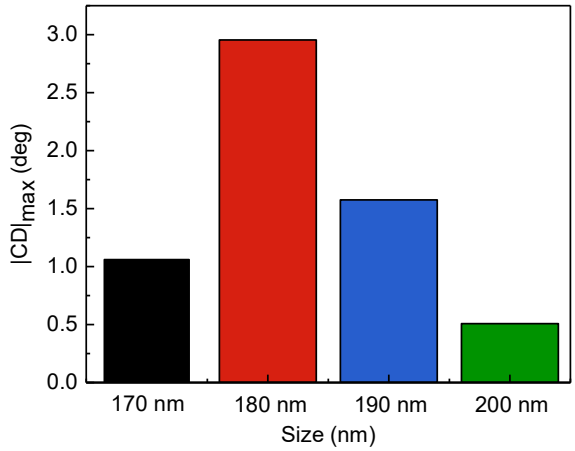


Figure 2. 12 Maximum absolute value of circular dichroism (CD) response in 2D helicoid crystal comprised with differently sized helicoids. 180 nm-sized helicoids induced strongest enhancements of chiroptic response in 2D helicoid crystal.

### 2.2.2 Controlling diffraction mode of 2D helicoid crystal

In order to induce a shift in the position of the diffraction mode, we proceeded to manipulate the angle of incidence of the incoming light. A plasmonic crystal with a regular lattice structure can produce diffraction due to its periodic configuration and altering the angle of the incoming light results in a change in the momentum coupling between the diffracted light and the incident light. This results in a shift in the momentum of the light incident on the plasmonic nanoparticles in the 2D plane[167]. Leveraging this mechanism, the energy transferred to the nanoparticles can be modulated with the incident light angle, inducing changes in the collective resonance generated by coupling between the localized surface plasmon resonance (LSPR) and diffraction mode (Figure 2.13).

Using this foundational knowledge, we analyzed the chiroptic response of the 2D helicoid crystal across varying incident light angles. Using a simple diffraction equation, we initially predicted the mathematical behavior of the diffraction modes and their angular tendencies in the hexagonal lattice that we utilized. As can be seen in Figure 2.14, a hexagonal lattice typically presents six dominant diffraction modes. Each of these modes can couple with the LSPR, generating different collective resonances at distinct wavelengths. By mapping these patterns, we endeavored to understand the origins of modes in the 2D helicoid crystal and identify the incident light conditions that could potentially maximize the chiroptic response of the 2D helicoid crystal.

To facilitate our experiments, we fabricated a holder capable of adjusting the angle between the 2D helicoid crystal and the incident light (Figure 2.15), and proceeded with the CD analysis. As we increased the incident light angle from 0 degrees to 60 degrees in increments of 10 degrees, we observed an enhancement in

the LSPR as the light-interacting region of the 2D helicoid crystal increased. This corresponded to a strengthening and a redshift in the CD signal due to the formation of collective resonance and changes in the hybridization pattern (Figure 2.16).

The heat map plot of the CD signals elucidated the trend of CD signal changes in the 2D helicoid crystal with varying incident light angles, and facilitated an intuitive visualization of this effect. The mode that induced the strongest chiroptic response and experienced a shift towards longer wavelengths showed a signal change pattern similar to the (-1, -2) mode derived from the diffraction equation. This suggested that the observed CD response was primarily induced by the collective resonance generated by the coupling of the (-1, -2) diffraction mode with the LSPR (Figure 2.17). This conclusion underpins the utility of manipulating the incident light angle as a viable strategy to tune the chiroptic response in 2D helicoid crystals.

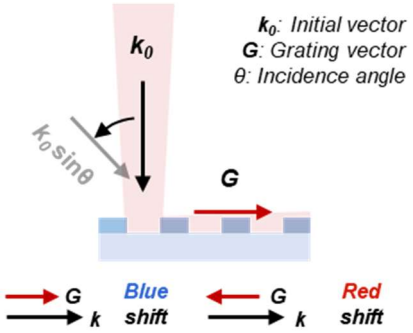


Figure 2. 13 Schematic illustration showing the momentum change toward 2D plane due to the diffraction by the periodic nanostructures.

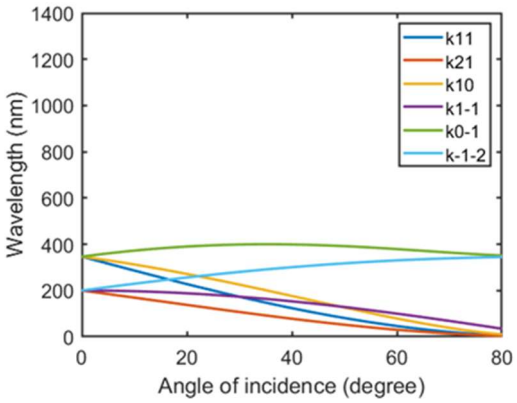


Figure 2. 14 Diffraction mode from the 400-nm periodic lattice.

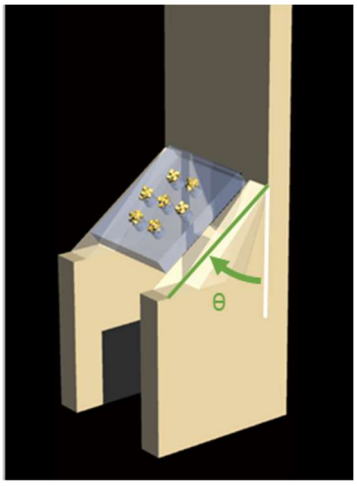


Figure 2. 15 Schematic illustration of the incident-angle adjustable holders.

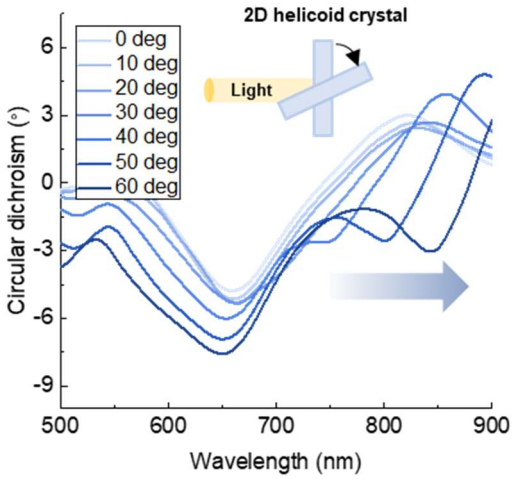


Figure 2. 16 Angle-resolved circular dichroism response of 2D helicoid crystal.

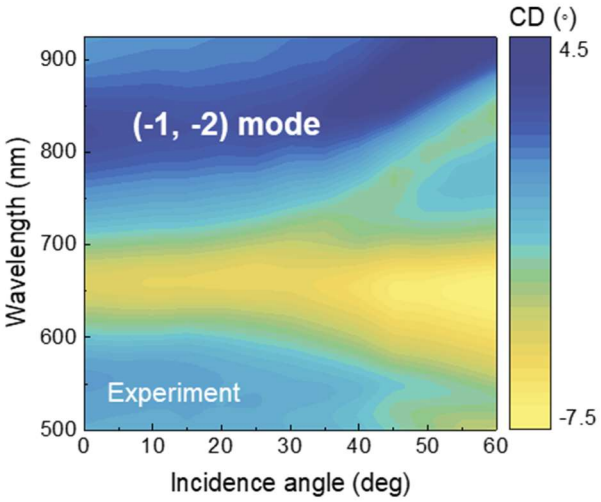


Figure 2. 17 Heat-map plot of angle-resolved CD response of 2D helicoid crystal.

Following this, we sought to modulate the collective resonance by adjusting the periodicity of the assembly of the 2D helicoid crystal[91]. As seen in Figure 2.6, altering the assembly period of the plasmonic crystal can provoke changes in the diffraction mode, thereby inducing shifts in the resulting collective resonance. We modified the periodicity of the original helicoid crystal from 400 nm to 600 nm, which consequently shifted the position of the diffraction mode from 400 nm to 600 nm. By shifting the diffraction mode to longer wavelengths, we examined the changing hybridization patterns of the collective resonance.

Consistent with predictions made through the hybridization diagram, when the periodicity of the collective CD response was altered from 400 nm to 600 nm, the occurrence of collective resonance was red-shifted towards longer wavelengths, and the intensity of the corresponding signal was found to diminish (Figure 2.18).

Comparison of this CD signal with that from the original 2D helicoid crystal with a periodicity of 400 nm allowed us to confirm that the 2D helicoid crystal with a spacing of 400 nm we fabricated exhibited a collective mode that induced a more potent chiroptic response. This systematic analysis underscores the role of controlling the assembly periodicity in modulating the chiroptic response, providing an effective strategy to tune collective resonances in 2D helicoid crystals.

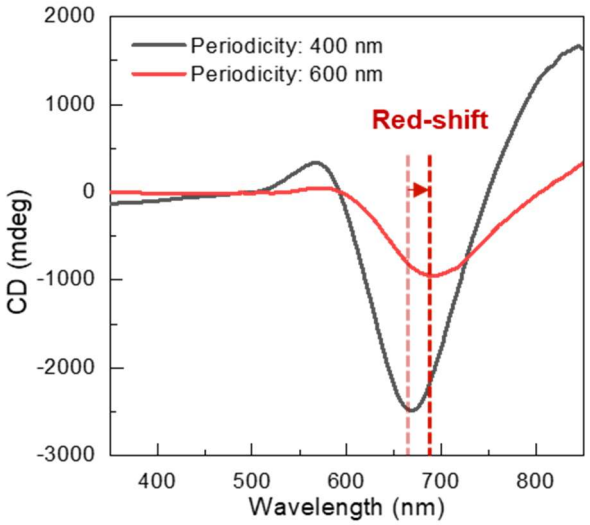


Figure 2. 18 Circular dichroism (CD) response of 2D helicoid crystals with 400 nm and 600 nm periodicity.

# Chapter 3. Theoretical Investigation on 2D Helicoid Crystal for Chiral Sensing Applications

## 3.1 Electromagnetic simulation on 2D helicoid crystal

### 3.1.1 Collective CD response of 2D helicoid crystal

Before commencing a detailed analysis of the pronounced chiroptic response of the 2D helicoid crystal using electromagnetic simulations, our first objective was to achieve a qualitative understanding of the robust collective resonance and circular dichroism (CD). The helicoid nanoparticles used in our study exhibit a notable structural distinction from traditional 2D chiral structures. Specifically, these particles showcase a unique 4, 3, 2-fold rotational symmetry along the <100>, <111>, and <110> crystallographic axes, respectively - a property referred to as 432 symmetry (Figure 1.12)[80].

The 432 symmetry characteristic of these nanoparticles signifies one of the most isotropic forms achievable by chiral entities in a three-dimensional lattice, resulting in a unique structural advantage. This symmetry means that the particles maintain a nearly consistent morphology irrespective of the observation angle. This isotropy implies that helicoid nanoparticles can deliver a consistent chiral response, largely unaltered by the direction of incident light. Consequently, this allows for a simplification of the helicoid nanoparticle into a sphere model for ease of analysis. By incorporating the physical chirality parameters of the helicoid into this model, it is possible to observe a CD signal that bears significant resemblance to that of the actual helicoid nanoparticles (Figure 3.1). All the numerical simulations have been conducted using COMSOL Multiphysics.

The inherent 432 symmetry of the helicoid nanoparticles predicts a noteworthy behavior. Even when the orientation of helicoid constituents within the experimentally fabricated 2D helicoid crystal is randomly distributed, the chirality intrinsic to the nanoparticles does not diminish. Instead, it contributes to the formation of a robust collective CD signal within the 2D surface where the collective resonance occurs. To verify this prediction, we conducted a simulation wherein the angle of incidence was fixed at 60 degrees and a 2D helicoid crystal with a variety of helicoid orientations was synthesized. The resulting collective CD response of the 2D helicoid crystal, consequent to variations in orientation, was then closely observed.

The results revealed that the collective CD signal of the 2D helicoid crystal exhibited substantial variance contingent on the orientation of the helicoid. Interestingly, even when these collective CD signals were averaged, the resultant CD signal did not vanish, contrary to expectation. Instead, the signal exhibited a negative value, closely mirroring the CD signal observed experimentally (Figure 3.2). This critical observation enabled us to confirm that the distinct 432 chirality of the helicoid is capable of preserving the circular dichroism-specific response within the collective resonance.

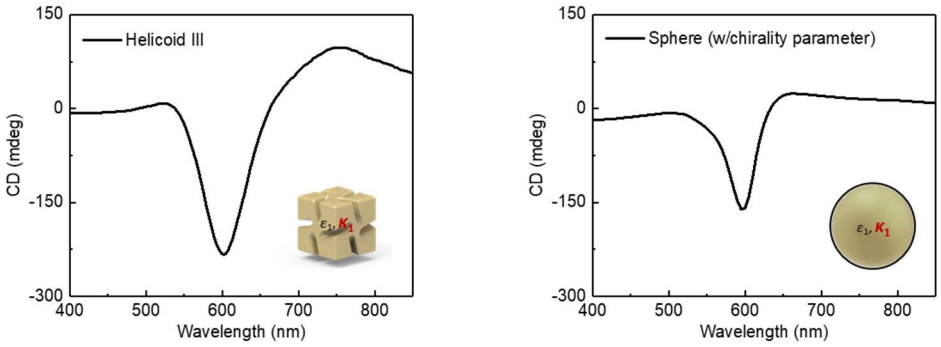


Figure 3. 1 Circular dichroism (CD) response of helicoids and spherical nanoparticles with chirality parameter of helicoids.

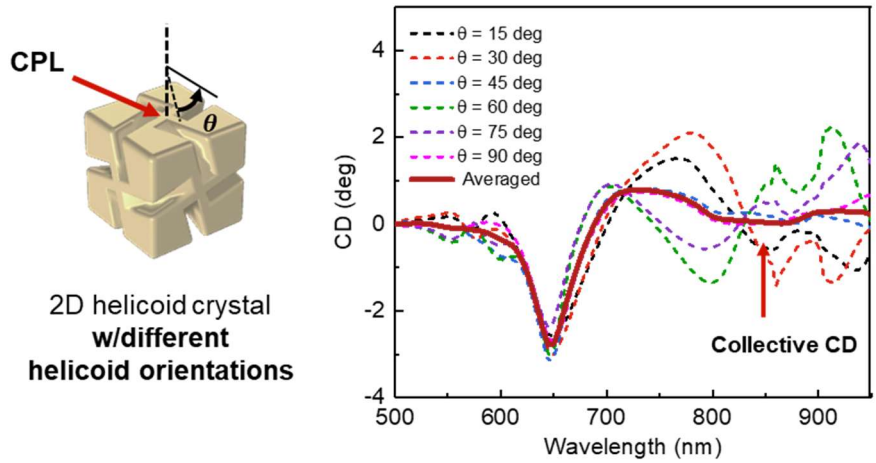


Figure 3. 2 Simulated CD response of 2D helicoid crystal with different helicoid orientations.

In an attempt to complement our qualitative understanding with a robust physical comprehension of the strong CD response in the 2D helicoid crystal, we undertook an analysis of the optical response of the 2D helicoid crystal under circularly polarized light (CPL) incidence via simulation. Specifically, we aimed to identify the optical modes that occur in the 2D helicoid crystal under CPL exposure, and the corresponding amplification of the CD signal. CPL constitutes transverse electric (TE) and transverse magnetic (TM) polarizations that propagate with a phase difference of $\pi/2$. For a material to exhibit a pronounced response to CPL, it must accommodate the concurrent excitation of TE and TM modes induced by the CPL. On this premise, we induced a photonic band diagram to ascertain the TE and TM modes in the 2D helicoid crystal under CPL incidence, utilizing electromagnetic simulation.

As illustrated in Figure 3.3, we observed that the 2D helicoid crystal, when exposed to CPL, enables the manifestation of a strong CD signal due to the simultaneous excitation of TE and TM modes in the local surface plasmon resonance (LSPR) wavelength region (~600 nm). Moreover, the TE and TM modes are induced at nearly identical wavelengths in the area where the collective resonance occurs. This observation was particularly significant at the location of collective resonance induced by CPL inclined at an angle of 60 degrees, where we could observe the concurrent incidence of both TE and TM modes. Based on these analyses, we deduced that the robust CD signal emanating from the 2D helicoid crystal at the LSPR, observed in Figure 2.16, can be attributed to the simultaneous excitation of TE and TM modes facilitated by CPL. We further discerned that the amplification of the collective CD signal with increasing incidence angle of light is a consequence of the concurrent excitation of TE and TM modes resulting from the increasing incidence angle. This finding illuminates the underlying mechanism of the strong chiroptic response of the 2D helicoid crystal and its dynamic relationship with the incident light angle.

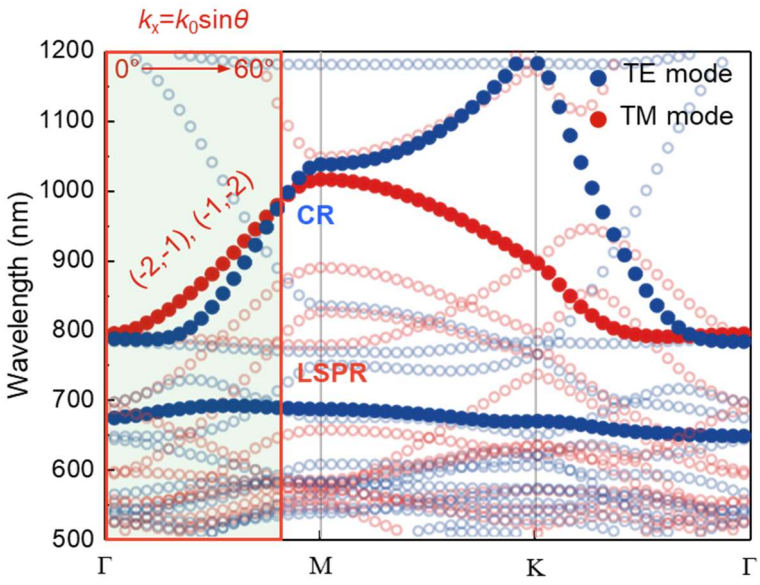


Figure 3. 3 Photonic band diagram of 2D helicoid crystal under circularly polarized light illuminations.

### 3.1.2 Collective CD response of 2D helicoid crystal

To validate the efficacy of chiral plasmonic nanostructures in the applications of chiral sensing, a rigorous analysis of their optical helicity density ($h$) is indispensable. Consequently, we have conducted a comprehensive study focusing on the manifestation of optical helicity density in a two-dimensional (2D) helicoid crystal due to collective resonance.

Optical helicity density, as delineated in Chapter 2, functions as an indicator expressing the degree to which light in a molecular space is both helically organized and intensified. The simultaneous excitation of transverse electric (TE) and transverse magnetic (TM) modes in the 2D helicoid crystal when subjected to circularly polarized light (CPL) incidence was substantiated via our photonic band diagram analysis in Chapter 3.1.1. This simultaneous excitation engendered a potent Circular Dichroism (CD) signal. However, this interpretation, although predicated on the photonic band diagram, is limited in its capacity to elucidate the helicity of the generated modes. In extreme cases, if the formed TE and TM modes under CPL incidence have a phase difference of 0 or $\pi$, the modes may resemble characteristics of linearly polarized light tilted at 45 degrees. Conversely, if the phase difference is $\pm\pi$, the modes may manifest attributes synonymous with CPL (Figure 3. 4).

In response to these nuances, we undertook a meticulous phase analysis of the TE and TM modes generated within the 2D helicoid crystal. To achieve this, we derived the electric dipoles ($\mathbf{p}$)[168–170] of individual helicoid particles – the underlying cause for the formation of each mode – through electromagnetic simulation. The helicoid dipole $\mathbf{p}$ was induced following the equation,

$\mathbf{p} \equiv \int \varepsilon_0(\varepsilon_{Au}-1)\mathbf{E}(\mathbf{r})dV$. Our aim was to discern the phase disparity between helicoid dipoles induced in the TE and TM directions (Figure 3. 5).

Our investigation disclosed that the helicoid dipoles in the TE and TM directions within the Localized Surface Plasmon Resonance (LSPR) spectral region (~600 nm), demonstrated a phase difference of 0 or π under LCP and RCP incidence. This revealed attributes akin to linearly polarized light. Contrastingly, within the Near-Infrared (NIR) wavelength region, where collective resonance is apparent, the phase difference between the two helicoid dipoles conveyed characteristics akin to CPL, exhibiting a phase difference of ±π (Figure 3. 6).

This insight led us to conclude that the helicoid dipoles, within the wavelength region corresponding to collective resonance, display temporal spin dynamics akin to CPL. As a consequence of this spin, the electric field ($\mathbf{E}_{sca}$) scattered from these dipoles also demonstrates rotational motion (Figure 3. 7). The induction of such helically polarized light within the 2D helicoid crystal fosters the generation of light with high optical helicity density[101].

In a simulated analysis calculating the optical helicity density, we substantiated that the LSPR band, presenting linearly polarized light features, resulted in optical helicity with non-uniform signs. However, owing to the rotational motion of the helicoid dipoles, collective resonance induced a two-dimensional uniform and pronounced optical helicity density (Figure 3. 8). This comprehensive study underscores the ability of the 2D helicoid crystal to effectively induce and manipulate optical helicity density, indicating its promising implications in the realm of chiral sensing.

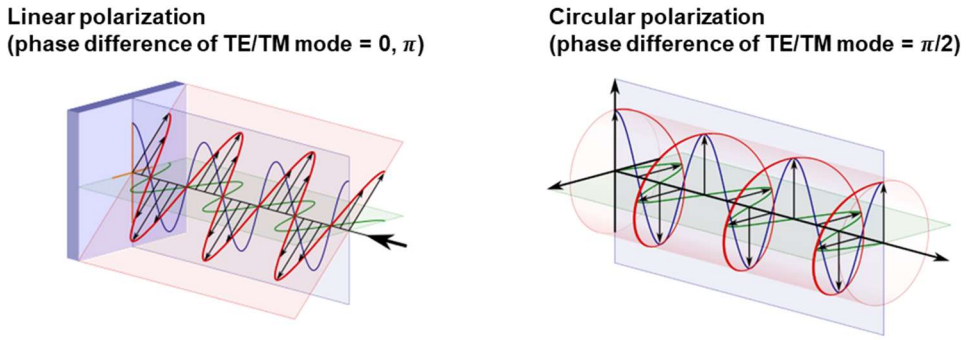


Figure 3. 4 Schematic illustration showing two different polarization states of field (linear and circular polarized field).

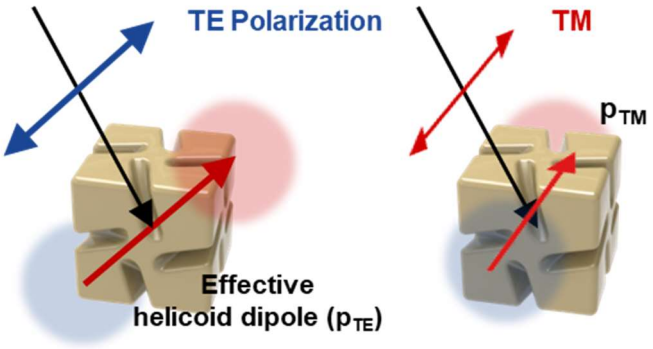


Figure 3. 5 Schematic illustration of helicoid dipoles along transverse electric (TE) and transverse magnetic (TM) directions.

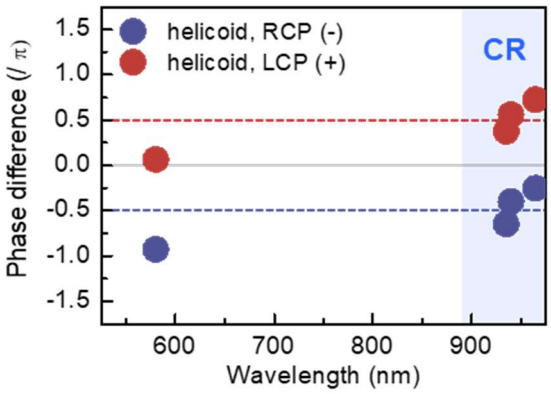


Figure 3. 6 Phase difference between helicoid dipoles along TE/TM directions.

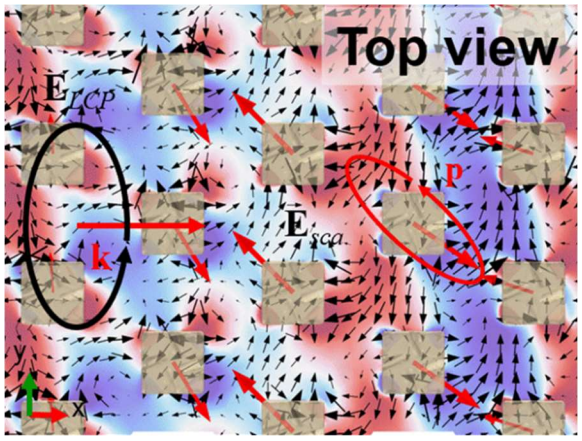


Figure 3. 7 Simulated effective dipole of helicoids. The helicoid dipole (**p**) and scattered electric field vector ($\mathbf{E}_{sca}$) spins like CPL.

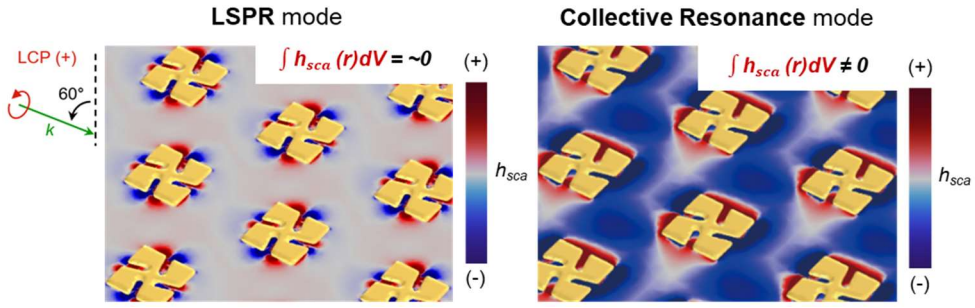


Figure 3. 8 Optical helicity density ($h$) of 2D helicoid crystal at LSPR and collective resonance mode wavelengths.

## 3.2 Chiral Perturbation Theory

In order to apply the significant optical helicity observed in our studies to chiral sensing, we first conducted an investigation to elucidate the implications of the optical helicity density of the 2D helicoid crystal in the context of chiral sensing. According to prevailing theories on molecular Circular Dichroism (CD) amplification, the uniform optical helicity of a 2D helicoid crystal could potentially induce a powerful enhancement of molecular CD. This amplification could lead to performance capabilities that transcend the limitations of conventional chiral sensors. However, these theories regarding molecular CD amplification have conspicuous limitations: not only do they fail to account for the resonance separation between molecules and plasmonic materials, but they also neglect factors that could modulate the energy of plasmonic materials, such as the refractive index of the molecules[21,56].

In an attempt to more accurately define the characteristics of chiral sensors induced by optical helicity density, we have endeavored to formulate a novel theoretical framework. Rather than relying on theories of molecular CD amplification, our proposed theory is premised on perturbation theory[68], which describes the influence of a molecule's refractive index on the resonance of plasmonic materials. This perspective allows us to precisely elucidate the impact of a molecule's chirality on the resonance characteristics of plasmonic materials.

In our comprehensive approach, we aim to circumvent the limitations of existing theories, providing a more holistic understanding of the complex interplay between optical helicity, molecular chirality, and plasmonic resonance. By doing so, we hope to shed light on the potential of 2D helicoid crystals in advancing the

field of chiral sensing and significantly enhancing the sensitivity and performance of chiral sensors.

In accordance with established perturbation theory, there is a strong correlation between the resonance frequency $\omega_0$ of the electromagnetic mode $\{\tilde{\mathbf{E}}, \tilde{\mathbf{H}}\}$ and the amount of energy stored in the mode. When molecules are introduced in the proximity of the optical resonator, a redistribution of energy between the resonant mode and these molecules transpires. This leads to a shift in the mode ($\delta\omega_0$) as well as a perturbation in the strength of the mode ($\delta a$). For the purpose of enantioselective sensing, we present an analytical expression of the mode shift $\delta\omega_0$ and the perturbed mode strength $\delta a$ in terms of the inherent characteristics of the mode.

We can represent the complete electromagnetic field of the cavity and its dielectric surrounding with

$$U = U_{cav} + U_{env} = \frac{1}{2} Re \int_{cav} \frac{\partial(\omega\varepsilon_{cav})}{\partial\omega} \left|\tilde{\mathbf{E}}\right|^2 dV + \frac{1}{2} Re \int_{env} \varepsilon_{env} \left|\tilde{\mathbf{E}}\right|^2 dV, \qquad \text{(Eq 3. 1)}$$

where $\varepsilon_{cav}$ and $\varepsilon_{env}$ denote the permittivity of the cavity and the environment, respectively. We consider that the environment does not demonstrate temporal dispersion, thus $\partial(\omega\varepsilon_{env})/\partial\omega = \varepsilon_{env}$. The introduction of chiral molecules to the environment for enantioselective sensing can be represented electromagnetically as minute changes in $\varepsilon_{env}$ and the introduction of the chirality parameter $\kappa_{env}$. Thus, the environment can be described by the subsequent constitutive relations of the chiral media,

$$\tilde{\mathbf{D}} = \varepsilon_{env}\tilde{\mathbf{E}} + i\kappa_{env}\sqrt{\varepsilon_0\mu_0}\tilde{\mathbf{H}}, \qquad \text{(Eq 3. 2)}$$

$$\tilde{\mathbf{B}} = \mu_{env}\tilde{\mathbf{H}} - i\kappa_{env}\sqrt{\varepsilon_0\mu_0}\tilde{\mathbf{E}}. \qquad \text{(Eq 3. 3)}$$

By adding molecules, the environment changes and this triggers a corresponding change in the total energy stored in the cavity and the environment; $\delta U$=$\delta U_{cav}$+$\delta U_{env}$, where $\delta$ symbolizes changes in the energy terms. As per the result of dielectric perturbation theory[68], the first term $\delta U_{cav}$ is given by

$$\delta U_{cav} = \delta\omega \, Re \left.\frac{\partial \varepsilon_{cav}}{\partial \omega}\right|_{\omega=\omega_0}. \qquad \text{(Eq 3. 4)}$$

The derivation of the second term $\delta U_{env}$ is complex as the constitutive relations of the environment transition into those of the chiral medium, Eqs 3. 2 and 3. We propose a simplification of $\delta U_{env} = \delta Re \int_{env}\left(\widetilde{\mathbf{D}} \cdot \tilde{\mathbf{E}}^* + \widetilde{\mathbf{B}} \cdot \widetilde{\mathbf{H}}^*\right)dV$ /4 into

$$\delta U_{env} = \frac{1}{2}\delta \int_{env}\{Re\varepsilon_{env}\left|\tilde{\mathbf{E}}\right|^2 + \kappa_{env}\sqrt{\epsilon_0\mu_0}Im(\tilde{\mathbf{E}} \cdot \widetilde{\mathbf{H}}^*)\}dV \qquad \text{(Eq 3. 5)}$$

using quasistatic identities[171],

$$\int_{cav}\widetilde{\mathbf{D}} \cdot \tilde{\mathbf{E}}^* dV + \int_{env}\widetilde{\mathbf{D}} \cdot \tilde{\mathbf{E}}^* dV = 0, \qquad \text{(Eq 3. 6)}$$

$$\int_{cav}\widetilde{\mathbf{D}}^* \cdot \tilde{\mathbf{E}} dV + \int_{env}\widetilde{\mathbf{D}}^* \cdot \tilde{\mathbf{E}} dV = 0, \qquad \text{(Eq 3. 7)}$$

which are applicable only when $\nabla \times \mathbf{E} = 0$ and $\mathbf{E} = -\nabla\Phi$.

When we combine the constitutive relations with two given equations (Eqs 3. 2, 3 and 3. 6, 7), two additional equations are produced.

$$\int_{cav}\varepsilon_{cav}\left|\tilde{\mathbf{E}}\right|^2 dV + \int_{env}\varepsilon_{env}\left|\tilde{\mathbf{E}}\right|^2 dV + \int_{env} i\kappa_{env}\sqrt{\varepsilon_0\mu_0}\tilde{\mathbf{E}}^* \cdot \widetilde{\mathbf{H}} dV = 0, \qquad \text{(Eq 3. 8)}$$

$$\int_{cav}\varepsilon^*_{env}\left|\tilde{\mathbf{E}}\right|^2 dV + \int_{env}\varepsilon^*_{env}\left|\tilde{\mathbf{E}}\right|^2 dV - \int_{env} i\kappa^*_{env}\sqrt{\varepsilon_0\mu_0}\tilde{\mathbf{E}} \cdot \widetilde{\mathbf{H}}^* dV = 0 \qquad \text{(Eq 3. 9)}$$

Summation of these gives

$$\int_{cav} Re\, \varepsilon_{cav}\left|\tilde{\mathbf{E}}\right|^2 dV + \int_{env}\left\{Re\, \varepsilon_{env}\left|\tilde{\mathbf{E}}\right|^2 + \kappa_{env}\sqrt{\varepsilon_0\mu_0}\, Im\left(\tilde{\mathbf{E}} \cdot \widetilde{\mathbf{H}}^*\right)\right\}dV = 0, \qquad \text{(Eq 3. 10)}$$

assuming the chirality parameter of chiral molecules does not have an imaginary part, *i.e.,* $\kappa_{env}=\kappa_{env}^{*}$. Most chiral molecules meet this condition in the visible and near-infrared frequencies because they show optical rotatory dispersion (ORD) alone and not circular dichroism (CD). By taking derivatives, Eq 3. 10 transforms into

$$\delta \int_{env} \left\{ Re\, \varepsilon_{env} \left|\tilde{\mathbf{E}}\right|^2 + \kappa_{env}\sqrt{\varepsilon_0\mu_0}\, Im\left(\tilde{\mathbf{E}} \cdot \tilde{\mathbf{H}}^*\right) \right\} dV = -\delta\, Re\, \varepsilon_{cav}. \quad \text{(Eq 3. 11)}$$

, allowing us to express the changed energy in the environment $\delta U_{\text{env}}$ in

$$\delta U_{env} = -\frac{1}{2} Re\, \delta\, \varepsilon_{cav} = -\frac{1}{2}\delta\omega\, Re \frac{\partial \varepsilon_{cav}}{\partial \omega}. \quad \text{(Eq 3. 12)}$$

Consequently, we can express the total energy change in a simplified form.

$$\delta U = \delta U_{cav} + \delta U_{env} = \frac{1}{2}\delta\omega_0\, Re \left.\frac{\partial \varepsilon_{cav}}{\partial \omega}\right|_{\omega=\omega_0}. \quad \text{(Eq 3. 13)}$$

This change in the energy of cavity $\delta U_{\text{cav}}$ should be changed by the additional molecule introductions. The energy captured by the chiral molecule $\delta U_{\text{mol}}$ can be represented by

$$\delta U_{mol} = -\frac{1}{2}\sum_i Re\left(\tilde{\mathbf{p}}_i \cdot \tilde{\mathbf{E}}_i^* + \tilde{\mathbf{m}}_i \cdot \tilde{\mathbf{H}}_i^*\right), \quad \text{(Eq 3. 14)}$$

where **p** and **m** are the electric and magnetic dipole moment, respectively. The subscript *i* denotes the moments of the *i*-th molecule and the fields of the *i*-th molecular position. Because of the molecular chirality, chiral molecules also have constitutive relations,

$$\tilde{\mathbf{p}} = \alpha_e \tilde{\mathbf{E}} + iG\tilde{\mathbf{H}}, \quad \text{(Eq 3. 15)}$$

$$\tilde{\mathbf{m}} = \alpha_m \tilde{\mathbf{H}} - iG\tilde{\mathbf{E}} \approx -iG\tilde{\mathbf{E}}, \quad \text{(Eq 3. 16)}$$

where $\alpha_{\text{e}}$, $\alpha_{\text{m}}\approx 0$, and *G* are the electric polarizability, the magnetic polarizability, and the chiral polarizability, respectively.

allowing us to substitute them into our energy equation to obtain additional equations. Substituting the Eq 3. 14 with Eqs 3. 15 and 16 yields

$$\delta U_{mol}(\mathbf{r}_{mol}) = -\frac{1}{2}\sum_i \left\{\alpha_{e,i}\left|\tilde{\mathbf{E}}_i\right|^2 + 2G_i\, Im\left(\tilde{\mathbf{E}}_i \cdot \tilde{\mathbf{H}}_i^*\right)\right\}. \quad \text{(Eq 3. 17)}$$

Near the resonance frequency $\omega_0$ of the mode $\{\tilde{\mathbf{E}}, \tilde{\mathbf{H}}\}$, the scattered field can be approximated and yields $\mathbf{E}_{sca}(\omega \approx \omega_0) \approx a(\omega = \omega_0)\tilde{\mathbf{E}}$, $\mathbf{H}_{sca}(\omega \approx \omega_0) \approx a(\omega = \omega_0)\tilde{\mathbf{H}}$ and

$$\delta U_{mol}(\mathbf{r}_{mol}) = -\frac{\alpha_e|\mathbf{E}_{sca}|^2}{2\int_{cav}|\mathbf{E}|^2 dV\big|_{\omega=\omega_0}} - \frac{2G\, Im(\mathbf{E}_{sca}\cdot\mathbf{H}_{sca}^*)}{2\int_{cav}|\mathbf{E}|^2 dV\big|_{\omega=\omega_0}}, \quad \text{(Eq 3. 18)}$$

since the strength of mode $a$ intensified[171].

As discussed, the changes in the cavity energy (Eq 3. 13) and molecule energy (Eq 3. 18) are the same. This equivalence allows us to derive an equation,

$$\delta\omega_0 = -\frac{\sum_i \alpha_{e,i}|\mathbf{E}_{sca}|^2}{\int_{cav}(\partial\varepsilon_{cav}/\partial\omega)|\mathbf{E}_{sca}|^2 dV\big|_{\omega=\omega_0}} - \frac{\sum_i 2G_i\, Im(\mathbf{E}_{sca}\cdot\mathbf{H}_{sca}^*)}{\int_{cav}(\partial\varepsilon_{cav}/\partial\omega)|\mathbf{E}_{sca}|^2 dV\big|_{\omega=\omega_0}}, \text{(Eq 3. 19)}$$

and by replacing the summation with integration, $\alpha_e|\mathbf{E}_{sca}|^2 \rightarrow \int_{env}\Delta\varepsilon|\mathbf{E}_{sca}(\mathbf{r})|^2 dV$ and $2G\, Im(\mathbf{E}_{sca}\cdot\mathbf{H}_{sca}^*) \rightarrow \int_{env} 2\Delta\kappa\, Im(\mathbf{E}_{sca}\cdot\mathbf{H}_{sca}^*)(\mathbf{r})dV/c$, when $\Delta\varepsilon$ denotes the permittivity change of the environment, we obtain the analytic expression for the mode shift by chiral molecule analytes

$$\delta\omega_0 = -\frac{\int_{sensor}\Delta\varepsilon|\mathbf{E}_{sca}(\mathbf{r})|^2 dV}{\int_{cav}\left(\frac{\partial\varepsilon_{cav}}{\partial\omega}\right)|\mathbf{E}_{sca}(\mathbf{r})|^2 dV} - \frac{(2/c)\int_{sensor}\Delta\kappa\, Im(\mathbf{E}_{sca}\cdot\mathbf{H}_{sca}^*)(\mathbf{r})dV}{\int_{cav}\left(\frac{\partial\varepsilon_{cav}}{\partial\omega}\right)|\mathbf{E}_{sca}(\mathbf{r})|^2 dV} \equiv \delta\omega_0^{(n)} + \delta\omega_0^{(\kappa)}$$

(Eq 3. 20).

We can consider two factors in Eq 3. 20 as the frequency shifts induced by dielectric ($\delta\omega_0^{(n)}$) and chirality ($\delta\omega_0^{(\kappa)}$) changes in the environment, respectively. This mode shift is related to the perturbation of the mode strength $a(\omega)$. We can note the general expression for the mode strength $a(\omega)$ by the Lorentz reciprocity theory[34]

$$a(\omega_0) = -iQ\frac{\int_{all}\{(\varepsilon-\varepsilon_0)|\mathbf{E}_{sca}|^2+2\kappa\, Im(\mathbf{E}_{sca}\cdot\mathbf{H}^*_{sca})/c\}dV}{\int_{all}\{\partial(\omega\varepsilon)/\partial\omega\}|\mathbf{E}_{sca}|^2dV\big|_{\omega=\omega_0}}. \quad \text{(Eq 3. 21)}$$

The integration range includes the volume of cavity (*cav*) and the environment (*env*). We follow the Drude model for the permittivity of the metallic cavities, *i.e.* $\varepsilon_{cav}=1-\omega_p^2/\omega^2$ ($\omega\partial\varepsilon/\partial\omega=2(\omega_p^2/\omega^2)$ and $\partial(\omega\varepsilon)/\partial\omega=1+(\omega_p^2/\omega^2)\approx\omega_p^2/\omega^2=(\omega\partial\varepsilon/\partial\omega)/2$), and assume most of the electromagnetic energy is stored inside the cavity. Therefore, Eq 3. 21 becomes

$$a(\omega_0) = -2iQ\frac{1}{\omega_0}\frac{\int_{all}\{(\varepsilon-\varepsilon_0)|\mathbf{E}_{sca}|^2+2\Delta\kappa\, I\quad(\mathbf{E}_{sca}\cdot\mathbf{H}^*_{sca})/c\}dV}{\int_{cav}(\partial\varepsilon/\partial\omega)|\mathbf{E}_{sca}|^2dV\big|_{\omega=\omega_0}}. \quad \text{(Eq 3. 22)}$$

Also, we can write the perturbation in mode strength, $\delta a=\delta a^{(n)}+\delta a^{(\kappa)}$, where change in mode strength by dielectric and chirality parameter changes

$$\delta a^{(n)} = -2i\frac{Q}{\omega_0}\frac{\int_{all}\Delta\varepsilon|\mathbf{E}_{sca}|^2dV}{\int_{cav}(\partial\varepsilon/\partial\omega)|\mathbf{E}_{sca}|^2dV\big|_{\omega=\omega_0}} = 2iQ\frac{\delta\omega_0^{(n)}}{\omega_0}, \quad \text{(Eq 3. 23)}$$

$$\delta a^{(\kappa)} = -2iQ\frac{1}{\omega_0}\frac{2\int_{all}\Delta\kappa\, Im(\mathbf{E}_{sca}\cdot\mathbf{H}^*_{sca})dV/c}{\int_{cav}(\partial\varepsilon/\partial\omega)|\mathbf{E}_{sca}|^2dV\big|_{\omega=\omega_0}} = 2iQ\frac{\delta\omega_0^{(\kappa)}}{\omega_0}, \text{ respectively.} \quad \text{(Eq 3. 24)}$$

According to the aforementioned chiral perturbation theory, Eq 3. 20 can be written in terms of the optical helicity density ($h$) as it corresponds to Im(**E**·**H***) present in Eq 1.5. Furthermore, the shift in the plasmonic resonance frequency induced by chiral molecules can also be represented as an energy variation in the plasmonic material. Therefore, this complex phenomenon can be succinctly encapsulated in the following mathematical formula,

$$\frac{\Delta E_{\pm}(\Delta\kappa)}{\Delta E_{0,\pm}} = -\left.\frac{8\Delta\kappa\int_{sensor}h_{\pm}(\mathbf{r})dV}{\int_{Au}(\partial\varepsilon_{Au}/\partial\omega)|\mathbf{E}_{\pm,sca}|^2dV}\right|_{\omega=\omega_{0,\pm}} \quad \text{(Eq 3. 25)},$$

where the subscripts + and - are for LCP and RCP, $\varepsilon_{Au}$ corresponds to the Au permittivity, $\kappa$ describes the chirality parameter of the molecules (the chirality

parameter of $\kappa>0$, $\kappa<0$, and $\kappa=0$ matches to L-, D-molecules, and their racemic mixture), respectively.

The derived analytic formula yields two pivotal insights. Firstly, it underscores the significance of both the magnitude and uniformity of the scattered optical helicity density, $h_{sca}(\mathbf{r})$. Secondly, the polarity of the chiral energy shift is ascertained by the product of two pseudoscalars: the change in chirality, $\Delta\kappa$, and the integral of the scattered helicity over the volume, $\int h_{sca}(\mathbf{r})dV$. As delineated in Figure 3.9, $h_{sca}(\mathbf{r})$ inverts its sign in response to circularly polarized light (CPL) excitations of opposing handedness. Further, the chiroptical response exhibited by our helicoids, characterized by a preferential reaction to right-handed circularly polarized (RCP) light, engenders an asymmetric distribution of $h_{sca}(\mathbf{r})$. Consequently, we observe four distinct energy shifts in the collective resonances (CRs). These include: i) a positive energy shift for a positive change in chirality under RCP light, $\Delta E_{+}$ $(+\Delta\kappa)>0$; ii) a negative shift under the same light for a positive chirality change, $\Delta E_{-}$ $(+\Delta\kappa)<0$; iii) a negative shift for a negative change in chirality under RCP light, $\Delta E_{+}$ $(-\Delta\kappa)<0$; and iv) a positive shift under RCP light for a negative chirality change, $\Delta E_{-}$ $(-\Delta\kappa)>0$, which yields sensitive shift in collective resonance for chiral molecules with negative chirality parameter (D-molecules). These observations are the resultant interplay between two opposing CPL excitations (indicated by the subscripts ±) and the two chiral variants ($\pm\Delta\kappa$), as demonstrated in Figure 3.10.

We unveil an intriguing phenomenon in which, given a specific enantiomer variation $\Delta\kappa$, the chiral energy shifts invariably exhibit opposing tendencies for the two circular polarizations. This is because the energy shifts under CPL of either handedness, $\Delta E_{\pm}$ $(\Delta\kappa)$, are directly proportional to the product of the change in chirality and the integrated scattered helicity, i.e., $\Delta E_{\pm}(\Delta\kappa)\propto\Delta\kappa\int(h_{\pm,sca}(\mathbf{r})\mathrm{dV})$.

Through the comprehensive investigations conducted in this Chapter, a rigorous and profound understanding of the pronounced chiroptic response

demonstrated by the two-dimensional (2D) helicoid crystal nanostructures, fabricated and characterized through rigorous experimental procedures, has been accomplished. The intrinsic chirality associated with the helicoid, emerging from its unique 432 symmetry, was found to retain its chiral characteristics, undeterred by the complexities induced by the coupling interactions among 2D nanostructures, even when subjected to collective resonances.

Our investigation further uncovered the roots of the robust chiroptic response elicited under the influence of incident plane-polarized light, inclined at an angle of 60 degrees, manifesting during the collective resonance conditions. Our analysis highlighted that this phenomenon is attributable to the concurrent excitation of both transverse electric (TE) and transverse magnetic (TM) modes within the spatial confines of the 2D helicoid crystal structure, thereby intensifying the interactive response with the incident CPL.

The resulting amplification of this interaction incites a collective spinning motion in the helicoid dipoles at the collective resonant wavelength, a cascading effect of which is the induced rotational dynamism in the surrounding scattered electric field vectors. This intricate chain of events culminates in the emanation of light characterized by an optical helicity density that is both uniform and potent in its spatial distribution.

Not content with just this groundbreaking discovery, we further augmented our theoretical breakthroughs by developing the chiral perturbation theory aimed at exploiting the inherently strong and uniform optical helicity density exhibited by the 2D helicoid crystal structure for tangible chirality sensing applications. Through this theoretical paradigm, we've validated that the implementation of the robust and uniform optical helicity properties inherent to the 2D helicoid crystal structure could significantly enhance chiral sensitivity. Moreover, this theoretical construct has endowed us with the capability to predict, with scientific precision, variations in

collective resonance and circular dichroism (CD) contingent upon the molecular chirality.

Considering these pivotal findings and armed with this advanced theoretical understanding, we anticipate dedicating the forthcoming Chapter to a thorough experimental exploration with a focus on potential applications of the 2D helicoid crystals in the domain of chirality sensing.

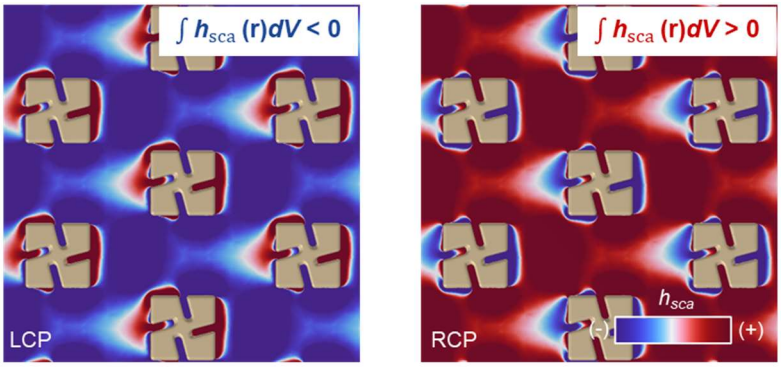


Figure 3. 9 Optical helicity density ($h$) of 2D helicoid crystal with Left and right circularly polarized light illumination.

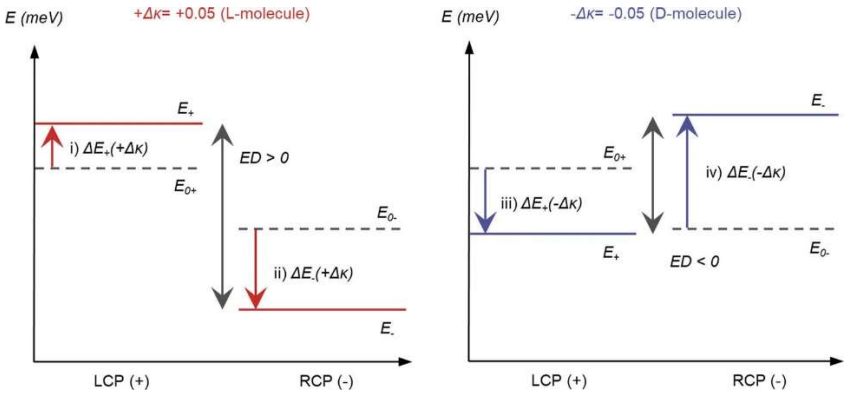


Figure 3. 10 Change in energy of 2D helicoid crystal for the combination of two parameters, handedness of light and chirality parameters ($\Delta\kappa$).

# Chapter 4. Molecular Chirality Sensing Using Collective CD of 2D Helicoid Crystal

## 4.1 Enantioselective collective CD response for proline molecules

The practical application of our fabricated chiral plasmonic structures for the purpose of chiral sensing represents an imperative stride forward in this field, one that elevates the value of chiral plasmonic sensors beyond merely theoretical conjectures or academic postulations. Notably, prior advancements in this area, based on chiral plasmonic structures, have largely remained confined within the theoretical realm or have restricted their experimental validations to only demonstrating chiral sensing capabilities under specific conditions. More often than not, these validations involved the measurement of molecules at relatively high concentrations, coated or deposited on plasmonic structures[24,49]. This approach was primarily taken to boost the signal of the molecules themselves, rather than showcasing the versatility of the sensor performance across a broad spectrum of chiral molecule concentrations. In contrast to this, we has extended beyond merely ratifying the chiral sensor performance of the 2D helicoid crystal, which is based on the relatively simple parameter of optical helicity density, on a theoretical level. Rather, we have undertaken an ambitious pursuit to experimentally validate whether this chiral sensor can indeed deliver effective performance across various molecular concentrations within practical, real-world scenarios.

As outlined in this Chapter, we has been geared towards ascertaining if our 2D helicoid crystal can indeed fulfill its role as a reliable chiral sensor across diverse molecular concentrations. We view this step as an integral part of our quest to cement the foundation for the practical application of 2D helicoid crystal as a truly functional

chiral sensor. In essence, this robust experimental validation seeks to bridge the chasm that often exists between theoretical expectations and practical implementations. By systematically analyzing the performance of our chiral sensor across a multitude of molecular concentrations, we offer a promising pathway to enhance the functionality and widen the applicability of chiral plasmonic sensing technology. This undertaking can pave the way towards comprehensive chiral analysis in numerous scientific and industrial applications. This expansion into practical applications will not only bolster the utilization of chiral plasmonic sensors but also inspire further innovations and advancements in this dynamic field.

### 4.1.1 Collective CD response of 2D helicoid crystal for proline

This Chapter discusses the experimental setup and subsequent findings relating to enantioselective sensing ability of 2D helicoid crystal. For this study, a 2D helicoid crystal was set up inside a cuvette with an 8.9 mm path length. Within this cuvette, solutions of either L- or D-proline were introduced (Figure 4. 1). Specifically, we started the experiment by loading the 2D helicoid crystal onto a quartz slide, a robust and transparent material ideal for optical applications. The dimensions of this slide were 1 $cm^2$, which provided an adequate surface area for the crystal to be loaded on. Once the helicoid crystal was securely positioned on the quartz slide, the slide was then placed in a specially fabricated sample holder. The sample holder was designed with a tilt of 60 degrees and was created using a 3D printer (uPrint SE, Stratasys). This specialized holder is crucial to position the slide in the intended orientation and maintain the desired position throughout the experiment. Next, the holder, along with the loaded slide, was carefully installed into a quartz cuvette for subsequent measurements. The cuvette was specifically chosen from Hellma Analytics (HE.101. QS10), well-regarded for its precision and quality. The cuvette had a size of 10 mm by 10 mm, which was a fitting size to accommodate

the slide and its holder. The final part of the setup involved aligning the optical path of light that would pass through the molecules. We precisely fixed this optical path to be approximately 8.9 mm. This optical path length is vital as it dictates the volume of sample the light will interact with, thus affecting the intensity and quality of the results obtained from the experiment.

In the CD measurement conducted in this set-up[11], we discerned that with the increasing concentration of either L- or D-proline, there was a significant redshift in the spectral positions of the collective CD peak and dip (as graphically represented in Figure 4. 2). The term "redshift" in this context refers to the spectral shift towards longer wavelengths or lower frequencies within the electromagnetic spectrum. Interestingly, the localized surface plasmon resonance (LSPR) CD dip position remained virtually static, notwithstanding the increasing proline concentration. We noted an intriguing phenomenon: the spectral position and intensity of the collective CD exhibited asymmetric shifts correlating with the chirality (handedness) of the proline molecules. Particularly, we observed that the presence of D-proline induced larger redshifts and intensity changes as opposed to when L-proline was utilized.

The aforementioned findings can primarily be elucidated through the chiral perturbation theory which is delineated in Chapter 3, which is fundamentally derived from the inherent mode splitting and enantioselective response in collective resonance of 2D helicoid crystal. In addition, we discovered that these shifts in both spectral position and intensity led to the modulation of the CD, signified as ΔCD in our study. ΔCD is defined as the difference in CD spectra between the proline molecule under investigation and the baseline CD in deionized water ($CD_{Molecule}-CD_{DW}$).

To quantify the comprehensive spectral changes of the collective CD, we calculated the modulation range of $\Delta CD_{D\text{-}Pro}$ and $\Delta CD_{L\text{-}Pro}$. This was achieved by determining the difference between the ΔCD value at the peak and that at the dip as shown in Figure 4. 3 ($\Delta CD_{D\text{-}Pro,peak} - \Delta CD_{D\text{-}Pro,dip}$). The result of this calculation revealed that the modulation range was approximately 1.6 times greater than that of $\Delta CD_{L\text{-}Pro}$. This finding underscores a more pronounced effect of D-proline on the CD spectra in contrast to L-proline. Therefore, based on the aforementioned experimental setup and methodology, we have empirically validated the feasibility of analyzing molecular chirality through the evaluation of enantioselective circular dichroism (CD) responses that correspond to the chirality of proline molecules.

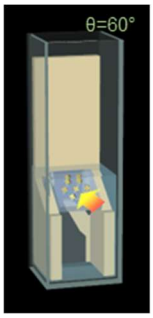


Figure 4. 1 Schematic illustration of 3D-printed holders for enantioselective sensing experiments.

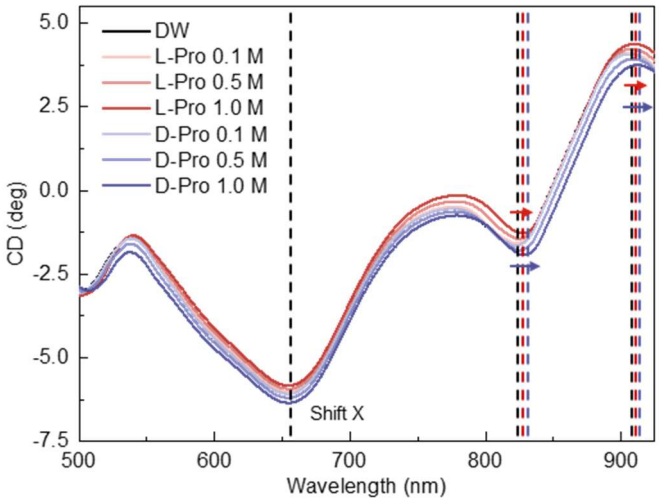


Figure 4. 2 CD spectra of 2D helicoid crystal for different medium (DI water, L-proline, D-proline).

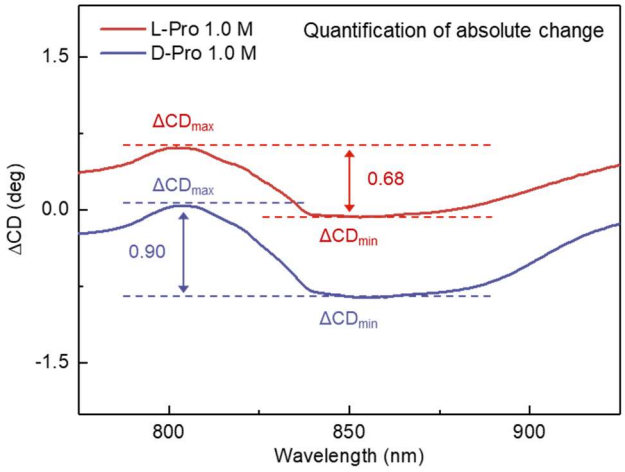


Figure 4. 3 ΔCD ($CD_{Molecule}$ – $CD_{DW}$) spectra of 2D helicoid crystal for L- and D-proline molecules.

### 4.1.2 Enantiomeric ratio and concentration determination by collective CD response

One of the remarkable attributes of our study, and indeed one that holds significant implications for the field of chiral analysis, is the unique capacity to employ the collective circular dichroism (CD) as a reliable analytical tool. This tool facilitates the simultaneous investigation of both the L/D ratio and concentration of an enantiomeric solution. It's noteworthy that the collective CD spectra showcase two disparate regions - Region I and Region II, indicated by red and blue circles respectively in our illustrations - each carrying its own distinct characteristics and responses to shifts in L- and D-proline concentrations (Figure 4. 4).

To elaborate, Region I, characterized by a negative slope in the collective CD spectra (marked by a red circle), reacts specifically to changes in the concentration of L-proline. In our study, an escalation in the L-proline concentration was seen to exclusively affect Region I, as signified by a red arrow in Figure 4. 4. On the other hand, Region II, marked by a positive slope in the collective CD spectra (highlighted by a blue circle), responds solely to changes in the concentration of D-proline. An increase in D-proline concentration was found to uniquely impact Region II, as shown by a blue arrow in the same figure.

This distinctive enantioselective spectral change observed in the CD spectra is a significant finding of our study, as it paves the way to precisely quantify the enantiomeric ratio (L/D ratio) in a racemic solution. This becomes especially evident in Fig. 3b, which presents a comprehensive suite of CD spectra corresponding to a wide range of molar ratios of L- to D-proline (extending from a ratio of 10:0 to 0:10). Here, the total proline concentration was held constant at 1 Molar (M).

An illustrative example can be seen in the case of a 1 M racemic solution with an equimolar ratio of 5:5 (represented by a purple line in the Figure 4. 5). We found that the CD spectrum for this solution was equivalent to the arithmetic mean of the CD spectra obtained from 1 M solutions of pure L-proline (denoted by a red line) and D-proline (indicated by a blue line).

From these experimental observations, we were able to derive empirical relationships linking the D-proline concentration (x), total concentration (y), and the shifted wavelength as shown by the red or blue circles in Fig. 3b (z). The relationships, in this specific instance, were $-16.2x+15.9y-z=0$ for Region I and $7.8x+8.5y-z=7.8$ for Region II (Figure 4. 6). These equations, borne out of empirical data, enable us to ascertain the molecular chirality and concentration with significant precision.

It's worth noting that these empirical relationships are not confined to proline molecules alone. Different equations might indeed be formulated for other chiral molecules, as we demonstrated in the case of L- and D-glucose (Figure 4. 7). This hints at the potential universality of our methodology, suggesting that our approach could potentially be extended to a broad spectrum of chiral molecules. This, in turn, augments the versatility and applicability of our study, reinforcing its standing in the realm of chiral analysis.

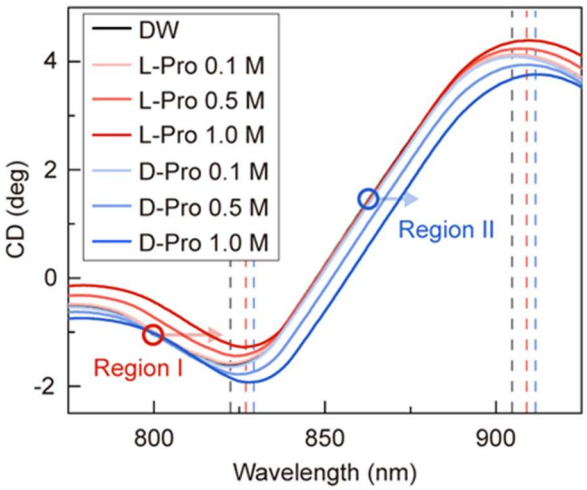


Figure 4. 4 Collective CD spectra for different concentration of L- and D-proline.

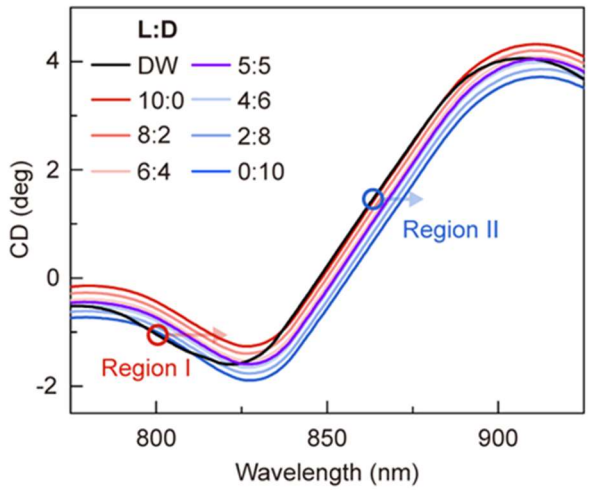


Figure 4. 5 Collective CD response for proline molecular solutions with different L/D proline ratios.

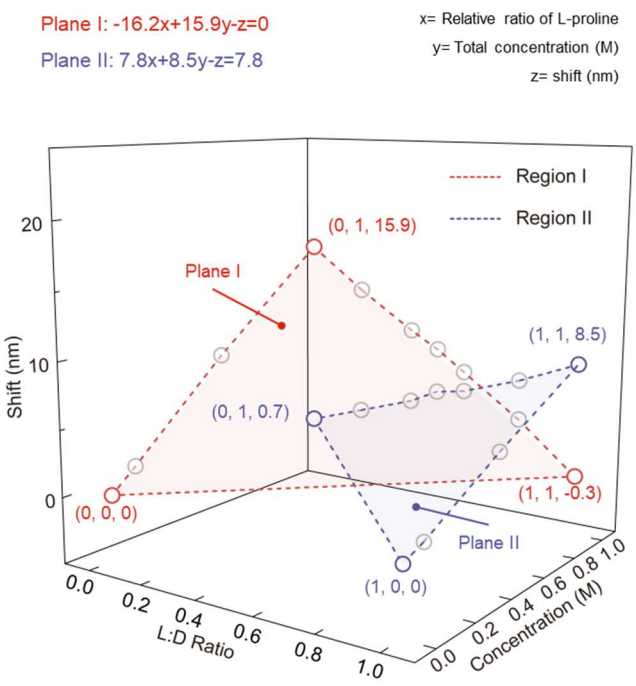


Figure 4. 6 Plane equations and corresponding plane graph showing the shift trend of Region I and II for different concentration and ratio of proline molecules.

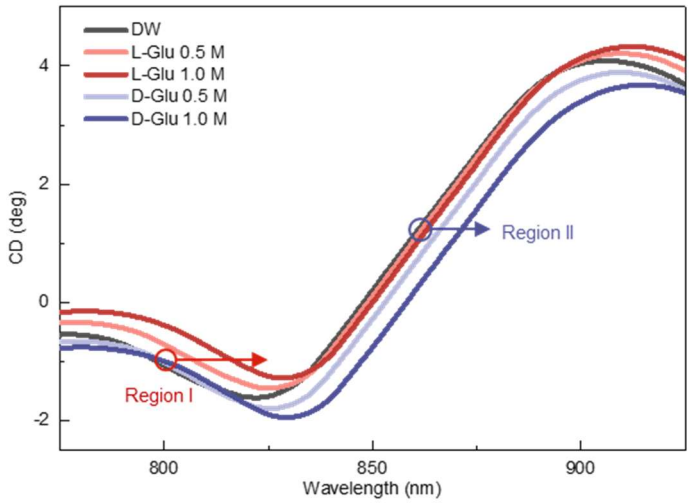


Figure 4. 7 Collective CD response of 2D helicoid crystal for chiral L- and D-glucose molecules

## 4.2 Colorimetric determination of molecular chirality

Harnessing the remarkable shift in the spectral characteristics of the collective CD, we have put forth a demonstration of a colorimetric chirality sensor. This particular sensor is capable of visually quantifying molecular chirality, essentially bringing the world of chiral molecules to the realm of observable phenomena. This approach rests on the principles of simple polarization colorimetry (Figure 4. 8), where wavelength-dependent rotation of linearly polarized light[65] occurs after it interacts with the 2D helicoid crystals containing chiral molecules. Chiral substances, by virtue of their unique properties, possess the capacity to rotate the axis of incident linearly polarized light, contingent upon their resonant wavelengths. Consequently, these substances can manifest unique polarization color distributions, depending upon the angle of the polarizer present at the analyzer stage. We observed that 2D helicoid crystals immersed in Deionized Water (DW) generated polarization colors such as light violet, purple, and red corresponding to analyzer angles of −2°, 0° and 2° respectively. In contrast, the Polydimethylsiloxane (PDMS) well did not yield any color (Figure 4.9).

As already corroborated through the CD spectra, the 2D helicoid crystals immersed in 1 M L-proline, racemic, and D-proline solutions exhibited distinct CD spectra. Therefore, the specific chiral molecular solvent in which the 2D helicoid crystal is placed dictates the resultant color distributions. In fact, during our measurements of polarization color distribution using L-, D-, and racemic proline (while changing the angle of the polarizer from −5° to 5°), we observed asymmetric trends in color generation in the 1 M L- and D-proline compared to the racemic solution (Figure 4. 10). These asymmetric color distribution trends can be vividly displayed on a chromaticity diagram (CIE 1931 color space). We can present the trajectory of the polarization color, as it changes with the rotation angle, as an

elliptical path on the chromaticity diagram (Figure 4. 11). Intriguingly, D-proline generates a trajectory that is shorter and more linear compared to L-proline, making the enantioselective optical response clearly discernible in the polarization colorimetry results.

In this Chapter, we have fundamentally showcased the potential of 2D helicoid crystals as the cornerstone of practical chiral sensing. Notably, our work stands as a testament to the fact that chiral sensing using 2D helicoid crystals is not only theoretically possible, but also demonstrably practical and versatile, thereby underlining the transformative potential of this approach to the broader landscape of chirality analysis. Through a systematic and iterative process of research and experimentation, we've been able to leverage the unique properties of 2D helicoid crystals to advance the domain of chiral sensing. We've shown that these remarkable structures can not only sense the presence of chiral molecules but also visually quantify the chirality of these molecules, making the intricate realm of molecular chirality more accessible and decipherable. This achievement substantially enhances the value proposition of chiral sensing based on 2D helicoid crystals. Moreover, our work has practical implications, offering a new lens to explore and analyze chiral molecules. Given the importance of chiral molecules in numerous scientific and industrial fields – from the development of new pharmaceuticals to the production of agricultural chemicals – this technology has the potential to revolutionize these fields. It could pave the way for more efficient processes in drug discovery and manufacturing, and it could facilitate new methods for identifying and analyzing chiral pollutants in the environment. On the path forward, our work is paving the way for advancements in the development of enantioselective sensors for the characterization of a wide range of chiral molecules, not just proline. Our experimental setup could be adapted to other chiral molecules, paving the way for broader applications of chiral sensing in various scientific and technological domains.

In conclusion, our experimental results, anchored in rigorous scientific inquiry, underscore the feasibility of practical chiral sensing using 2D helicoid crystals. This not only substantiates the value proposition of chiral sensing based on 2D helicoid crystals, but it also opens promising avenues for the real-world application of this technology, further underpinning its transformative potential for the field of chirality analysis.

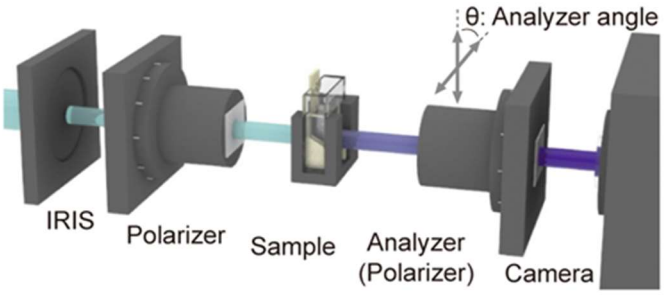


Figure 4. 8 Schematic illustration showing the optical set-up for observing polarization-resolved color distribution of chiral materials.

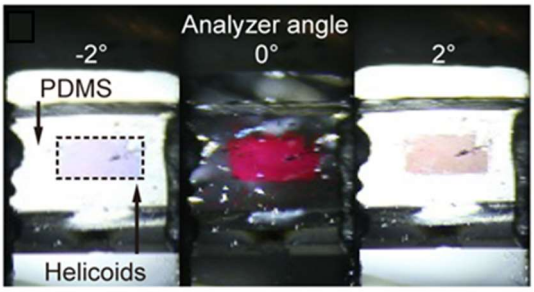


Figure 4. 9 Polarization-resolved color of 2D helicoid crystal for different analyzer angles.

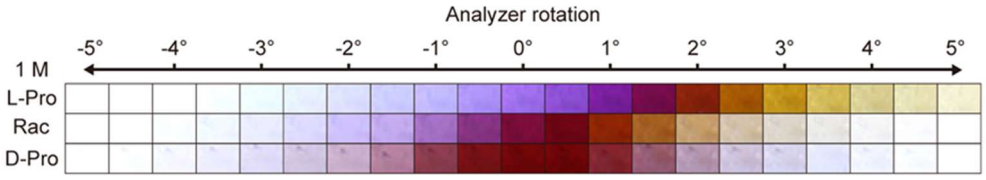


Figure 4. 10 Polarization-resolved color distribution of 2D helicoid crystal in 1 M L-, D-, and racemic proline solutions.

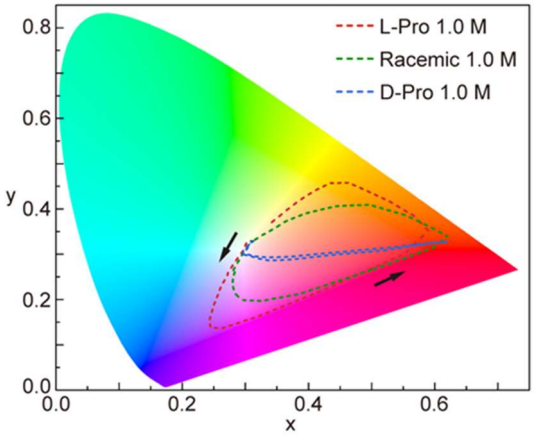


Figure 4. 11 CIE 1931 chromaticity diagram showing the change in polarization color of 2D helicoid crystal in 1 M L-, D-, and racemic proline solutions.

## 4.3 Application of collective CD for chiral sensing of micro-volume analyte

In Chapter 4.2, we demonstrated the successful execution of chiral sensing experiments on a 1.5 mL sample using 2D helicoid crystals. To extend the practical application of this technique to the sensing of diverse molecules, it is crucial to determine the detection limit. In fact, detection limit serves as a critical parameter for assessing the utility and efficacy of any chiral analysis technique and is particularly essential when the analysis technology is intended for industrial applications, such as in the pharmaceutical sector where extremely minute quantities of new drug molecules require precise chiral analysis. Taking advantage of the unique property of the optical helicity density of the collective resonance (CR) – which is spatially extended and confined within two dimensions – we can reduce the height of the channel while maintaining the chiral renormalization of the mode energy of the 2D helicoid crystal by the analyte. In this Chapter, we built upon the experiments and optical helicity density considerations outlined in Chapter 4.2, with the aim to discern the minimal effective concentration of proline molecules that can trigger a discernible enantiosensitive response, thereby gauging the detection capabilities of the 2D helicoid crystal.

We devised a microfluidic chamber that was 150 μm thick and could hold a volume of 15 μL, enclosing a 2D helicoid crystal within it. The fabrication process of the microfluidic chamber is visually demonstrated in Figure 4.12. Utilizing a 3D-printed mold, we developed a microfluidic chamber featuring an optical path of 150 μm thickness and a total volume of 15 μL. In this chamber, the intrinsic optical responses of proline in bulk solution are mitigated due to the reduced analyte volume. This allows the collective circular dichroism (CD) of the 2D helicoid crystal and its

robust coupling with the analyte to govern the enantioselective response, as illustrated in Figure 4.13. For quantifying the variation in mode strength induced by chiral molecules, we calculated ΔCD (defined as the difference between the CD of the molecule and that of deionized water), and evaluated the absolute value of ΔCD at the minima ($|\Delta CD_{min}|$) as shown in Figure 4. 14 and 15. Examining the ΔCD for L- and D-proline at concentrations of 10 and 100 mM, we noted that the sensitivity to D-proline exceeded that to L-proline, consistent with the observations made for the bulk solution. In experiments involving a broad concentration range spanning from $10^{-3}$ mM to $10^{2}$ mM, $|\Delta CD_{min}|$ progressively escalated from 0 mdeg to 57 mdeg for L-proline and 98 mdeg for D-proline, as captured in Figure 4.15.

Our efforts culminated in the achievement of a detection limit for D-proline of ~$10^{-1}$ mM in a volume of 15 μL, which is equivalent to a bulk refractive index unit (RIU) of $2\times10^{-6}$. This detection limit and sensitivity are comparable to those demonstrated by other cutting-edge nanophotonic sensors, such as localized surface plasmon resonance (LSPR)[166], surface plasmon resonance (SPR)[172], and metamaterial sensors[25], as summarized in Table 4.1. We confirmed this enantioselective response for numerical simulations. In our numerical simulation, we conceptualized the chiral molecule solution as a homogeneous medium with a refractive index ($n$) and a chirality parameter ($\kappa$). This enabled us to quantitatively represent the molecular concentration by leveraging the chiral Maxwell-Garnett formula[173]. As seen in Figure 4.16, the bisignate feature of ΔCD displayed more substantial changes for $\kappa<0$ (representing D-proline) compared to $\kappa>0$ (representing L-proline). Additionally, analogous trends in ΔCD were observed for a range of (n, κ) from (1.331, ±1.2×10-7) to (1.373, ±2.4×10-3), with higher $|\Delta CD_{min}|$ recorded for $\kappa < 0$, as depicted in Figure 4.17.

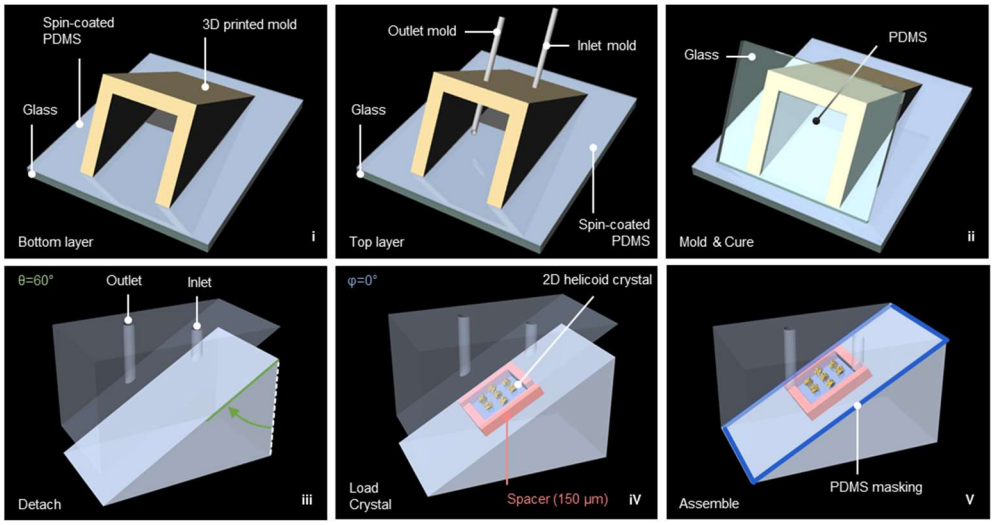


Figure 4. 12 Schematic illustration of fabrication of analyte chamber with micro-volume analyte. Two distinct triangular prism molds were crafted: the bottom layer (i, left), void of any inlet or outlet, and the top layer (i, right), equipped with both an inlet and an outlet, were formed by casting a 3D-printed mold in PDMS (ii). Upon removal from the mold, the fabricated structure displayed a 60° inclined angle for incident light (θ=60°) (iii). A 2D helicoid crystal with Γ-M (φ=0°) symmetry was then positioned on the bottom layer, followed by the placement of a 150 μm-thick spacer atop the 2D helicoid crystal (iv). Finally, all the components were assembled together, with PDMS used to seal the open space of the integrated structure (v).

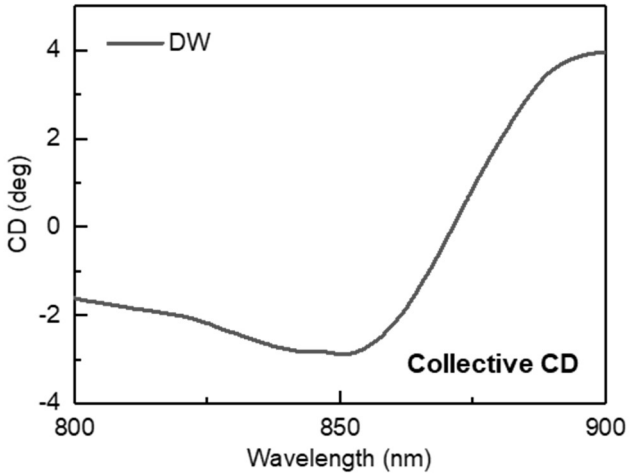


Figure 4. 13 Collective CD response of 2D helicoid crystal in micro-volume analyte chamber.

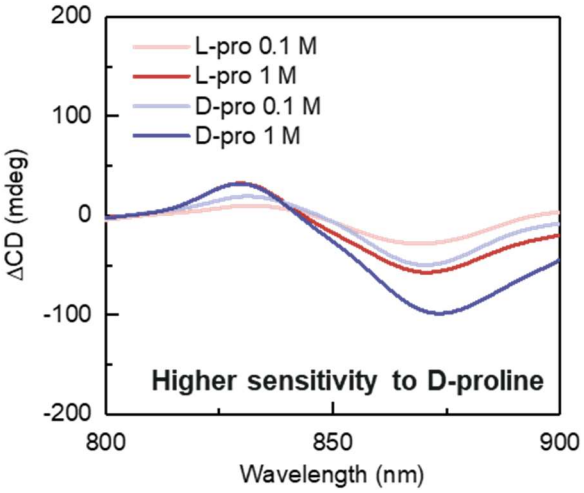


Figure 4. 14 ΔCD response of 2D helicoid crystal in micro-volume chamber for L- and D-proline.

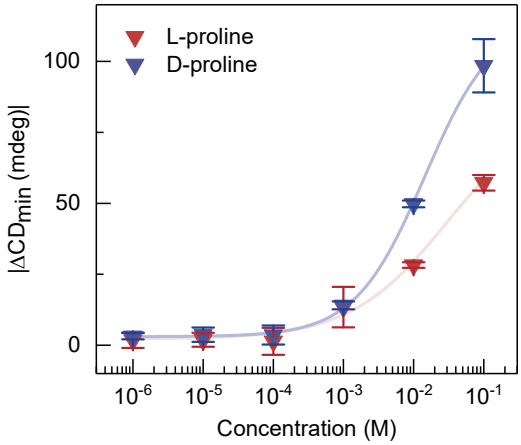


Figure 4. 15 $|\Delta CD_{min}|$ response of 2D helicoid crystal in micro-volume chamber for L- and D-proline.

| Method | Structure | Target | Detection range | | Enantio-selective range /Limit (M) |
|---|---|---|---|---|---|
| | | | Refractive Index | Concentration (M) | |
| Localized Surface Plasmon Resonance (LSPR) | Au nanosphere | Bulk glycerol | 1.333 - 1.459 ($10^{-3}$ resolution) | 0 - 10.858 | X |
| | Au nanocube | Bulk glycerol | 1.333 - 1.459 ($10^{-3}$ resolution) | 0 - 10.858 | |
| | Au nanorod | Bulk glycerol | 1.333 - 1.42 ($10^{-3}$ resolution) | 0 - 8.6864 | |
| Surface Plasmon Resonance (SPR) | Prism coupled Au/Cr thin fi lm | Bulk sucrose | 1.3328 - 1.3728 ($10^{-6}$ resolution) | 0 - 0.8 | |
| | Prism coupled Ag thin film | Bulk glycerol | 1.3330 - 1.3357 ($10^{-6}$ resolution) | 0 - 0.2 | |
| | DNA functionalized Au film | RNA 18-mers | * | $10^{-8}$ - 5 $\times 10^{-7}$ | |
| | DNA functionalized Au grating | MicroRNA-122 | * | $2 \times 10^{-10}$ - $5 \times 10^{-8}$ | |
| Hyperbolic metamaterial | Multilayered metal-insulator | Bovine Serum Albumin (BSA) adsorbate | * | $10^{-14}$ - $10^{-7}$ | |
| Plasmonic exceptional point | Layered Au nanorod array | Anti-Immunoglobulin G (Anti-IgG) adsorbate | * | $3 \times 10^{-17}$ - $1.5 \times 10^{-15}$ | |
| (Chiral) Metamaterials | Au cross array | Flavin mononucleotide adsorbate | * | $2.2 \times 10^{-3}$ | $2.2 \times 10^{-3}$ / * |
| | Au gammadion array | Bulk tryptophan | 1.3333 | $5 \times 10^{-3}$ | $5 \times 10^{-3}$ / * |
| | | Concanavalin A adsorbate | * | $3.77 \times 10^{-5}$ | $3.77 \times 10^{-5}$ / * |
| | Mechano-tunable Au colloidal assembly | Concanavalin A adsorbate | * | $3.77 \times 10^{-5}$ | $3.77 \times 10^{-5}$ / * |
| | Au twisted nanorod array | Bulk propanediol | 1.440 | 13.142 (Pure propanediol) | 13.142 / * |
| | | Concanavalin A adsorbate | * | $3.77 \times 10^{-5}$ | $3.77 \times 10^{-5}$ / * |
| | 2D helicoid crystal | Bulk proline, glucose | 1.333 - 1.352, 1.333 - 1.360 ($10^{-6}$ resolution) | $10^{-6}$ - $10^{0}$, $5 \times 10^{-1}$ - $10^{0}$ | $10^{-4}$ - $10^{0}$ / $10^{-4}$, $5 \times 10^{-1}$ - $10^{0}$ / * |
| | | MicroRNA-21 | * | $5 \times 10^{-11}$ - $3 \times 10^{-9}$ | $5 \times 10^{-11}$ - $3 \times 10^{-9}$ / $1.14 \times 10^{-10}$ |
| | | sVAMP2 (SNARE protein complex) | * | $2 \times 10^{-7}$ | $2 \times 10^{-7}$ / * |

Table 4. 1 Sensor properties of various nanophotonic sensors[24,25,49,55,166,172,174–178].

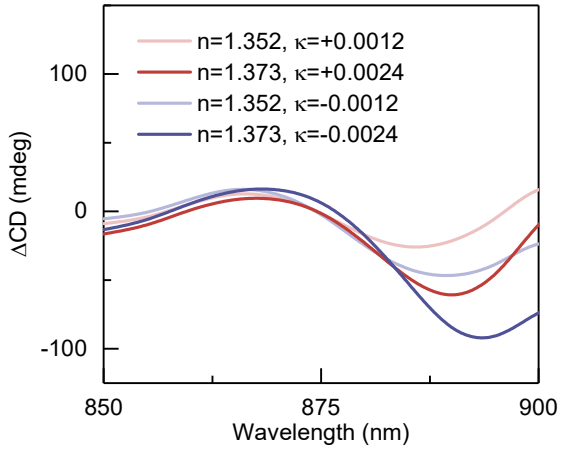


Figure 4. 16 Numerically calculated enantioselective collective CD (ΔCD) response of 2D helicoid crystal for various chirality parameters and refractive indices.

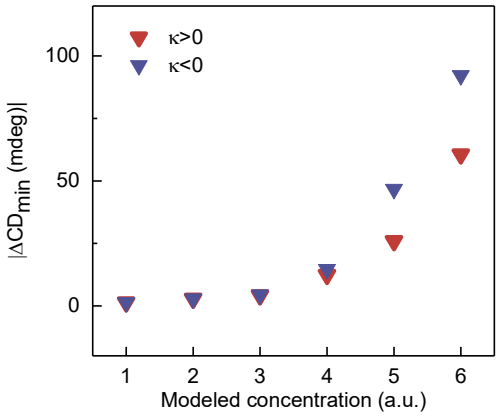


Figure 4. 17 Numerically calculated enantioselective collective CD ($|\Delta CD_{min}|$) response of 2D helicoid crystal for various chirality parameters and refractive indices. Modeled concentrations are as follows, ($n$, $\kappa$)= (1; 1.331, $\pm 1.2\times10^{-7}$), (2; 1.332, $\pm 1.2\times10^{-6}$), (3; 1.333, $\pm 1.2\times10^{-5}$), (4; 1.339, $\pm 1.2\times10^{-4}$), (5; 1.352, $\pm 1.2\times10^{-3}$), and (6; 1.373, $\pm 2.4\times10^{-3}$).

The results presented herein bear significant relevance, offering a meticulous validation of the potential of applying the distinctively high and uniform optical helicity density inherent to two-dimensional (2D) helicoid crystals. Such application is envisioned as a practical and efficacious chiral sensor, transforming the theoretical underpinnings into real-world applications. The implications of these findings are profound, suggesting a possibility that a chirality sensor underpinned using 2D helicoid crystals can move beyond the realms of large-scale molecular analysis, extending its utility to the assessment of chirality in minute samples that are vital for practical applications. The prospective applications encompass the analysis of the chirality of innovative drug molecules, Deoxyribonucleic Acid (DNA), proteins, and an array of other biologically relevant substances. Looking ahead to the subsequent chapter, the scope of investigation is set to broaden, moving beyond the confines of sensing molecular chirality. The investigative effort will involve conducting sensing experiments on a diverse spectrum of biomolecules. Moreover, the validation effort will include exploring whether the 2D helicoid crystals developed during this study can be utilized not only in the context of our customized setup but also incorporated into commercially available setups.

# Chapter 5. 2D Helicoid Crystal for Practical Chiral sensing

In the previous chapters, it has been robustly established that 2D helicoid crystals carry profound implications for the practical and real-world sensing of biomolecular chirality, even in scenarios where the volume of the analyte is extremely limited, reaching microscale dimensions. The ramifications of these findings are multi-fold, indicating that the utility of these 2D helicoid crystals isn't confined to the analysis of molecular chirality alone. Rather, these crystal structures might possess broader applications, demonstrating an adeptness in the sensing of chirality within a diverse array of biomolecules. These biomolecules not only inherently possess chirality, but their chirality can also dynamically vary as part of their biological mechanisms, presenting a wide-ranging landscape for potential chirality sensing applications. Furthermore, the research has underscored the uniquely advantageous properties of the 2D helicoid crystals. Their robust and uniformly distributed optical helicity density facilitates the analysis of chirality even in the context of trace amounts of molecules. This proves advantageous in applications where the detection of minute chirality variations is crucial. Another distinctive feature is the sensitivity of performance. Unlike conventional technologies that primarily rely on localized surface plasmon resonance (LSPR) and require direct attachment to plasmonic structures for sensing, the 2D helicoid crystals demonstrate a consistent and sensitive performance, regardless of the position of target analyte (See the positions in Figure 5. 1).

As the focus transitions to the following Chapter, the research intends to explore the application of 2D helicoid crystals in the context of DNA and protein molecules. Initial part of this Chapter involves attaching DNA and protein molecules to the 2D helicoid crystals, subsequently inducing their biological mechanisms to observe any associated changes in chirality. A key objective during this process will

be to investigate the potential applicability of collective circular dichroism (CD) as a tool to analyze the evolving chirality of DNA and proteins during these induced biological mechanisms. Moreover, in the concluding sections of this Chapter, the research aims to investigate if the 2D helicoid crystals can retain their characteristic properties and enantiosensitivity even when integrated into commercially available equipment, without necessitating the use of intricate and complex optical systems. This is an essential step towards understanding whether these crystals can function as a viable platform for tangible device applications.

By attempting to validate these ideas, the research hopes to demonstrate that the collective CD response of 2D helicoid crystals can sensitively detect the chirality of a wide variety of trace molecules. Furthermore, it also aims to show that this detection is possible within commercial equipment, requiring only straightforward processing steps. Through these investigations, the research expects to gain deeper insights into the real-world applications and potential commercialization of 2D helicoid crystals in the realm of chiral sensing.

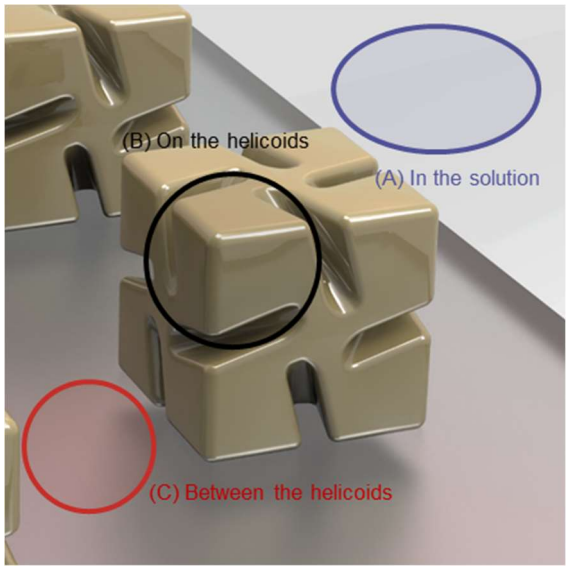


Figure 5. 1 Schematic illustration showing the capabilities of uniform and strong optical helicity for analyte position-independent sensing.

## 5.1 Sensing DNA-RNA hybridization by collective CD

To start the experiment, we aimed to probe the variation in chirality induced during the hybridization of a DNA strand that shared a complementary sequence with microRNA-21 (miRNA-21), a significant biomarker for lung cancer studies. This examination was designed to transpire atop the helicoid nanoparticles, integral to the 2D helicoid crystal, enclosed within a Polydimethylsiloxane (PDMS) matrix positioned over the nanoparticles (Position (B) in Figure 5. 1).

The methodology commenced with the immobilization of the thiolated DNA onto the helicoid, which was succeeded by the introduction of miRNA-21. MiRNA-21, being equipped with a sequence complementary to the affixed DNA, instigated the hybridization process (Figure 5. 2). During this transformation, we aimed to meticulously monitor the alterations in the collective CD signal radiating from the 2D helicoid crystal. The DNA and RNA entities used for the process, namely Thiolated ssDNA (5'-TCAACATCAGTCTGATAAGCTAAAAAAAAAAA/3DTPA/-3') and microRNA-21 (5'-rUAGCrUrUArUCAGACrUGArUGrUrUGA-3') were commercially procured from Integrated DNA Technologies (IDT). For the successful functionalization of the thiolated ssDNA onto the helicoid nanoparticles, we employed a low pH-assisted DNA functionalization technique[179], taking inspiration from the protocols delineated in previous literature. A thorough preparation of the 2D helicoid crystal was deemed necessary for the seamless functionalization of DNA, beginning with the surface cleaning of the helicoids using an ice-cold Sodium Borohydride ($NaBH_4$) solution. This process was performed under a temperature of 20 mM for a duration of 10 minutes. Following

the cleaning procedure, the crystal was washed with Deionized Water (DW) thrice and later bathed in a citrate·HCl buffer (10 mM) at 25 ℃ for 30 minutes. Subsequently, we ensured complete coverage of the 2D helicoid crystal with the DNA solution (5 μM, 15 μL) by injecting it into the analyte chamber (15 μL). The addition of the pH 3 sodium citrate buffer (500 mM, 0.63 μL) to the DNA solution instigated the functionalization reaction, which was allowed to proceed at a temperature of 25 ℃ for 30 minutes. An estimate of the DNA coverage on the 2D helicoid crystal, assessed to be roughly 1000 equivalents of DNA per nanoparticle, was obtained by comparing the UV-VIS response of the reacted and unreacted DNA solutions at a wavelength of 260 nm (Figure 5. 3). Following functionalization, the DNA-bound 2D helicoid crystal was washed with a flow of 10 mM Phosphate Buffered Saline (PBS) buffer (pH=7.4) for a span of 1 minute, aiming to eradicate any residual unreacted DNA strands within the analyte chamber. Post this cleaning process, miR-21 was hybridized to the DNA strands adhered to the 2D helicoid crystal. The miR-21 solution was created by diluting 100 μmol of RNA to the desired concentration using a 10 mM PBS buffer (pH=7.4). The actual process of hybridization entailed the rapid addition of a pre-heated RNA solution (60 ℃ for 30 minutes, 15 μL) to the analyte chamber, which was subsequently allowed to naturally cool down to 25 ℃, ensuring complete hybridization. Following the hybridization, another round of cleaning with a flow of 10 mM PBS buffer (pH=7.4) for 1 minute was performed to clear out unreacted RNA strands present in the chamber.

The changes induced by the hybridization were quantified by calculating the difference in CD signals ($\Delta CD=CD_{DNA+RNA}-CD_{DNA}$) before and after RNA binding, along with the absolute value of the minimum change ($|\Delta CD_{min}|$). As the concentration of miR-21 escalated, a corresponding increase in $|\Delta CD_{min}|$ was

observed (Figures 5.4 and 5.5). The detection limit was determined to be 146 pM, indicating a high-performance level compared to existing RNA sensors (Table 4.1)[180].

Through the in-depth results presented above, we have been successful in elucidating a robust method to sensitively capture the changes in chirality occurring during the intricate process of DNA and RNA hybridization using a 2D helicoid crystal. The significance of these findings cannot be overstated, as they represent a substantial step forward in our understanding of molecular chirality sensing. It has been observed that the sensing mechanism, which is anchored by the 2D helicoid crystal's unique attribute of high and consistent optical helicity density, is not merely limited to analysis of samples suspended in solution. Instead, its potential extends far beyond, providing the capability to scrutinize the chirality of molecules like DNA, which demonstrates a specific affinity for nanoparticle binding.

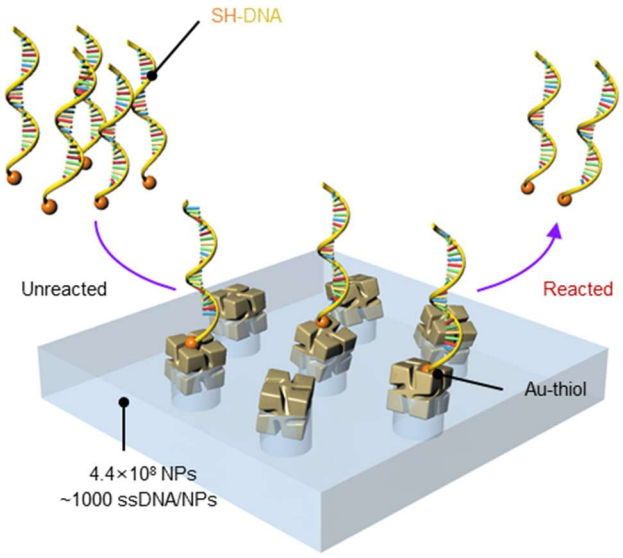


Figure 5. 2 Schematic illustration showing the process of attaching the thiolated DNA on the helicoids of 2D helicoid crystal.

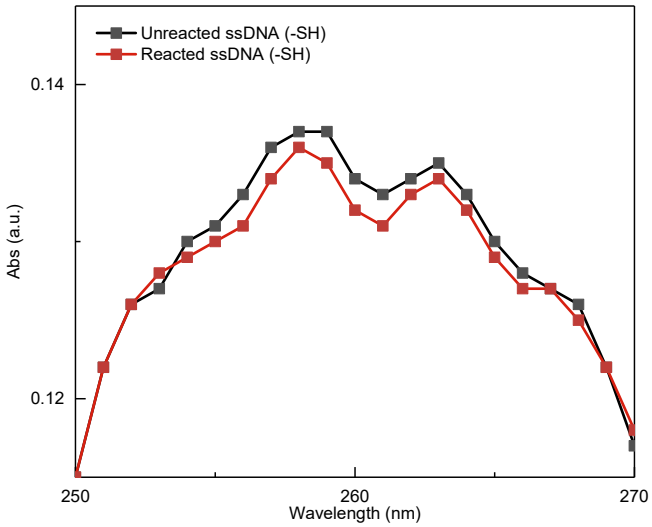


Figure 5. 3 UV-VIS spectra of thiolated DNA solution before and after the binding reaction on 2D helicoid crystal.

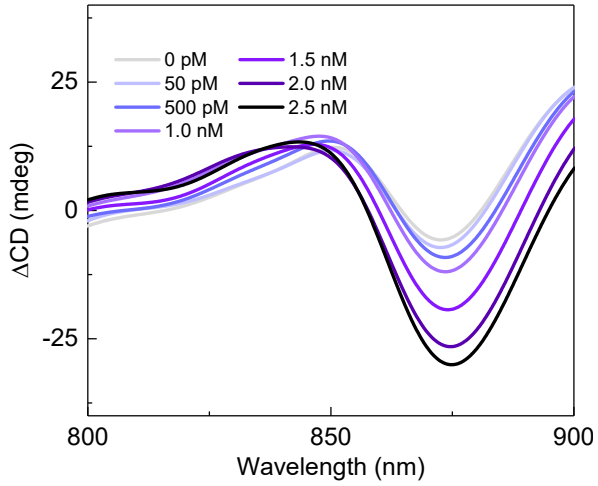


Figure 5. 4 ΔCD response of 2D helicoid crystal for various concentrations of miRNA-21 which hybridized on the 2D helicoid crystal.

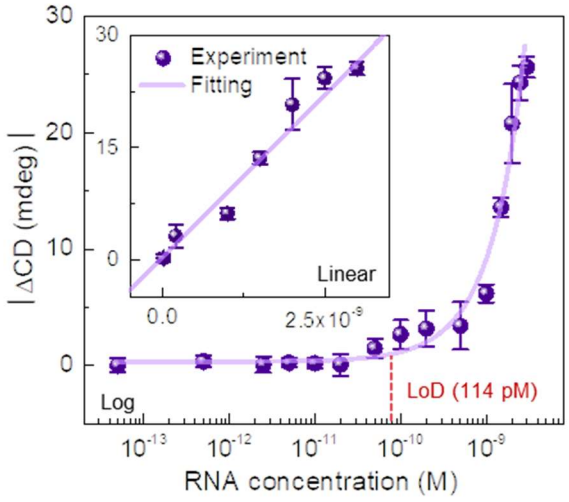


Figure 5. 5 $|\Delta CD_{min}|$ response of 2D helicoid crystal for concentration of miRNA-21 hybridized on the 2D helicoid crystal.

## 5.2 Sensing protein complex conformation change by collective CD

Next, in order to detect the chirality arising from the structural changes of proteins, researchers aimed to sense it through the PDMS section of the 2D helicoid crystal (Position (C) in Figure 5.1). We selected the SNARE complex[181–184], which forms a helical structure upon complex formation and is expressed in the process of neurotransmitter transmission in vivo, as the target substance.

Typically, the SNARE complex consists of an acceptor complex made up of syntaxin-1A without the N-terminal Habc domain (183-288), a synaptobrevin-2/VAMP2 fragment (49-96), and cysteine-free SNAP-25 isoform A, which are found in the bio-membrane within the body. It also includes the soluble part of VAMP2 lacking a transmembrane domain (1-96, A82C), distributed on the neurotransmitter-carrying vesicle (Figure 5. 6). The formation of a helical complex occurs through the binding of the acceptor complex and soluble VAMP2, thereby transmitting neurotransmitters into the membrane (Figure 5. 7).

For the purpose of experimentation, we first manufactured the SNARE proteins and the vesicles capable of carrying SNARE proteins in the following manner:

**Protein Preparation:**

All SNARE complexes were derived from rats and expressed in the Rosetta (DE3) pLysS strain. The acceptor complex consisted of a truncated syntaxin-1A without the N-terminal Habc domain (183-288), a synaptobrevin-2/VAMP2 fragment (49-96), and a cysteine-free SNAP-25 isoform A. The soluble part of

VAMP2 lacking a transmembrane domain (1-96, A82C) was cloned into pGEX-KG with an N-terminal GST-tag and a thrombin cleavage site. For expression of the acceptor complex, syntaxin-1A (183-288) and a VAMP2 fragment (49-96) without any affinity tags were cloned into pETDuet-1, and full-length SNAP-25A with an N-terminal 6His-tag was cloned into pET28a. These two plasmids were co-transformed into E. coli to assemble the acceptor complex. All proteins were grown in 1 L of standard LB medium at 37 °C until the OD600 reached approximately 0.7 and expressed for 3 hours post-0.5 mM IPTG induction. The cells were gathered via centrifugation and suspended in A buffer (50 mM pH 7.4 HEPES, 300 mM NaCl, 20 mM imidazole, 0.5 mM TCEP). For suspension cells expressing soluble VAMP2, 0.5% Tx100 and 1x protease inhibitor cocktail (genDEPOT) were added, and the same chemical and 0.5% sarcosine were added to cells expressing the acceptor complex. The suspended cells were lysed by sonication, and the cell lysate-expressing acceptor complex was nutated for 1 hour at 4 °C to solubilize the membrane proteins. After centrifugation (17,000×g, 30 minutes), the supernatant was loaded onto Ni-NTA agarose resin (QIAGEN) or glutathione-Sepharose 4B (GE healthcare) for 1 hour at 4 °C. In the case of the acceptor complex, the resin was sequentially washed with A buffer containing 0.1% Triton X-100 and A buffer containing 1 wt% OG, and the proteins were eluted with elution buffer (50 mM pH 8.0 Tris-HCl, 20 mM NaCl, 400 mM imidazole, 1 wt% OG, and 1 mM DTT). Thrombin was added for His-tag cleavage, and the elute was loaded onto a HiTrap Q (GE Healthcare) for anion exchange chromatography with a linearly increasing NaCl concentration of 20 mM to 1 M in 50 mM pH 8.0 Tris-HCl, 10% glycerol, and 1 mM DTT. The soluble part of VAMP2 in glutathione resin was washed with A buffer containing 0.1% Triton X-100 and eluted by thrombin cleavage for 1 hour at room temperature. The eluate was concentrated and loaded into a size exclusion chromatography (SEC) column (GE healthcare)

with SEC buffer (50 mM pH 7.4 HEPES, 150 mM NaCl, and 0.5 mM TCEP). Purified VAMP2 with cysteine mutation (A82C) was labeled with 10 times excess Cy3-maleimide (Lumiprobe) overnight at 4 °C (for VAMP2 labeled with Cy3). Unlabeled free dyes were separated on a PD MiniTrap G25 column (GE healthcare) with SEC buffer containing 10% glycerol. All purified proteins were confirmed by SDS-PAGE, and their concentration and labeling efficiency were measured with UV-VIS spectroscopy. Purified proteins whose purity and concentration were confirmed were stored at −80 °C until use.

**Vesicle reconstitution:**

All lipids utilized in the experiment were procured from Avanti. A lipid composition consisting of approximately 47 mol% 1-palmitoyl-2-oleoyl-glycero-3-phosphocholine (POPC), 25 mol% cholesterol, 12 mol% 1,2-dioleoyl-sn-glycero-3-phospho-L-serine (DOPS), 15 mol% 1,2-dioleoyl-sn-glycero-3-phosphoethanoleamine (DOPE), and 0.7 mol% 1,2-dioleoyl-sn-glycero-3-phosphoethanolamine-N-(cap biotinyl) (biotinyl CapDPPE) was assembled in a glass vial and subjected to vacuum drying overnight at 25 ℃. The solubilization of the dried lipids was initiated by introducing a solubilization buffer (50 mM pH 7.4 HEPES, 150 mM NaCl, and 3 wt% OG) to the vial, ensuring careful resuspension to preclude the formation of air bubbles. The lipid mixture was then sonicated for a minute in the vial to conclude the solubilization process. Subsequently, this mixture was moved to an e-tube and gently mixed using an Intelli-Mixer for a period of 30 minutes. Following solubilization, the lipid mixture was combined with the acceptor complex at a predetermined protein-to-lipid ratio of 1:1000. The solution was then diluted threefold using a buffer (50 mM pH 7.4 HEPES, 150 mM NaCl), effectively reducing the OG concentration below the critical micelle concentration (CMC). This diluted solution was transferred to a pre-equilibrated

Midi GeBaFlex tube (GeBa) with dialysis buffer (50 mM pH 7.4 HEPES and 150 mM NaCl) for more than 30 minutes at 4 ℃. Subsequently, SM2 Bio-Beads (Bio-Rad) were introduced into a beaker filled with the dialysis buffer. The tube was placed in a floating rack within the beaker and left to incubate overnight at 4 ℃, allowing the detergent to be removed from the mixture. After dialysis, the vesicle reconstitution process was considered complete.


Figure 5. 6 Proteins which constructs the SNARE complex.

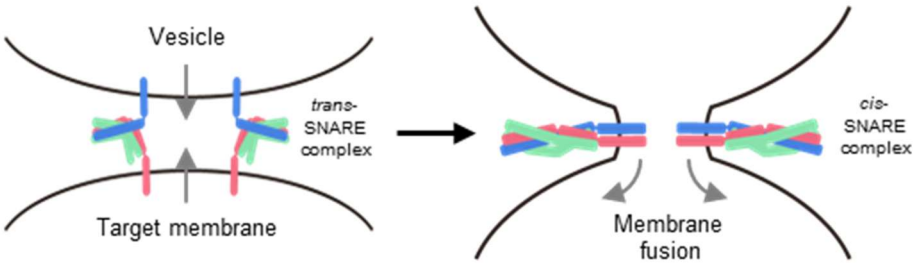


Figure 5. 7 Schematic illustration showing the membrane fusion process by constructing SNARE complex.

The protein previously prepared was utilized in carrying out an in vitro analysis of SNARE complex assembly with helicoids (Figure 5. 8). Given the two-dimensional extension of the optical helicity of the CR rather than it being localized, even minor disturbances in the 2D helicoid crystal could lead to a substantial renormalization of the resonance mode.

In order to commence the experiment, we manufactured 2D helicoid crystals and imparted functionality with BSA-biotin to hinder nonspecific binding. Subsequently, neutravidin (NTV) and biotinylated vesicles (Ves) were consecutively linked to the 2D helicoid crystals through specific molecular interactions. A PDMS substrate with nanopatterns was subjected to a solution of 20 μg/ml BSA-biotin in distilled water for a period of 12 hours at 25 ℃ in order to establish attachment of BSA-biotin to PDMS through hydrophobic interactions. The procedure was carried out inside a moisture-retaining chamber to prevent the solution from drying and evaporating. Once helicoids were implanted into the BSA-biotin-enhanced PDMS substrate, a 2D helicoid crystal was situated within the solution compartment (15 μL) and neutralized with reaction buffer (50 mM pH 7.4 HEPES, 150 mM NaCl, and 0.1% v/v Triton X-100) for a period of 10 minutes at 25 ℃ preceding the in vitro reconstitution analysis of SNARE complex assembly. In the process of NTV binding, NTV (0.1 mg/ml, 15 μL) from Thermo Fisher Scientific in the reaction buffer was directed onto the 2D helicoid crystal and subjected to incubation for 10 minutes at 25 ℃. Post NTV binding, the 2D helicoid crystal was thoroughly rinsed with buffer (50 mM pH 7.4 HEPES and 150 mM NaCl) three times in order to exclude unbound NTV from the substrate. During vesicle binding, vesicles (10 nM (100 μM [lipid conc.]), 15 μL), with and without the inclusion of the acceptor complex (*trans*-form), were guided onto the 2D helicoid crystal and subjected to incubation for 10 minutes at 25 ℃, which was

then followed by a rinsing phase. Post vesicle binding, soluble VAMP2 (200 nM, 15 μL) in buffer (50 mM pH 7.4 HEPES and 150 mM NaCl) with 1 wt% BSA to deter nonspecific binding was infused into the chamber and subjected to incubation for 10 minutes at 25 ℃. The rinsing phase was repeated after sVAMP2 infusion. The addition of sVAMP2 leads to the substitution of the C-terminal VAMP2 in the acceptor complex and the formation of a complete four-helix bundle, symbolic of the structure of the SNARE complex (*cis*-form). The validation of SNARE complex formation upon the addition of VAMP2 was conducted through a fluorescence test employing soluble VAMP2 marked with Cy3 in place of the unlabeled form (Figure 5. 9, 10, and 11). The surface coverage of SNARE complexes on 2D helicoid crystal was calculated to be 1 complex/$10^3$ $nm^2$ (i.e., monolayer). After completion of the in vitro analysis of SNARE complex assembly, the 2D helicoid crystal was removed from the solution compartment, placed on a coverslip (VWR), and immobilized using 5 Minute® Epoxy (Devcon). After securing the position, the coverslip was affixed onto the sample stage of a custom objective-style microscope.

Spectral data for the 2D helicoid crystal was procured for each step of the reaction in 50 mM HEPES buffer (pH 7.4, 150 mM NaCl). The addition of NTV and Ves shifted the $\Delta CD_{proteins} \equiv CD_{after\ conjugation} - CD_{initial}$ of the 2D helicoid crystal irrespective of the presence of acceptor complexes. However, the addition of sVAMP2 could only escalate the ΔCD of the 2D helicoid crystal with acceptor complexes (Figure 5.12 and 13).

Alterations in SNARE complex conformations was captured with high selectivity and sensitivity. Specifically, the structural transition of SNARE complexes from trans- to cis-form was sequentially emulated by stepwise addition of Ves-integrated acceptor complexes and sVAMP2 to the biotin-NTV system.

Significantly, Ves, which is similar to cellular membranes, was efficiently constructed on 2D helicoid crystals. Moreover, this combination, in concert with sequential reproduction, successfully emulated the Ves-membrane fusion process. In contrast to traditional methodologies such as fluorescence resonance energy transfer (FRET), our sensor can operate unlabeled. This finding indicates that our platform can be deployed to monitor time-dependent structural alterations of biomolecules that occur even in a localized region, such as on membranes.

This groundbreaking revelation paves the way for the application of 2D helicoid crystals in broad-ranging scenarios, including those demanding a deeper understanding of the chirality dynamics in complex molecular structures and interactions. Furthermore, the versatility of this sensing mechanism, as demonstrated by its capacity to accommodate different types of analytes, adds a substantial layer of utility and applicability, thereby raising the bar for future advancements in the field of chiral sensing. It should be highlighted that these insights have potentially transformative implications for the development of novel chirality sensing platforms, offering a platform that promises a significantly improved sensitivity and applicability spectrum. This, coupled with the 2D helicoid crystal's potential to identify and analyse chiral phenomena even in molecules demonstrating specific binding affinities to nanoparticles, could potentially lead to breakthroughs in various scientific and technological domains that rely on molecular chirality analysis.

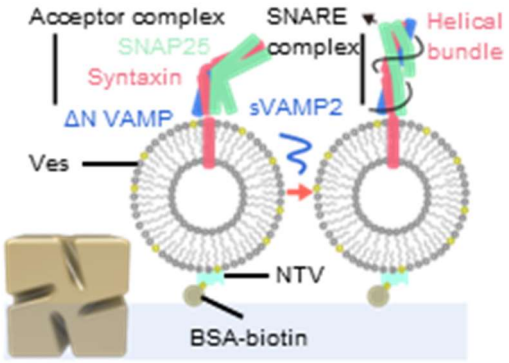


Figure 5. 8 Schematic illustration showing the SNARE complexation on the 2D helicoid crystal.

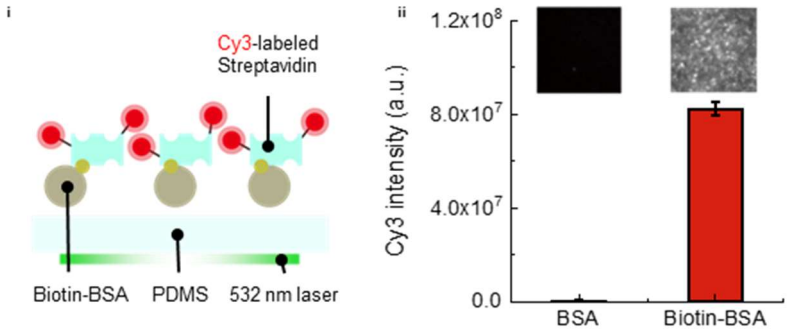


Figure 5. 9 Schematic illustration showing the fluorescence-based confirmation of BSA binding on the 2D helicoid crystal (i) and corresponding fluorescence data (ii).

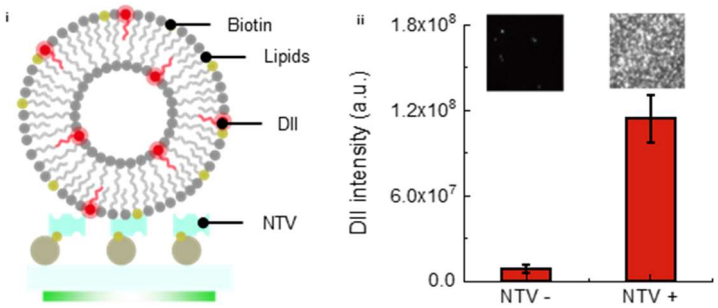


Figure 5. 10 Schematic illustration showing the fluorescence based confirmation of Vesicle binding on the 2D helicoid crystal (i) and corresponding fluorescence data (ii).

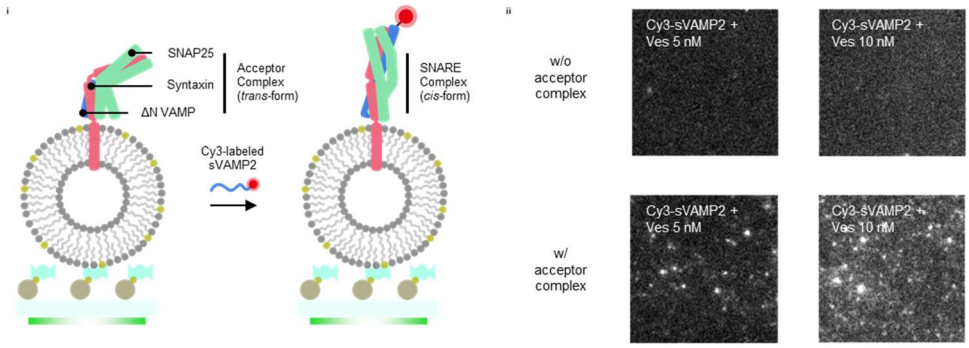


Figure 5. 11 Schematic illustration showing the fluorescence-based confirmation of SNARE complex formation on the 2D helicoid crystal (i) and corresponding fluorescence data (ii).

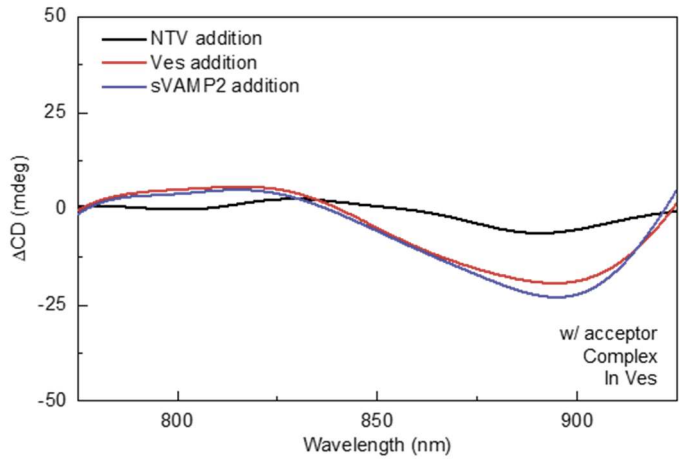


Figure 5. 12 $\Delta CD_{proteins} \equiv CD_{after\ conjugation} - CD_{initial}$ response of 2D helicoid crystal for each step of SNARE complex formation on 2D helicoid crystal with acceptor complexes.

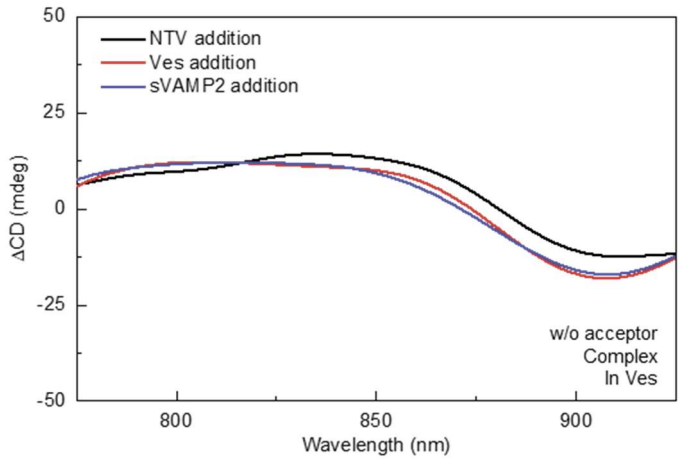


Figure 5. 13 $\Delta CD_{proteins} \equiv CD_{after\ conjugation} - CD_{initial}$ response of 2D helicoid crystal for each step of SNARE complex formation on 2D helicoid crystal without acceptor complexes.

## 5.3 Integration of 2D helicoid crystal in SPR sensing system

In this Chapter, our primary objective was to authenticate the generic adaptability of 2D helicoid crystals. More specifically, our ambition was to scrutinize whether the enantioselective response, a prominent characteristic that we had previously demonstrated with these crystals, is operational not solely in specially designed optical measurement systems, but also in traditional commercially available optical frameworks. We envisioned that such a capability would unequivocally underline their potential as a sensor platform. Therefore, we carried out an experimental approach where we integrated the 2D helicoid crystals into a Surface Plasmon Resonance (SPR) sensing apparatus, to observe and evaluate their enantioselective response.

An intriguing phenomenon that we observed was that the enantioselective CD, a signature feature of our 2D helicoid crystals, was also profoundly visible in the reflection mode. This was a significant observation since it indicated that any changes or deviations in this feature could be precisely detected under Total Internal Reflection (TIR) conditions. As part of our experimental protocol, we incorporated a 2D helicoid crystal into a Circularly Polarized Light (CPL)-based SPR sensing system and were able to observe enantioselective optical responses of the collective CD under these TIR conditions, a feature we've denoted as $CD_R$. Specifically, we utilized a custom-designed reflection-CD apparatus that could gauge the circular dichroism of light reflected off the test samples. We assembled an optical table with several components: a tungsten halogen lamp that served as the light source, a mirror to direct the light, a collimating lens for beam shaping, a linear polarizer to generate plane-polarized light, a quarter-wave plate from

Thorlabs to alter the polarization state of light, and an objective lens to focus the beam down to a spot size of 200 μm (Figure 5. 14).

For our experiment, we mounted the 2D helicoid crystal - that was prepared onto a quartz substrate, which was subsequently positioned on a hemicylindrical prism. This prism was placed on a motorized rotation stage from Thorlabs that allowed us to precisely control the angle of incidence of the light. Utilizing a spectrophotometer, specifically the Flame spectrometer from Ocean Optics, we were able to measure the reflectivity of the sample (averaged over 10 acquisitions) for Left Circularly Polarized (LCP) and Right Circularly Polarized (RCP) light. This reflectivity data served as a basis for calculating the reflection circular dichroism by subtracting the reflectivity for RCP light from the reflectivity for LCP light. Our data acquisition strategy involved repeated measurements, conducted four times for each experiment, which ensured consistency in the obtained reflection CD spectra.

Our experiments revealed that the reflection-based setup is not just a viable, but also an effective method for generating a CR mode and collective CD that respond enantioselectively (Figure 5. 15 and 16). We also confirmed the formation of such modes by comparing the reflection CD data from drop-coated (*i.e.*, randomly distributed helicoids). This was a remarkable finding as it underscored the versatility of our 2D helicoid crystal system. Furthermore, we were able to quantify the variations in the collective CD that were induced by different chirality prolines, L- and D-proline. For this, we extracted the difference in reflection CD, denoted $\Delta CD_R$, and calculated the absolute value of $\Delta CD_R$ at the minima ($|\Delta CD_{R,min}|$). Our observations indicated a higher sensitivity to D-proline compared to L-proline, which was in agreement with theoretical predictions and previous

transmission-based measurements. The measured changes in the reflection CD ($|\Delta CD_{R,\,min}|$) exhibited a gradual increase over a wide concentration range from 10-6 M to 100 M, specifically from 0 mdeg to 69 mdeg for L-proline and up to 76 mdeg for D-proline (Figure 5. 17). We compiled and compared the sensing performance of our technique with that of other prevalent methods, emphasizing the distinct advantages of our approach (Table 4. 1 and Figure 5. 18).

In conclusion, the successful integration of the 2D helicoid crystals into the commercially available SPR sensing system and the consequent observations of an enantioselective optical response underline the potential of these uniquely structured crystals as a versatile sensor platform. The ability of the 2D helicoid crystal to demonstrate enantioselective responses in both specially designed and traditional optical systems indicates its potential for diverse applications. Furthermore, the sensitivity to changes in chiral molecules, as exemplified by the L- and D-proline, and the ability to precisely monitor these changes under total internal reflection conditions, provide strong evidence for the robustness and sensitivity of this sensing approach. The distinct advantages, including its label-free nature, versatility, and high sensitivity, when compared with other prevalent methods, make the 2D helicoid crystal a promising candidate for chiral sensing applications. The results from this work open up a new path for the application of 2D helicoid crystals and similar structures in the field of chiral molecule detection, and potentially broaden the horizon of biomolecular sensing, by offering a promising platform that could be effectively customized for diverse sensing applications.

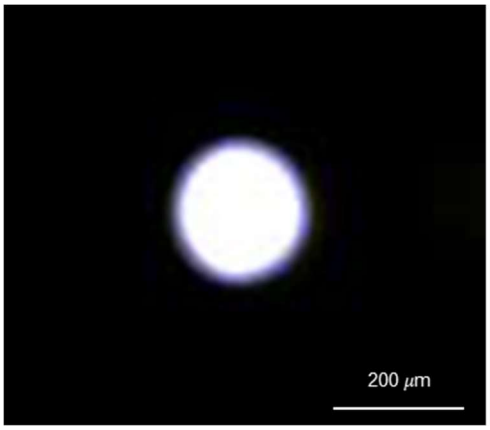


Figure 5. 14 Photograph of light source at the sample position.

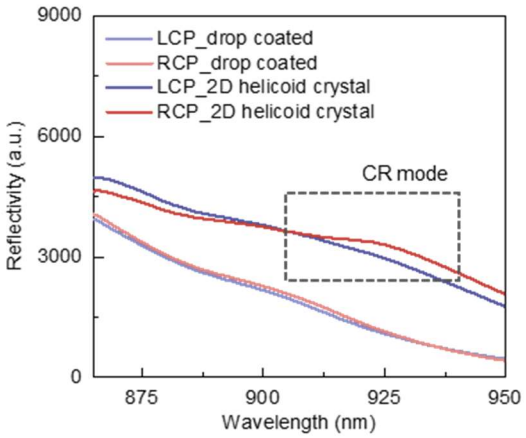


Figure 5. 15 Reflectance spectra for 2D helicoid crystal and drop coated helicoids for LCP and RCP illuminations.

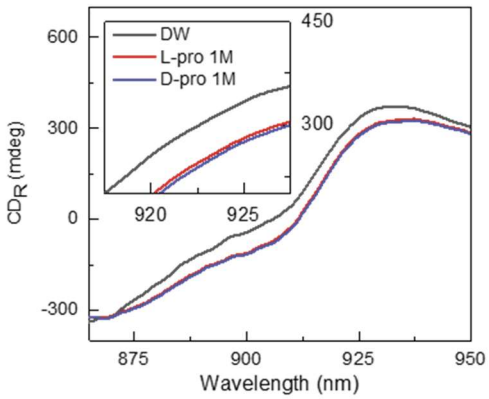


Figure 5. 16 $CD_R$ spectra for 2D helicoid crystal for DI, 1M L-, and D-proline solutions.

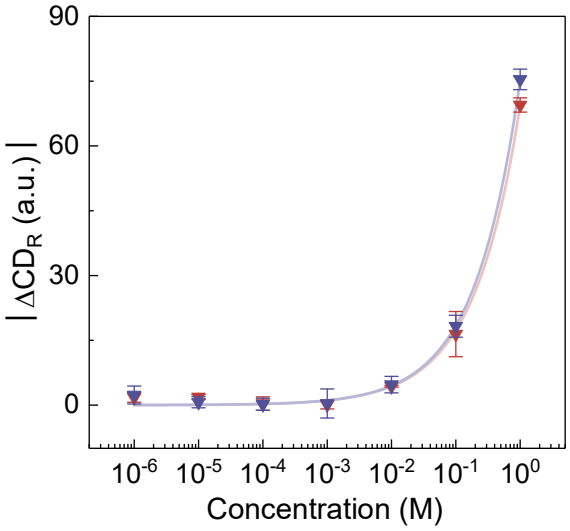


Figure 5. 17 $|\Delta CD_{R,\ min}|$ graphs for various concentrations of L- and D-proline solutions.

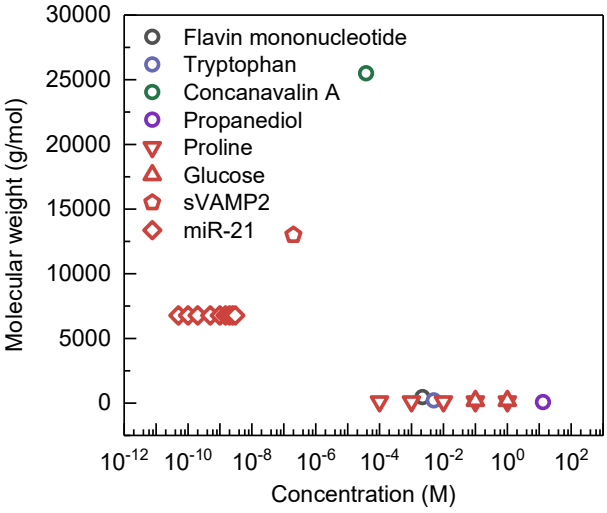


Figure 5. 18 Performance chart describing the enantioselective sensitivity of currently reported chiral sensors for various types of bio-molecular analyte.

# Chapter 6. Concluding Remarks

In this thesis, we embarked on a journey to create an advanced platform for ultra-sensitive chiral sensing, relying on the power of chiral plasmonic nanostructures known for their robust and uniform optical helicity density. This complex task spanned the realms of fabricating and optically characterizing two-dimensional (2D) aligned chiral plasmonic nanoparticles, unraveling the theoretical constructs for their precise deployment in chiral sensing, and progressing towards creating functional chiral sensor platforms. As a part of this, first, we engineered a system of two-dimensional (2D) aligned helicoid nanoparticles. We thoroughly studied the collective resonance and resulting collective CD generated from this structure. Our investigation examined the interdependencies among the size of the nanoparticles, the angle of the incident light, and the periodicity of the structures. Secondly, we applied the fabricated 2D helicoid crystal for chiral sensing. To do this effectively, we had to gain a comprehensive understanding of the physical properties of these structures and develop a chiral perturbation theory. This theory allowed us to elucidate the mechanisms of chiral sensing. Lastly, we empirically demonstrated the applicability of the 2D helicoid crystal as a chiral sensor by conducting chirality sensing experiments on various molecules, including amino acids, DNA, and proteins. Through techniques like micro-volume and colorimetric chirality detection, we were able to showcase the practicality of our system. Furthermore, we demonstrated the universality of the 2D helicoid crystal. Our theoretical mechanisms and experimental realizations can be integrated not only into custom optic systems but also into commercialized platforms. This finding underscores the broad applicability and versatility of the 2D helicoid crystal.

The conventional chiral plasmonic structure, which is based on the local surface plasmon resonance (LSPR) for chiral sensing, has primarily focused on amplifying the CD of the molecules themselves through the local enhancement of optical helicity density, which describes how helical and strong the incident light is in the space where the molecules exist. While these methods have succeeded in amplifying the CD signal of high-concentration samples on the plasmonic structures, most of the techniques could not be used as a platform for practical chiral sensing applications due to the impact of the molecule's location, orientation, etc., owing to the local characteristics of the LSPR. In this thesis, we fabricated a chiral plasmonic nanostructure that can induce a broader and stronger optical helicity density characteristic, and demonstrated a practical, versatile chirality sensor based on this structure.

Firstly, we aimed to induce a collective resonance phenomenon, which can concentrate the energy of incident light strongly and uniformly on a 2D plane, in a 3D structure that has the most isotropic chirality, the 432 helicoid III. For the fabrication of a 2D helicoid crystal with a regular assembly structure, we manufactured a PDMS substrate with a regular nano-well structure through PDMS patterning. We developed a methodology to assemble helicoids into the nano-well structure through assembly, thereby fabricating a 2D helicoid crystal. We found that the collective resonance mode occurs through the hybridization of the LSPR of the nanoparticles constituting the 2D helicoid crystal and the diffraction mode due to the regular structure, and aimed to produce a 2D helicoid crystal that can exhibit the largest chiroptic response in this structure. For this purpose, we used a helicoid with a size of 180 nm, fixed the angle of the incident light at 60 degrees, and set the periodicity of the assembled helicoid nanoparticles to 400 nm. The fabricated 2D helicoid crystal showed a strong chiroptic response of about 4000 mdeg, and it was confirmed that the CD signal generated by the collective resonance showed an

amplified chiroptic response from 0 to 3000 mdeg. Through this, we were able to produce a 2D helicoid crystal with a strong collective CD signal based on the collective resonance phenomenon and understand its optical properties.

Furthermore, we conducted research to physically understand the strong chiroptic response of the 2D helicoid crystal based on electromagnetic simulation. As a result, we found that a collective mode, where the TE/TM mode overlaps, thus strongly interacting with the circularly polarized light, is generated when a circularly polarized light tilted at 60 degrees is irradiated on the 2D helicoid crystal, and we were able to physically explain the strong chiroptic response of the 2D helicoid crystal. Also, to apply the actual fabricated 2D helicoid crystal for chiral sensing applications, we first physically grasped the optical helicity density of the 2D helicoid crystal. For this purpose, we conducted a phase analysis of the formed TE/TM mode to understand how helical and strong the formed mode is in the 2D helicoid crystal and confirmed that an electromagnetic field mode rotating like a circularly polarized light is formed in the 2D helicoid crystal when the formed TE/TM mode has a phase difference of half a pi. As a result, we found that a strong optical helicity density could be induced in the 2D helicoid crystal and aimed to apply it to chirality sensing.

To apply the strong optical helicity density of the 2D helicoid crystal to practical chiral sensing in a substantive manner, we developed a Chiral Perturbation Theory. This theory, similar to traditional molecular CD augmentation theories, posits that structures with high optical helicity density are advantageous for chiral sensing. However, it differs from traditional theories by focusing on the back-action of the molecule's chirality on the energy of the chiral plasmonic nanostructure, rather than amplifying the CD of the molecule itself. This robust theory can explain the spectral resonance difference between the molecule and the plasmonic material,

which has been a chronic issue in traditional molecular CD amplification. It also implies that a sensor with a strong and uniform optical helicity density, such as a 2D helicoid crystal, can demonstrate strong enantiosensitivity and consistent performance regardless of the molecule's position or orientation. We did not stop at this theoretical discovery. We carried out experimental applications of chiral sensing using the 2D helicoid crystal. According to the Chiral Perturbation Theory, we detected different degrees of shift in the collective CD variation due to the chirality of 1.5 mL of chiral molecules. This resulted in CD changes that were more sensitive to D-molecules than L-molecules, indicating that the chirality of molecules dispersed in a solution can be differentiated using a 2D helicoid crystal. Furthermore, we developed a platform capable of predicting the ratio and total concentration of chiral molecules in a solution by identifying anomalies in the slope changes of the collective CD variation.

Additionally, we linked the sensitive chiral response of the 2D helicoid crystal in collective CD to the unique characteristic of chiral plasmonic structures, which is the distribution of polarized colors. We then demonstrated a platform that can distinguish the chirality of molecules with the naked eye by tracing back the color change of the polarized light in the 2D helicoid crystal caused by the chiral molecules. This provides proof of the practical chiral sensing applicability of the 2D helicoid crystal.

For real-world applications of molecular chirality sensing with the 2D helicoid crystal, we conducted chiral sensing experiments on minuscule amounts of molecules, such as DNA and protein. By introducing a micro-volume chamber into the 2D helicoid crystal, we were able to sensitively detect the chirality of molecules with only 15 uL of sample, achieving sensitivity down to the few-mM range. We also verified the location-independent sensing capability of the 2D helicoid crystal,

thanks to its strong and uniform optical helicity density in 2D. Specifically, we detected the chirality changes that occur when the structure of miRNA-21 attached to the helicoid and SNARE protein complex attached to PDMS changes in real time, through the collective CD response changes of the 2D helicoid crystal.

Finally, through the introduction of an SPR sensor system into the 2D helicoid crystal, we demonstrated that chiral sensing based on collective CD is possible even without a specially constructed optical measurement method used in this thesis, thus proving the versatile applicability of the 2D helicoid crystal as a platform. By simply adjusting the linearly polarized light source of the existing SPR system to circularly polarized light to induce CD signals, we could clearly confirm the enantioselective response of their collective CD signals in this system.

From this study, we conclude that the novel nanophotonic approach utilizing the collective CD of 2D helicoid crystals holds substantial promise in revolutionizing enantioselective sensing. Central to our approach is the idea of uniformly amplifying chiral light-matter interactions across a 2D plane through the collective activation of a rotating electric dipole, leading to the generation of collective CD. This introduces two important enhancements to nanophotonic chiral sensing. The first is the remarkable robustness against molecular randomness, demonstrated by consistently high sensitivity even in liquid samples. The second is the occurrence of reverse spectral shift of the resonance contingent on molecular handedness. Looking ahead, this methodology opens doors for transformative applications of chiral sensing, such as real-time surveillance of conformational transitions at the molecular scale. Given the compatibility of our approach with other optical sensing systems like SPR, it paves the way for large-scale, rapid implementation of chiral sensing, thereby offering a significant contribution to this field of research. The principles of collective CD, as explored in our study, hence stand at the forefront of future advancements in enantioselective sensing. For more

practical application of the 2D helicoid crystal in the aspect of commercialization, the optimization of fabrication process such as, improvement in nanopatterning and helicoid assembly should be accompanied. Also, the selection of specific target which can draw attention from real-industry. By doing so, we expect that we can expand the realm of our principles of 2D helicoid crystal which delineated in this thesis into the real-industrial application.

# References


(1) Inaki, M.; Liu, J.; Matsuno, K. Cell Chirality: Its Origin and Roles in Left–Right Asymmetric Development. *Philosophical Transactions of the Royal Society B: Biological Sciences* **2016**, *371* (1710), 20150403. https://doi.org/10.1098/rstb.2015.0403.

(2) Tee, Y. H.; Shemesh, T.; Thiagarajan, V.; Hariadi, R. F.; Anderson, K. L.; Page, C.; Volkmann, N.; Hanein, D.; Sivaramakrishnan, S.; Kozlov, M. M.; Bershadsky, A. D. Cellular Chirality Arising from the Self-Organization of the Actin Cytoskeleton. *Nat Cell Biol* **2015**, *17* (4), 445–457. https://doi.org/10.1038/ncb3137.

(3) Kean, W. F.; Howard-Lock, H. E.; Lock, C. J. L. Chirality in Antirheumatic Drugs. *The Lancet* **1991**, *338* (8782–8783), 1565–1568. https://doi.org/10.1016/0140-6736(91)92382-C.

(4) Nguyen, L. A.; He, H.; Pham-Huy, C. Chiral Drugs: An Overview. *Int J Biomed Sci* **2006**, *2* (2), 85–100. https://doi.org/https://www.ncbi.nlm.nih.gov/pmc/articles/PMC3614593/.

(5) Cody, A. M.; Cody, R. D. Chiral Habit Modifications of Gypsum from Epitaxial-like Adsorption of Stereospecific Growth Inhibitors. *J Cryst Growth* **1991**, *113* (3–4), 508–519. https://doi.org/10.1016/0022-0248(91)90086-K.

(6) Raval, R. Chiral Expression from Molecular Assemblies at Metal Surfaces: Insights from Surface Science Techniques. *Chem Soc Rev* **2009**, *38* (3), 707. https://doi.org/10.1039/b800411k.

(7) Barron, L. D. *Molecular Light Scattering and Optical Activity*; Cambridge University Press, 2004. https://doi.org/10.1017/CBO9780511535468.

(8) Tang, Y.; Cohen, A. E. Optical Chirality and Its Interaction with Matter. *Phys Rev Lett* **2010**, *104* (16), 163901. https://doi.org/10.1103/PhysRevLett.104.163901.

(9) Glazer, A. M.; Stadnicka, K. On the Origin of Optical Activity in Crystal Structures. *J Appl Crystallogr* **1986**, *19* (2), 108–122. https://doi.org/10.1107/S0021889886089823.

(10) Rhee, H.; Choi, J. S.; Starling, D. J.; Howell, J. C.; Cho, M. Amplifications in Chiroptical Spectroscopy, Optical Enantioselectivity, and Weak Value Measurement. *Chem Sci* **2013**, *4* (11), 4107–4114. https://doi.org/10.1039/c3sc51255j.

(11) Eom, I.; Ahn, S.-H.; Rhee, H.; Cho, M. Broadband near UV to Visible Optical Activity Measurement Using Self-Heterodyned Method. *Opt Express* **2011**, *19* (10), 10017. https://doi.org/10.1364/oe.19.010017.

(12) Bassiri, S.; Papas, C. H.; Engheta, N. Electromagnetic Wave Propagation through a Dielectric–Chiral Interface and through a Chiral Slab: Errata. *Journal of the Optical Society of America A* **1990**, *7* (11), 2154. https://doi.org/10.1364/JOSAA.7.002154.

(13) Fasman, G. D. *Circular Dichroism and the Conformational Analysis of Biomolecules*; Fasman, G. D., Ed.; Springer US: Boston, MA, 1996. https://doi.org/10.1007/978-1-4757-2508-7.

(14) Greenfield, N. J. Using Circular Dichroism Spectra to Estimate

Protein Secondary Structure. *Nat Protoc* **2006**, *1* (6), 2876–2890. https://doi.org/10.1038/nprot.2006.202.

(15) Ranjbar, B.; Gill, P. Circular Dichroism Techniques: Biomolecular and Nanostructural Analyses- A Review. *Chem Biol Drug Des* **2009**, *74* (2), 101–120. https://doi.org/10.1111/j.1747-0285.2009.00847.x.

(16) Prabodh, A.; Wang, Y.; Sinn, S.; Albertini, P.; Spies, C.; Spuling, E.; Yang, L. P.; Jiang, W.; Bräse, S.; Biedermann, F. Fluorescence Detected Circular Dichroism (FDCD) for Supramolecular Host-Guest Complexes. *Chem Sci* **2021**, *12* (27), 9420–9431. https://doi.org/10.1039/d1sc01411k.

(17) Funk, T.; Deb, A.; George, S. J.; Wang, H.; Cramer, S. P. X-Ray Magnetic Circular Dichroism - A High Energy Probe of Magnetic Properties. *Coordination Chemistry Reviews*. 2005, pp 3–30. https://doi.org/10.1016/j.ccr.2004.05.017.

(18) Parchaňský, V.; Kapitán, J.; Bouř, P. Inspecting Chiral Molecules by Raman Optical Activity Spectroscopy. *RSC Adv* **2014**, *4* (100), 57125–57136. https://doi.org/10.1039/c4ra10416a.

(19) Rhee, H.; June, Y. G.; Lee, J. S.; Lee, K. K.; Ha, J. H.; Kim, Z. H.; Jeon, S. J.; Cho, M. Femtosecond Characterization of Vibrational Optical Activity of Chiral Molecules. *Nature* **2009**, *458* (7236), 310–313. https://doi.org/10.1038/nature07846.

(20) Bonner, W. A.; Kavasmaneck, P. R.; Martin, F. S.; Flores, J. J. Asymmetric Adsorption by Quartz: A Model for the Prebiotic Origin of Optical Activity. *Orig Life* **1975**, *6* (3), 367–376.

https://doi.org/10.1007/BF01130338.

(21) Hentschel, M.; Schäferling, M.; Duan, X.; Giessen, H.; Liu, N. Chiral Plasmonics. *Sci Adv* **2017**, *3* (5), e1602735. https://doi.org/10.1126/sciadv.1602735.

(22) Okamoto, H. Local Optical Activity of Nano-to Microscale Materials and Plasmons. *Journal of Materials Chemistry C*. Royal Society of Chemistry 2019, pp 14771–14787. https://doi.org/10.1039/c9tc05141d.

(23) Schäferling, M.; Dregely, D.; Hentschel, M.; Giessen, H. Tailoring Enhanced Optical Chirality: Design Principles for Chiral Plasmonic Nanostructures. *Phys Rev X* **2012**, *2* (3), 031010. https://doi.org/10.1103/PhysRevX.2.031010.

(24) Zhao, Y.; Askarpour, A. N.; Sun, L.; Shi, J.; Li, X.; Alù, A. Chirality Detection of Enantiomers Using Twisted Optical Metamaterials. *Nat Commun* **2017**, *8*, 6–13. https://doi.org/10.1038/ncomms14180.

(25) Abdulrahman, N. A.; Fan, Z.; Tonooka, T.; Kelly, S. M.; Gadegaard, N.; Hendry, E.; Govorov, A. O.; Kadodwala, M. Induced Chirality through Electromagnetic Coupling between Chiral Molecular Layers and Plasmonic Nanostructures. *Nano Lett* **2012**, *12* (2), 977–983. https://doi.org/10.1021/nl204055r.

(26) Rodrigues, S. P.; Cui, Y.; Lan, S.; Kang, L.; Cai, W. Metamaterials Enable Chiral-Selective Enhancement of Two-Photon Luminescence from Quantum Emitters. *Advanced Materials* **2015**, *27* (6), 1124–1130. https://doi.org/10.1002/adma.201405072.

(27) Lu, F.; Tian, Y.; Liu, M.; Su, D.; Zhang, H.; Govorov, A. O.; Gang, O. Discrete Nanocubes as Plasmonic Reporters of Molecular Chirality. *Nano Lett* **2013**, *13* (7), 3145–3151. https://doi.org/10.1021/nl401107g.

(28) Wu, X.; Xu, L.; Liu, L.; Ma, W.; Yin, H.; Kuang, H.; Wang, L.; Xu, C.; Kotov, N. A. Unexpected Chirality of Nanoparticle Dimers and Ultrasensitive Chiroplasmonic Bioanalysis. *J Am Chem Soc* **2013**, *135* (49), 18629–18636. https://doi.org/10.1021/ja4095445.

(29) Funck, T.; Nicoli, F.; Kuzyk, A.; Liedl, T. Sensing Picomolar Concentrations of RNA Using Switchable Plasmonic Chirality. *Angewandte Chemie - International Edition* **2018**, *57* (41), 13495–13498. https://doi.org/10.1002/anie.201807029.

(30) Liu, M.; Powell, D. A.; Guo, R.; Shadrivov, I. V.; Kivshar, Y. S. Polarization-Induced Chirality in Metamaterials via Optomechanical Interaction. *Adv Opt Mater* **2017**, *5* (16), 1600760. https://doi.org/10.1002/adom.201600760.

(31) Valev, V. K.; Baumberg, J. J.; Sibilia, C.; Verbiest, T. Chirality and Chiroptical Effects in Plasmonic Nanostructures: Fundamentals, Recent Progress, and Outlook. *Advanced Materials* **2013**, *25* (18), 2517–2534. https://doi.org/10.1002/adma.201205178.

(32) McPeak, K. M.; van Engers, C. D.; Bianchi, S.; Rossinelli, A.; Poulikakos, L. V.; Bernard, L.; Herrmann, S.; Kim, D. K.; Burger, S.; Blome, M.; Jayanti, S. V.; Norris, D. J. Ultraviolet Plasmonic Chirality from Colloidal Aluminum Nanoparticles Exhibiting Charge-Selective Protein Detection. *Advanced Materials* **2015**, *27* (40),

6244–6250. https://doi.org/10.1002/adma.201503493.

(33) Mohammadi, E.; Tsakmakidis, K. L.; Askarpour, A. N.; Dehkhoda, P.; Tavakoli, A.; Altug, H. Nanophotonic Platforms for Enhanced Chiral Sensing. *ACS Photonics* **2018**, *5* (7), 2669–2675. https://doi.org/10.1021/acsphotonics.8b00270.

(34) Yoo, S.; Park, Q. H. Chiral Light-Matter Interaction in Optical Resonators. *Phys Rev Lett* **2015**, *114* (20), 1–5. https://doi.org/10.1103/PhysRevLett.114.203003.

(35) Fan, Z.; Govorov, A. O. Plasmonic Circular Dichroism of Chiral Metal Nanoparticle Assemblies. *Nano Lett* **2010**, *10* (7), 2580–2587. https://doi.org/10.1021/nl101231b.

(36) Kelly, C.; Tullius, R.; Lapthorn, A. J.; Gadegaard, N.; Cooke, G.; Barron, L. D.; Karimullah, A. S.; Rotello, V. M.; Kadodwala, M. Chiral Plasmonic Fields Probe Structural Order of Biointerfaces. *J Am Chem Soc* **2018**, *140* (27), 8509–8517. https://doi.org/10.1021/jacs.8b03634.

(37) Yang, L.; Kwan, C.; Zhang, L.; Li, X.; Han, Y.; Leung, K. C.; Yang, Y.; Huang, Z. Chiral Nanoparticle-Induced Enantioselective Amplification of Molecular Optical Activity. *Adv Funct Mater* **2018**, *29* (8), 1807307. https://doi.org/10.1002/adfm.201807307.

(38) Tang, Y.; Cohen, A. E. Enhanced Enantioselectivity in Excitation of Chiral Molecules by Superchiral Light. *Science (1979)* **2011**, *332* (6027), 333–336. https://doi.org/10.1126/science.1202817.

(39) Maoz, B. M.; Chaikin, Y.; Tesler, A. B.; Bar Elli, O.; Fan, Z.;

Govorov, A. O.; Markovich, G. Amplification of Chiroptical Activity of Chiral Biomolecules by Surface Plasmons. *Nano Lett* **2013**, *13* (3), 1203–1209. https://doi.org/10.1021/nl304638a.

(40) Yoo, S. J.; Park, Q. H. Metamaterials and Chiral Sensing: A Review of Fundamentals and Applications. *Nanophotonics* **2019**, *8* (2), 249–261. https://doi.org/10.1515/nanoph-2018-0167.

(41) Solomon, M. L.; Hu, J.; Lawrence, M.; García-Etxarri, A.; Dionne, J. A. Enantiospecific Optical Enhancement of Chiral Sensing and Separation with Dielectric Metasurfaces. *ACS Photonics* **2019**, *6* (1), 43–49. https://doi.org/10.1021/acsphotonics.8b01365.

(42) Wang, Z.; Cheng, F.; Winsor, T.; Liu, Y. Optical Chiral Metamaterials: A Review of the Fundamentals, Fabrication Methods and Applications. *Nanotechnology* **2016**, *27* (41), 412001. https://doi.org/10.1088/0957-4484/27/41/412001.

(43) Tullius, R.; Karimullah, A. S.; Rodier, M.; Fitzpatrick, B.; Gadegaard, N.; Barron, L. D.; Rotello, V. M.; Cooke, G.; Lapthorn, A.; Kadodwala, M. "superchiral" Spectroscopy: Detection of Protein Higher Order Hierarchical Structure with Chiral Plasmonic Nanostructures. *J Am Chem Soc* **2015**, *137* (26), 8380–8383. https://doi.org/10.1021/jacs.5b04806.

(44) Lee, S.; Kang, J. H.; Yoo, S. J.; Park, Q. H. Robust Numerical Evaluation of Circular Dichroism from Chiral Medium/Nanostructure Coupled Systems Using the Finite-Element Method. *Sci Rep* **2018**, *8* (1), 1–8. https://doi.org/10.1038/s41598-018-26815-5.

(45) Govorov, A. O.; Fan, Z.; Hernandez, P.; Slocik, J. M.; Naik, R. R. Theory of Circular Dichroism of Nanomaterials Comprising Chiral Molecules and Nanocrystals: Plasmon Enhancement, Dipole Interactions, and Dielectric Effects. *Nano Lett* **2010**, *10* (4), 1374–1382. https://doi.org/10.1021/nl100010v.

(46) Govorov, A. O. Plasmon-Induced Circular Dichroism of a Chiral Molecule in the Vicinity of Metal Nanocrystals. Application to Various Geometries. *Journal of Physical Chemistry C* **2011**, *115* (16), 7914–7923. https://doi.org/10.1021/jp1121432.

(47) Han, J. H.; Lim, Y. C.; Kim, R. M.; Lv, J.; Cho, N. H.; Kim, H.; Namgung, S. D.; Im, S. W.; Nam, K. T. Neural-Network-Enabled Design of a Chiral Plasmonic Nanodimer for Target-Specific Chirality Sensing. *ACS Nano* **2023**, *17* (3), 2306–2317. https://doi.org/10.1021/acsnano.2c08867.

(48) Schäferling, M.; Yin, X.; Giessen, H. Formation of Chiral Fields in a Symmetric Environment. *Opt Express* **2012**, *20* (24), 26326. https://doi.org/10.1364/OE.20.026326.

(49) Hendry, E.; Carpy, T.; Johnston, J.; Popland, M.; Mikhaylovskiy, R. V.; Lapthorn, A. J.; Kelly, S. M.; Barron, L. D.; Gadegaard, N.; Kadodwala, M. Ultrasensitive Detection and Characterization of Biomolecules Using Superchiral Fields. *Nat Nanotechnol* **2010**, *5* (11), 783–787. https://doi.org/10.1038/nnano.2010.209.

(50) Lipkin, D. M. Existence of a New Conservation Law in Electromagnetic Theory. *J Math Phys* **2004**, *5* (5), 696–700. https://doi.org/10.1063/1.1704165.

(51) Ma, W.; Kuang, H.; Xu, L.; Ding, L.; Xu, C.; Wang, L.; Kotov, N. A. Attomolar DNA Detection with Chiral Nanorod Assemblies. *Nat Commun* **2013**, *4* (1), 2689. https://doi.org/10.1038/ncomms3689.

(52) Han, B.; Zhu, Z.; Li, Z.; Zhang, W.; Tang, Z. Conformation Modulated Optical Activity Enhancement in Chiral Cysteine and Au Nanorod Assemblies. *J Am Chem Soc* **2014**, *136* (46), 16104–16107. https://doi.org/10.1021/ja506790w.

(53) Kuzyk, A.; Schreiber, R.; Fan, Z.; Pardatscher, G.; Roller, E. M.; Högele, A.; Simmel, F. C.; Govorov, A. O.; Liedl, T. DNA-Based Self-Assembly of Chiral Plasmonic Nanostructures with Tailored Optical Response. *Nature* **2012**, *483* (7389), 311–314. https://doi.org/10.1038/nature10889.

(54) Davis, T. J.; Hendry, E. Superchiral Electromagnetic Fields Created by Surface Plasmons in Nonchiral Metallic Nanostructures. *Phys Rev B Condens Matter Mater Phys* **2013**, *87* (8), 1–5. https://doi.org/10.1103/PhysRevB.87.085405.

(55) Probst, P. T.; Mayer, M.; Gupta, V.; Steiner, A. M.; Zhou, Z.; Auernhammer, G. K.; König, T. A. F.; Fery, A. Mechano-Tunable Chiral Metasurfaces via Colloidal Assembly. *Nat Mater* **2021**, *20* (7), 1024–1028. https://doi.org/10.1038/s41563-021-00991-8.

(56) Choi, J. S.; Cho, M. Limitations of a Superchiral Field. *Phys Rev A* **2012**, *86* (6), 1–22. https://doi.org/10.1103/PhysRevA.86.063834.

(57) Auguié, B.; Barnes, W. L. Collective Resonances in Gold Nanoparticle Arrays. *Phys Rev Lett* **2008**, *101* (14), 1–4.

https://doi.org/10.1103/PhysRevLett.101.143902.

(58) Cherqui, C.; Bourgeois, M. R.; Wang, D.; Schatz, G. C. Plasmonic Surface Lattice Resonances: Theory and Computation. *Acc Chem Res* **2019**, *52* (9), 2548–2558. https://doi.org/10.1021/acs.accounts.9b00312.

(59) Im, S. W.; Jo, E.; Kim, R. M.; Han, J. H.; Nam, K. T. 32-Symmetric Chiral Gold Nanoplates with Near-Infrared Circular Dichroism. *Adv Opt Mater* **2023**. https://doi.org/10.1002/adom.202300037.

(60) Lee, Y. Y.; Cho, N. H.; Im, S. W.; Lee, H. E.; Ahn, H. Y.; Nam, K. T. Chiral 432 Helicoid II Nanoparticle Synthesized with Glutathione and Poly(T)20 Nucleotide. *ChemNanoMat* **2020**, *6* (3), 362–367. https://doi.org/10.1002/cnma.201900709.

(61) Kim, J. W.; Cho, N. H.; Lim, Y. C.; Im, S. W.; Han, J. H.; Nam, K. T.; Im, S. W. Controlling the Size and Circular Dichroism of Chiral Gold Helicoids. *Mater Adv* **2021**, *2* (21), 6988–6995. https://doi.org/10.1039/d1ma00783a.

(62) Cho, N. H.; Byun, G. H.; Lim, Y. C.; Im, S. W.; Kim, H.; Lee, H. E.; Ahn, H. Y.; Nam, K. T. Uniform Chiral Gap Synthesis for High Dissymmetry Factor in Single Plasmonic Gold Nanoparticle. *ACS Nano* **2020**, *14* (3), 3595–3602. https://doi.org/10.1021/acsnano.9b10094.

(63) Lee, H. E.; Kim, R. M.; Ahn, H. Y.; Lee, Y. Y.; Byun, G. H.; Im, S. W.; Mun, J.; Rho, J.; Nam, K. T. Cysteine-Encoded Chirality Evolution in Plasmonic Rhombic Dodecahedral Gold Nanoparticles.

*Nat Commun* **2020**, *11* (1), 1–10. https://doi.org/10.1038/s41467-019-14117-x.

(64) Kim, H.; Im, S. W.; Cho, N. H.; Seo, D. H.; Kim, R. M.; Lim, Y. C.; Lee, H. E.; Ahn, H. Y.; Nam, K. T. γ-Glutamylcysteine- and Cysteinylglycine-Directed Growth of Chiral Gold Nanoparticles and Their Crystallographic Analysis. *Angewandte Chemie - International Edition* **2020**, *59* (31), 12976–12983. https://doi.org/10.1002/anie.202003760.

(65) Lee, H.-E.; Ahn, H.-Y.; Mun, J.; Lee, Y. Y.; Kim, M.; Cho, N. H.; Chang, K.; Kim, W. S.; Rho, J.; Nam, K. T. Amino-Acid- and Peptide-Directed Synthesis of Chiral Plasmonic Gold Nanoparticles. *Nature* **2018**, *556* (7701), 360–365. https://doi.org/10.1038/s41586-018-0034-1.

(66) Cho, N. H.; Kim, Y. B.; Lee, Y. Y.; Im, S. W.; Kim, R. M.; Kim, J. W.; Namgung, S. D.; Lee, H. E.; Kim, H.; Han, J. H.; Chung, H. W.; Lee, Y. H.; Han, J. W.; Nam, K. T. Adenine Oligomer Directed Synthesis of Chiral Gold Nanoparticles. *Nat Commun* **2022**, *13* (1). https://doi.org/10.1038/s41467-022-31513-y.

(67) Kim, R. M.; Huh, J. H.; Yoo, S. J.; Kim, T. G.; Kim, C.; Kim, H.; Han, J. H.; Cho, N. H.; Lim, Y. C.; Im, S. W.; Im, E. J.; Jeong, J. R.; Lee, M. H.; Yoon, T. Y.; Lee, H. Y.; Park, Q. H.; Lee, S.; Nam, K. T. Enantioselective Sensing by Collective Circular Dichroism. *Nature* **2022**, *612* (7940), 470–476. https://doi.org/10.1038/s41586-022-05353-1.

(68) Zhang, W.; Martin, O. J. F. A Universal Law for Plasmon Resonance

Shift in Biosensing. *ACS Photonics* **2015**, *2* (1), 144–150. https://doi.org/10.1021/ph500355d.

(69) Lee, Y. Y.; Kim, R. M.; Im, S. W.; Balamurugan, M.; Nam, K. T. Plasmonic Metamaterials for Chiral Sensing Applications. *Nanoscale*. Royal Society of Chemistry January 7, 2020, pp 58–66. https://doi.org/10.1039/c9nr08433a.

(70) Spreyer, F.; Mun, J.; Kim, H.; Kim, R. M.; Nam, K. T.; Rho, J.; Zentgraf, T. Second Harmonic Optical Circular Dichroism of Plasmonic Chiral Helicoid-III Nanoparticles. *ACS Photonics* **2022**, *9* (3), 784–792. https://doi.org/10.1021/acsphotonics.1c00882.

(71) Karst, J.; Cho, N. H.; Kim, H.; Lee, H. E.; Nam, K. T.; Giessen, H.; Hentschel, M. Chiral Scatterometry on Chemically Synthesized Single Plasmonic Nanoparticles. *ACS Nano* **2019**, *13* (8), 8659–8668. https://doi.org/10.1021/acsnano.9b04046.

(72) Cho, N. H.; Lee, H.; Ahn, H.; Lee, Y. Y.; Im, S. W.; Kim, H.; Nam, K. T. Cysteine Induced Chiral Morphology in Palladium Nanoparticle. *Particle & Particle Systems Characterization* **2019**, *36* (5), 1900062. https://doi.org/10.1002/ppsc.201900062.

(73) Lee, S.; Lim, Y. C.; Kim, H.; Seo, D. H.; Na, J.; Kim, H.; Nam, K. T.; Jeong, Y. Random Lasing with a High Degree of Circular Dichroism by Chiral Plasmonic Gold Nanoparticles. *ACS Photonics* **2022**, *9* (2), 613–620. https://doi.org/10.1021/acsphotonics.1c01601.

(74) Kim, S.; Lim, Y. C.; Kim, R. M.; Fröch, J. E.; Tran, T. N.; Nam, K. T.; Aharonovich, I. A Single Chiral Nanoparticle Induced Valley

Polarization Enhancement. *Small* **2020**, *16* (37). https://doi.org/10.1002/smll.202003005.

(75) Ahn, H. Y.; Yoo, S.; Cho, N. H.; Kim, R. M.; Kim, H.; Huh, J. H.; Lee, S.; Nam, K. T. Bioinspired Toolkit Based on Intermolecular Encoder toward Evolutionary 4D Chiral Plasmonic Materials. *Acc Chem Res* **2019**, *52* (10), 2768–2783. https://doi.org/10.1021/acs.accounts.9b00264.

(76) Kim, H.; Im, S. W.; Kim, R. M.; Cho, N. H.; Lee, H. E.; Ahn, H. Y.; Nam, K. T. Chirality Control of Inorganic Materials and Metals by Peptides or Amino Acids. *Materials Advances*. Royal Society of Chemistry 2020, pp 512–524. https://doi.org/10.1039/d0ma00125b.

(77) Kim, J. W.; Cho, N. H.; Kim, R. M.; Han, J. H.; Choi, S.; Namgung, S. D.; Kim, H.; Nam, K. T. Magnetic Control of the Plasmonic Chirality in Gold Helicoids. *Nano Lett* **2022**, *22* (20), 8181–8188. https://doi.org/10.1021/acs.nanolett.2c02661.

(78) Ohnoutek, L.; Cho, N. H.; Allen Murphy, A. W.; Kim, H.; Răsădean, D. M.; Pantoş, G. D.; Nam, K. T.; Valev, V. K. Single Nanoparticle Chiroptics in a Liquid: Optical Activity in Hyper-Rayleigh Scattering from Au Helicoids. *Nano Lett* **2020**, *20* (8), 5792–5798. https://doi.org/10.1021/acs.nanolett.0c01659.

(79) Ryu, J.; Kim, H.; Kim, R. M.; Kim, S.; Jo, J.; Lee, S.; Nam, K. T.; Joo, Y. C.; Yi, G. C.; Lee, J.; Kim, M. Dimensionality Reduction and Unsupervised Clustering for EELS-SI. *Ultramicroscopy* **2021**, *231*. https://doi.org/10.1016/j.ultramic.2021.113314.

(80) Im, S. W.; Ahn, H.-Y.; Kim, R. M.; Cho, N. H.; Kim, H.; Lim, Y.-C.; Lee, H.-E.; Nam, K. T. Chiral Surface and Geometry of Metal Nanocrystals. *Advanced Materials* **2020**, *32* (41), 1905758. https://doi.org/https://doi.org/10.1002/adma.201905758.

(81) Namgung, S. D.; Kim, R. M.; Lim, Y. C.; Lee, J. W.; Cho, N. H.; Kim, H.; Huh, J. S.; Rhee, H.; Nah, S.; Song, M. K.; Kwon, J. Y.; Nam, K. T. Circularly Polarized Light-Sensitive, Hot Electron Transistor with Chiral Plasmonic Nanoparticles. *Nat Commun* **2022**, *13* (1), 5081. https://doi.org/10.1038/s41467-022-32721-2.

(82) Kim, H.; Bang, K. M.; Ha, H.; Cho, N. H.; Namgung, S. D.; Im, S. W.; Cho, K. H.; Kim, R. M.; Choi, W. Il; Lim, Y. C.; Shin, J. Y.; Song, H. K.; Kim, N. K.; Nam, K. T. Tyrosyltyrosylcysteine-Directed Synthesis of Chiral Cobalt Oxide Nanoparticles and Peptide Conformation Analysis. *ACS Nano* **2021**, *15* (1), 979–988. https://doi.org/10.1021/acsnano.0c07655.

(83) 조남헌. Study on Chirality Evolution during Systematic Control of Seed-Mediated Chiral Nanoparticle Synthesis, 2021.

(84) 안효용. Morphology and Chirality Control of Plasmonic Nanoparticle Using Amino Acids and Peptides, 2019.

(85) 김혜온. Circular Dichroism Modulation Based on Plasmon Coupling in Chiral Nanostructures, 2022.

(86) 이혜은. Morphology and Assembly Control of Nanostructures for

Plasmonic Optical Amplification, 서울, 2017.
http://www.riss.kr/link?id=T14507816.

(87) 이윤영. Synthesis and Morphology Control of Plasmonic Nanostructures for Optical Amplification via Seed-Mediated Growth Approach, 서울, 2020. http://www.riss.kr/link?id=T15552375.

(88) 김정원. Study on Active Control of Optical Response from Chiral Plasmonic Nanostructures, 서울, 2022.
http://www.riss.kr/link?id=T16161232.

(89) 임상원. Crystallographic and Morphological Analysis of Chiral Gold Nanoparticles, 서울, 2022. http://www.riss.kr/link?id=T16547826.

(90) 임예찬. Study on Exceptional Point of Non-Hermitian Chiral Plasmonic Nanomaterials, 서울, 2021.
http://www.riss.kr/link?id=T15957112.

(91) Khlopin, D.; Laux, F.; Wardley, W. P.; Martin, J.; Wurtz, G. A.; Plain, J.; Bonod, N.; Zayats, A. V.; Dickson, W.; Gérard, D. Lattice Modes and Plasmonic Linewidth Engineering in Gold and Aluminum Nanoparticle Arrays. *Journal of the Optical Society of America B* **2017**, *34* (3), 691. https://doi.org/10.1364/josab.34.000691.

(92) Kim, M.; Kwon, H.; Lee, S.; Yoon, S. Effect of Nanogap Morphology on Plasmon Coupling. *ACS Nano* **2019**, *13* (10), 12109–12119.

https://doi.org/10.1021/acsnano.9b06492.

(93) Moreau, A.; Ciracì, C.; Mock, J. J.; Smith, D. R.; Hill, R. T.; Chilkoti, A.; Wang, Q.; Wiley, B. J. Controlled-Reflectance Surfaces with Film-Coupled Colloidal Nanoantennas. *Nature*. December 5, 2012, pp 86–89. https://doi.org/10.1038/nature11615.

(94) Abdulrahman, N. A.; Fan, Z.; Tonooka, T.; Kelly, S. M.; Gadegaard, N.; Hendry, E.; Govorov, A. O.; Kadodwala, M. Induced Chirality through Electromagnetic Coupling between Chiral Molecular Layers and Plasmonic Nanostructures. *Nano Lett* **2012**, *12* (2), 977–983. https://doi.org/10.1021/nl204055r.

(95) Cho, N. H.; Guerrero-Martínez, A.; Ma, J.; Bals, S.; Kotov, N. A.; Liz-Marzán, L. M.; Nam, K. T. Bioinspired Chiral Inorganic Nanomaterials. *Nature Reviews Bioengineering* **2023**, *1* (2), 88–106. https://doi.org/10.1038/s44222-022-00014-4.

(96) Wang, J. S.; Wang, G.; Feng, X. Q.; Kitamura, T.; Kang, Y. L.; Yu, S. W.; Qin, Q. H. Hierarchical Chirality Transfer in the Growth of Towel Gourd Tendrils. *Sci Rep* **2013**, *3*. https://doi.org/10.1038/srep03102.

(97) Shibazaki, Y.; Shimizu, M.; Kuroda, R. Body Handedness Is Directed by Genetically Determined Cytoskeletal Dynamics in the Early Embryo. *Current Biology* **2004**, *14*, 1462–1467. https://doi.org/10.1016/j.

(98) Sweeney, A.; Jiggins, C.; Johnsen, S. Polarized Light as a Butterfly Mating Signal. *Nature* **2003**, *423* (6935), 31–32. https://doi.org/10.1038/423031a.

(99) Smith, S. W. Chiral Toxicology: It's the Same Thing Only Different. *Toxicological Sciences*. 2009, pp 4–30. https://doi.org/10.1093/toxsci/kfp097.

(100) Griffiths, D. J. (David J. *Introduction to Electrodynamics*.

(101) Eismann, J. S.; Neugebauer, M.; Banzer, P. Exciting a Chiral Dipole Moment in an Achiral Nanostructure. *Optica* **2018**, *5* (8), 954–959. https://doi.org/10.1364/OPTICA.5.000954.

(102) Kittel, C.; McEuen, P.; McEuen, P. *Introduction to Solid State Physics*; Wiley New York, 1996; Vol. 8.

(103) Ahn, H.-Y.; Lee, H.-E.; Jin, K.; Nam, K. T. Extended Gold Nano-Morphology Diagram: Synthesis of Rhombic Dodecahedra Using CTAB and Ascorbic Acid. *J Mater Chem C Mater* **2013**, *1* (41), 6861. https://doi.org/10.1039/c3tc31135j.

(104) Cho, N. H.; Lee, H.; Ahn, H.; Lee, Y. Y.; Im, S. W.; Kim, H.; Nam, K. T. Cysteine Induced Chiral Morphology in Palladium Nanoparticle. *Particle & Particle Systems Characterization* **2019**, *36* (5), 1900062. https://doi.org/10.1002/ppsc.201900062.

(105) Lee, H.-E.; Lee, J.; Ju, M.; Ahn, H.-Y.; Lee, Y. Y.; Jang, H.-S.; Nam, K. T. Identifying Peptide Sequences That Can Control the Assembly of Gold Nanostructures. *Mol Syst Des Eng* **2018**, *3* (3), 581–590. https://doi.org/10.1039/C7ME00091J.

(106) Lee, H.-E.; Yang, K. D.; Yoon, S. M.; Ahn, H.-Y.; Lee, Y. Y.; Chang, H.; Jeong, D. H.; Lee, Y.-S.; Kim, M. Y.; Nam, K. T. Concave Rhombic Dodecahedral Au Nanocatalyst with Multiple High-Index

Facets for CO 2 Reduction. *ACS Nano* **2015**, *9* (8), 8384–8393. https://doi.org/10.1021/acsnano.5b03065.

(107) Ortega Lorenzo, M.; Baddeley, C. J.; Muryn, C.; Raval, R. Extended Surface Chirality from Supramolecular Assemblies of Adsorbed Chiral Molecules. *Nature* **2000**, *404* (6776), 376–379. https://doi.org/10.1038/35006031.

(108) Ben-Moshe, A.; Wolf, S. G.; Sadan, M. B.; Houben, L.; Fan, Z.; Govorov, A. O.; Markovich, G. Enantioselective Control of Lattice and Shape Chirality in Inorganic Nanostructures Using Chiral Biomolecules. *Nat Commun* **2014**, *5* (1), 4302. https://doi.org/10.1038/ncomms5302.

(109) Ernst, K.-H. Molecular Chirality at Surfaces. *physica status solidi (b)* **2012**, *249* (11), 2057–2088. https://doi.org/10.1002/pssb.201248188.

(110) Baddeley, C. J.; Richardson, N. V. Chirality at Metal Surfaces. In *Scanning Tunneling Microscopy in Surface Science*; Wiley-VCH Verlag GmbH & Co. KGaA: Weinheim, Germany, 2010; Vol. 109, pp 1–27. https://doi.org/10.1002/9783527628827.ch1.

(111) Zaera, F. Chirality in Adsorption on Solid Surfaces. *Chem Soc Rev* **2017**, *46* (23), 7374–7398. https://doi.org/10.1039/C7CS00367F.

(112) Widmer, R.; Haug, F.-J.; Ruffieux, P.; Gröning, O.; Bielmann, M.; Gröning, P.; Fasel, R. Surface Chirality of CuO Thin Films. *J Am Chem Soc* **2006**, *128* (43), 14103–14108. https://doi.org/10.1021/ja0640703.

(113) Kumar, J.; Thomas, K. G.; Liz-Marzán, L. M. Nanoscale Chirality in

Metal and Semiconductor Nanoparticles. *Chemical Communications* **2016**, *52* (85), 12555–12569. https://doi.org/10.1039/C6CC05613J.

(114) Wang, P.; Yu, S.-J.; Govorov, A. O.; Ouyang, M. Cooperative Expression of Atomic Chirality in Inorganic Nanostructures. *Nat Commun* **2017**, *8* (1), 14312. https://doi.org/10.1038/ncomms14312.

(115) Barlow, S. M.; Raval, R. Complex Organic Molecules at Metal Surfaces: Bonding, Organisation and Chirality. *Surf Sci Rep* **2003**, *50* (6–8), 201–341. https://doi.org/10.1016/S0167-5729(03)00015-3.

(116) Zhou, Y.; Yang, M.; Sun, K.; Tang, Z.; Kotov, N. A. Similar Topological Origin of Chiral Centers in Organic and Nanoscale Inorganic Structures: Effect of Stabilizer Chirality on Optical Isomerism and Growth of CdTe Nanocrystals. *J Am Chem Soc* **2010**, *132* (17), 6006–6013. https://doi.org/10.1021/ja906894r.

(117) Yogev-Einot, D.; Avnir, D. Quantitative Symmetry and Chirality of the Molecular Building Blocks of Quartz. *Chemistry of Materials* **2003**, *15* (2), 464–472. https://doi.org/10.1021/cm0207806.

(118) Kim, H.; Im, S. W.; Kim, R. M.; Cho, N. H.; Lee, H.-E.; Ahn, H.-Y.; Nam, K. T. Chirality Control of Inorganic Materials and Metals by Peptides or Amino Acids. *Mater. Adv.* **2020**, *1* (4), 512–524. https://doi.org/10.1039/D0MA00125B.

(119) Oaki, Y.; Imai, H. Amplification of Chirality from Molecules into Morphology of Crystals through Molecular Recognition. *J Am Chem Soc* **2004**, *126* (30), 9271–9275. https://doi.org/10.1021/ja048661+.

(120) Xu, Z.; Qiu, L.; Ding, F. The Kinetics of Chirality Assignment in

Catalytic Single-Walled Carbon Nanotube Growth and the Routes towards Selective Growth. *Chem Sci* **2018**, *9* (11), 3056–3061. https://doi.org/10.1039/C7SC04714B.

(121) Sholl, D. S. Adsorption of Chiral Hydrocarbons on Chiral Platinum Surfaces. *Langmuir* **1998**, *14* (4), 862–867. https://doi.org/10.1021/la9708546.

(122) Horvath, J. D.; Gellman, A. J. Naturally Chiral Surfaces. *Top Catal* **2003**, *25* (1–4), 9–15. https://doi.org/10.1023/B:TOCA.0000003094.07345.d1.

(123) Jiang, W.; Pacella, M. S.; Athanasiadou, D.; Nelea, V.; Vali, H.; Hazen, R. M.; Gray, J. J.; McKee, M. D. Chiral Acidic Amino Acids Induce Chiral Hierarchical Structure in Calcium Carbonate. *Nat Commun* **2017**, *8* (1), 15066. https://doi.org/10.1038/ncomms15066.

(124) Horvath, J. D.; Gellman, A. J. Enantiospecific Desorption of Chiral Compounds from Chiral Cu(643) and Achiral Cu(111) Surfaces. *J Am Chem Soc* **2002**, *124* (10), 2384–2392. https://doi.org/10.1021/ja012182i.

(125) Sugawara, T.; Suwa, Y.; Ohkawa, K.; Yamamoto, H. Chiral Biomineralization: Mirror-Imaged Helical Growth of Calcite with Chiral Phosphoserine Copolypeptides. *Macromol Rapid Commun* **2003**, *24* (14), 847–851. https://doi.org/10.1002/marc.200350030.

(126) Gellman, A. J. Chiral Surfaces: Accomplishments and Challenges. *ACS Nano* **2010**, *4* (1), 5–10. https://doi.org/10.1021/nn901885n.

(127) Flack, H. D. Chiral and Achiral Crystal Structures. *Helv Chim Acta*

**2003**, *86* (4), 905–921. https://doi.org/10.1002/hlca.200390109.

(128) Gellman, A. J.; Horvath, J. D.; Buelow, M. T. Chiral Single Crystal Surface Chemistry. *J Mol Catal A Chem* **2001**, *167* (1–2), 3–11. https://doi.org/10.1016/S1381-1169(00)00484-2.

(129) Hazen, R. M. Chiral Crystal Faces of Common Rock-Forming Minerals. In *Progress in Biological Chirality*; Palyi, G., Zucchi, C., Caglioti, L., Eds.; Elsevier: New York, 2004; pp 137–151. https://doi.org/10.1016/B978-008044396-6/50013-7.

(130) Hazen, R. M.; Sholl, D. S. Chiral Selection on Inorganic Crystalline Surfaces. *Nat Mater* **2003**, *2* (6), 367–374. https://doi.org/10.1038/nmat879.

(131) Gellman, A. J. Enantioselectivity on Naturally Chiral Metal Surfaces. In *Model Systems in Catalysis*; Springer New York: New York, 2010; pp 75–95. https://doi.org/10.1007/978-0-387-98049-2_4.

(132) Sholl, D. S.; Gellman, A. J. Developing Chiral Surfaces for Enantioselective Chemical Processing. *AIChE Journal* **2009**, *55* (10), 2484–2490. https://doi.org/10.1002/aic.12036.

(133) Horvath, J. D.; Koritnik, A.; Kamakoti, P.; Sholl, D. S.; Gellman, A. J. Enantioselective Separation on a Naturally Chiral Surface. *J Am Chem Soc* **2004**, *126* (45), 14988–14994. https://doi.org/10.1021/ja045537h.

(134) Sholl, D. S.; Asthagiri, A.; Power, T. D. Naturally Chiral Metal Surfaces as Enantiospecific Adsorbents. *J Phys Chem B* **2001**, *105* (21), 4771–4782. https://doi.org/10.1021/jp004524x.

(135) Baber, A. E.; Gellman, A. J.; Sholl, D. S.; Sykes, E. C. H. The Real Structure of Naturally Chiral Cu{643}. *The Journal of Physical Chemistry C* **2008**, *112* (30), 11086–11089. https://doi.org/10.1021/jp803601b.

(136) Jiang, W.; Yi, X.; McKee, M. D. Chiral Biomineralized Structures and Their Biomimetic Synthesis. *Mater Horiz* **2019**, 10.1039/C9MH00431A. https://doi.org/10.1039/C9MH00431A.

(137) James, J.; Sholl, D. Theoretical Studies of Chiral Adsorption on Solid Surfaces. *Curr Opin Colloid Interface Sci* **2008**, *13* (1–2), 60–64. https://doi.org/10.1016/j.cocis.2007.08.012.

(138) Kulp, E. A.; Switzer, J. A. Electrochemical Biomineralization: The Deposition of Calcite with Chiral Morphologies. *J Am Chem Soc* **2007**, *129* (49), 15120–15121. https://doi.org/10.1021/ja076303b.

(139) Francis, A. J.; Koritnik, A. J.; Gellman, A.; Salvador, P. A. Chiral Surfaces and Metal/Ceramic Heteroepitaxy in the Pt/SrTiO3(621) System. *Surf Sci* **2007**, *601* (9), 1930–1936. https://doi.org/10.1016/j.susc.2007.02.026.

(140) Greber, T.; Šljivančanin, Ž.; Schillinger, R.; Wider, J.; Hammer, B. Chiral Recognition of Organic Molecules by Atomic Kinks on Surfaces. *Phys Rev Lett* **2006**, *96* (5), 056103. https://doi.org/10.1103/PhysRevLett.96.056103.

(141) Šljivančanin, Ž.; Gothelf, K. V.; Hammer, B. Density Functional Theory Study of Enantiospecific Adsorption at Chiral Surfaces. *J Am Chem Soc* **2002**, *124* (49), 14789–14794.

https://doi.org/10.1021/ja027239v.

(142) Bhatia, B.; Sholl, D. S. Enantiospecific Chemisorption of Small Molecules on Intrinsically Chiral Cu Surfaces. *Angewandte Chemie International Edition* **2005**, *44* (47), 7761–7764. https://doi.org/10.1002/anie.200501655.

(143) Addadi, L.; Geva, M. Molecular Recognition at the Interface between Crystals and Biology: Generation, Manifestation and Detection of Chirality at Crystal SurfacesThis Article Is Based (Partly) on a Presentation Which Will Be Made at the European Research Conference (EURESCO) . *CrystEngComm* **2003**, *5* (26), 140–146. https://doi.org/10.1039/b304061e.

(144) Yun, Y.; Gellman, A. J. Enantiospecific Adsorption of Amino Acids on Naturally Chiral Cu{3,1,17} R&S Surfaces. *Langmuir* **2015**, *31* (22), 6055–6063. https://doi.org/10.1021/acs.langmuir.5b00707.

(145) Rankin, R. B.; Sholl, D. S. Structures of Dense Glycine and Alanine Adlayers on Chiral Cu(3,1,17) Surfaces. *Langmuir* **2006**, *22* (19), 8096–8103. https://doi.org/10.1021/la0613272.

(146) Raval, R. Chiral Expression from Molecular Assemblies at Metal Surfaces: Insights from Surface Science Techniques. *Chem Soc Rev* **2009**, *38* (3), 707. https://doi.org/10.1039/b800411k.

(147) Gladys, M. J.; O'Donnell, K.; Tadich, A.; Yook, H.; Han, J. W.; Thomsen, L. Enantiospecific Adsorption and Decomposition of Cysteine Enantiomers on the Chiral Cu{421} R Surface. *The Journal of Physical Chemistry C* **2019**, *123* (34), 20829–20837.

https://doi.org/10.1021/acs.jpcc.9b03373.

(148) Gladys, M. J.; Han, J. W.; Pedersen, T. S.; Tadich, A.; O'Donnell, K. M.; Thomsen, L. Adsorption Differences between Low Coverage Enantiomers of Alanine on the Chiral Cu{421} R Surface. *Physical Chemistry Chemical Physics* **2017**, *19* (21), 13562–13570. https://doi.org/10.1039/C7CP01844D.

(149) Orme, C. A.; Noy, A.; Wierzbicki, A.; McBride, M. T.; Grantham, M.; Teng, H. H.; Dove, P. M.; DeYoreo, J. J. Formation of Chiral Morphologies through Selective Binding of Amino Acids to Calcite Surface Steps. *Nature* **2001**, *411* (6839), 775–779. https://doi.org/10.1038/35081034.

(150) Cody, A. M.; Cody, R. D. Chiral Habit Modifications of Gypsum from Epitaxial-like Adsorption of Stereospecific Growth Inhibitors. *J Cryst Growth* **1991**, *113* (3–4), 508–519. https://doi.org/10.1016/0022-0248(91)90086-K.

(151) Soai, K.; Osanai, S.; Kadowaki, K.; Yonekubo, S.; Shibata, T.; Sato, I. D - and l -Quartz-Promoted Highly Enantioselective Synthesis of a Chiral Organic Compound. *J Am Chem Soc* **1999**, *121* (48), 11235–11236. https://doi.org/10.1021/ja993128t.

(152) Horvath, J. D.; Gellman, A. J. Enantiospecific Desorption of R - and S -Propylene Oxide from a Chiral Cu(643) Surface. *J Am Chem Soc* **2001**, *123* (32), 7953–7954. https://doi.org/10.1021/ja015890c.

(153) Soai, K.; Osanai, S.; Kadowaki, K.; Yonekubo, S.; Shibata, T.; Sato, I. D - and l -Quartz-Promoted Highly Enantioselective Synthesis of a

Chiral Organic Compound. *J Am Chem Soc* **1999**, *121* (48), 11235–11236. https://doi.org/10.1021/ja993128t.

(154) Horvath, J. D.; Baker, L.; Gellman, A. J. Enantiospecific Orientation of R –3-Methylcyclohexanone on the Chiral Cu(643) R / S Surfaces. *The Journal of Physical Chemistry C* **2008**, *112* (20), 7637–7643. https://doi.org/10.1021/jp0753878.

(155) Levy-Lior, A.; Weiner, S.; Addadi, L. Achiral Calcium-Oxalate Crystals with Chiral Morphology from the Leaves of Some Solanacea Plants. *Helv Chim Acta* **2003**, *86* (12), 4007–4017. https://doi.org/10.1002/hlca.200390334.

(156) Horvath, J. D.; Gellman, A. J. Enantiospecific Desorption of R - and S -Propylene Oxide from a Chiral Cu(643) Surface. *J Am Chem Soc* **2001**, *123* (32), 7953–7954. https://doi.org/10.1021/ja015890c.

(157) Song, H. S.; Han, J. W. Tuning the Surface Chemistry of Chiral Cu(531) S for Enhanced Enantiospecific Adsorption of Amino Acids. *The Journal of Physical Chemistry C* **2015**, *119* (27), 15195–15203. https://doi.org/10.1021/acs.jpcc.5b02695.

(158) Yun, Y.; Wei, D.; Sholl, D. S.; Gellman, A. J. Equilibrium Adsorption of <scp>d</Scp> - and <scp>l</Scp> -Alanine Mixtures on Naturally Chiral Cu{3,1,17} R&S Surfaces. *The Journal of Physical Chemistry C* **2014**, *118* (27), 14957–14966. https://doi.org/10.1021/jp503796u.

(159) Power, T. D.; Asthagiri, A.; Sholl, D. S. Atomically Detailed Models of the Effect of Thermal Roughening on the Enantiospecificity of

Naturally Chiral Platinum Surfaces. *Langmuir* **2002**, *18* (9), 3737–3748. https://doi.org/10.1021/la011535o.

(160) Yun, Y.; Gellman, A. J. Enantioselective Separation on Naturally Chiral Metal Surfaces: <scp>d,L</Scp> -Aspartic Acid on Cu(3,1,17) *R* & *S* Surfaces. *Angewandte Chemie International Edition* **2013**, *52* (12), 3394–3397. https://doi.org/10.1002/anie.201209025.

(161) Fajín, J. L. C.; Gomes, J. R. B.; Cordeiro, M. N. D. S. DFT Study of the Adsorption of <scp>d</Scp> - ( <scp>l</Scp> - )Cysteine on Flat and Chiral Stepped Gold Surfaces. *Langmuir* **2013**, *29* (28), 8856–8864. https://doi.org/10.1021/la401057f.

(162) Arteaga, O.; Sancho-Parramon, J.; Nichols, S.; Maoz, B. M.; Canillas, A.; Bosch, S.; Markovich, G.; Kahr, B. Relation between 2D/3D Chirality and the Appearance of Chiroptical Effects in Real Nanostructures. *Opt Express* **2016**, *24* (3), 2242. https://doi.org/10.1364/oe.24.002242.

(163) Wu, H. L.; Tsai, H. R.; Hung, Y. T.; Lao, K. U.; Liao, C. W.; Chung, P. J.; Huang, J. S.; Chen, I. C.; Huang, M. H. A Comparative Study of Gold Nanocubes, Octahedra, and Rhombic Dodecahedra as Highly Sensitive SERS Substrates. *Inorg Chem* **2011**, *50* (17), 8106–8111. https://doi.org/10.1021/ic200504n.

(164) Goerlitzer, E. S. A.; Zapata-Herrera, M.; Ponomareva, E.; Feller, D.; Garcia-Etxarri, A.; Karg, M.; Aizpurua, J.; Vogel, N. Molecular-Induced Chirality Transfer to Plasmonic Lattice Modes. *ACS Photonics* **2023**. https://doi.org/10.1021/acsphotonics.3c00174.

(165) Odom, T. W.; Love, J. C.; Wolfe, D. B.; Paul, K. E.; Whitesides, G. M. Improved Pattern Transfer in Soft Lithography Using Composite Stamps. *Langmuir* **2002**, *18* (13), 5314–5320. https://doi.org/10.1021/la020169l.

(166) Chen, H.; Kou, X.; Yang, Z.; Ni, W.; Wang, J. Shape- and Size-Dependent Refractive Index Sensitivity of Gold Nanoparticles. *Langmuir* **2008**, *24* (10), 5233–5237. https://doi.org/10.1021/la800305j.

(167) Juodenas, M.; Tamulevičius, T.; Henzie, J.; Erts, D.; Tamulevičius, S. Surface Lattice Resonances in Self-Assembled Arrays of Monodisperse Ag Cuboctahedra. *ACS Nano* **2019**, *13* (8), 9038–9047. https://doi.org/10.1021/acsnano.9b03191.

(168) Shafiei, F.; Monticone, F.; Le, K. Q.; Liu, X. X.; Hartsfield, T.; Alù, A.; Li, X. A Subwavelength Plasmonic Metamolecule Exhibiting Magnetic-Based Optical Fano Resonance. *Nat Nanotechnol* **2013**, *8* (2), 95–99. https://doi.org/10.1038/nnano.2012.249.

(169) Gurvitz, E. A.; Ladutenko, K. S.; Dergachev, P. A.; Evlyukhin, A. B.; Miroshnichenko, A. E.; Shalin, A. S. The High-Order Toroidal Moments and Anapole States in All-Dielectric Photonics. *Laser Photon Rev* **2019**, *13* (5), 1–13. https://doi.org/10.1002/lpor.201800266.

(170) Shahmoon, E.; Wild, D. S.; Lukin, M. D.; Yelin, S. F. Cooperative Resonances in Light Scattering from Two-Dimensional Atomic Arrays. *Phys Rev Lett* **2017**, *118* (11), 113601. https://doi.org/10.1103/PhysRevLett.118.113601.

(171) Wang, F.; Shen, Y. R. General Properties of Local Plasmons in Metal Nanostructures. *Phys Rev Lett* **2006**, *97* (20), 1–4. https://doi.org/10.1103/PhysRevLett.97.206806.

(172) Jung, L. S.; Campbell, C. T.; Chinowsky, T. M.; Mar, M. N.; Yee, S. S. Quantitative Interpretation of the Response of Surface Plasmon Resonance Sensors to Adsorbed Films. *Langmuir* **1998**, *14* (19), 5636–5648. https://doi.org/10.1021/la971228b.

(173) Lindell, I. V. Electromagnetic Waves in Chiral and Bi-Isotropic Media; 1994.

(174) Sreekanth, K. V.; Alapan, Y.; Elkabbash, M.; Ilker, E.; Hinczewski, M.; Gurkan, U. A.; De Luca, A.; Strangi, G. Extreme Sensitivity Biosensing Platform Based on Hyperbolic Metamaterials. *Nat Mater* **2016**, *15* (6), 621–627. https://doi.org/10.1038/nmat4609.

(175) Park, J. H.; Ndao, A.; Cai, W.; Hsu, L.; Kodigala, A.; Lepetit, T.; Lo, Y. H.; Kanté, B. Symmetry-Breaking-Induced Plasmonic Exceptional Points and Nanoscale Sensing. *Nat Phys* **2020**, *16* (4), 462–468. https://doi.org/10.1038/s41567-020-0796-x.

(176) Nusz, G. J.; Marinakos, S. M.; Curry, A. C.; Dahlin, A.; Hook, F.; Wax, A.; Chilkoti, A. Label-Free Plasmonic Detection of Biomolecular Binding by a Single Gold Nanorod. *Anal Chem* **2008**, *80* (4), 984–989. https://doi.org/10.1021/ac7017348.

(177) Nelson, S. G.; Johnston, K. S.; Yee, S. S. High Sensitivity Surface Plasmon Resonance Sensor Based on Phase Detection. *Sens Actuators B Chem* **1996**, *35* (1–3), 187–191.

https://doi.org/10.1016/S0925-4005(97)80052-4.

(178) Nelson, B. P.; Grimsrud, T. E.; Liles, M. R.; Goodman, R. M.; Corn, R. M. Surface Plasmon Resonance Imaging Measurements of DNA and RNA Hybridization Adsorption onto DNA Microarrays. *Anal Chem* **2001**, *73* (1), 1–7. https://doi.org/10.1021/ac0010431.

(179) Zhang, X.; Servos, M. R.; Liu, J. Instantaneous and Quantitative Functionalization of Gold Nanoparticles with Thiolated DNA Using a PH-Assisted and Surfactant-Free Route. *J Am Chem Soc* **2012**, *134* (17), 7266–7269. https://doi.org/10.1021/ja3014055.

(180) Šípová, H.; Zhang, S.; Dudley, A. M.; Galas, D.; Wang, K.; Homola, J. Surface Plasmon Resonance Biosensor for Rapid Label-Free Detection of Microribonucleic Acid at Subfemtomole Level. *Anal Chem* **2010**, *82* (24), 10110–10115. https://doi.org/10.1021/ac102131s.

(181) Pobbati, A. V.; Stein, A.; Fasshauer, D. N- to C-Terminal SNARE Complex Assembly Promotes Rapid Membrane Fusion. *Science (1979)* **2006**, *313* (5787), 673–676. https://doi.org/10.1126/science.1129486.

(182) Kim, C.; Shon, M. J.; Kim, S. H.; Eun, G. S.; Ryu, J. K.; Hyeon, C.; Jahn, R.; Yoon, T. Y. Extreme Parsimony in ATP Consumption by 20S Complexes in the Global Disassembly of Single SNARE Complexes. *Nat Commun* **2021**, *12* (1), 1–15. https://doi.org/10.1038/s41467-021-23530-0.

(183) Ryu, J.-K.; Min, D.; Rah, S.-H.; Kim, S. J.; Park, Y.; Kim, H.; Hyeon,

C.; Kim, H. M.; Jahn, R.; Yoon, T.-Y. Spring-Loaded Unraveling of a Single SNARE Complex by NSF in One Round of ATP Turnover. *Science (1979)* **2015**, *347* (6229), 1485–1489. https://doi.org/10.1126/science.aaa5267.

(184) Liang, B.; Kiessling, V.; Tamm, L. K. Prefusion Structure of Syntaxin-1A Suggests Pathway for Folding into Neuronal Trans-SNARE Complex Fusion Intermediate. *Proc Natl Acad Sci U S A* **2013**, *110* (48), 19384–19389. https://doi.org/10.1073/pnas.1314699110.

# 초 록

분자의 카이랄성을 극도로 민감하게 감지하고 정밀하게 분석하는 것은 자연현상의 여러 가지 현상을 이해하고 제어할 수 있는 능력 때문에 생물학, 물리학, 화학, 심지어 약학을 포함한 광범위한 분야에서 중요한 이슈가 되었다. 카이랄 생물 분자와 편광 사이의 특정 빛-물질 상호작용에 대한 이해는 이러한 상호작용을 카이랄성에 따른 투과, 흡수, 산란을 측정함으로써 분석하는 분광학적 기법이 발전되어 왔다. 대표적으로, 왼쪽 원편광 (LCP)과 오른쪽 원편광 (RCP) 사이의 흡수 차이를 측정하는 원편광 이성질 (CD)과 초기 광축의 회전을 분석하는 광학 회전 분산 (ORD)은 분자 카이랄성에 대한 비침습적이고 간단한 탐지 기술로 입증되어 왔다. 그러나, 몇 나노미터 크기의 분자와 수백 나노미터 규모의 빛 사이의 큰 규모 불일치는 빛-물질 상호작용의 강도를 감소시키며, 이는 분자 카이랄성의 검출 한계를 낮출 수 있다.

최근에는 플라즈모닉 재료의 국소 표면 플라즈몬 공명 (LSPR)을 이용하는 나노 광학 카이랄 센싱 시스템이 개발되어 카이랄성 분석에 대한 민감도를 증폭시킬 수 있음이 밝혀졌다. 이 시스템은 빛의 카이랄 에너지(즉, 광학 헬리시티 밀도)를 분자 규모로 집중시킴으로써 빛과 물질간의 상호작용과 분자의 CD 응답을 향상시킬 수 있다. 그러나 카이랄 플라즈모닉 구조에 의한 광학 헬리시티 밀도의 약하고 비균일적인 증폭으로 인한 민감도 부족 및 메커니즘 이해의 부재는 재현성 문제를 야기하고, 결국 나노 광학 카이랄 센싱 플랫폼의 실제적인 활용을 제한하게 되었다. 따라서, 나노 광학 카이랄 센싱에 대한 메커니즘적인 조사와 광학 헬리시티 밀도를 균일하게 증폭시킬 수 있는 카이랄 나노구조체의 개발은 카이랄성 감지를 위한 나노 광학 시스템의 실제적인 응용에 있어 중요한 과제가 되었다. 이 연구를 통해, 우리는

2 차원적으로(2D) 정렬된 카이랄 플라즈모닉 나노입자(헬리코이드), 즉 2D 헬리코이드 크리스탈의 집단 공명(CR)을 이용하고, 분자의 카이랄성에 따라 변하는 2D 정렬 카이랄 플라즈모닉 나노구조체의 CD 응답을 모니터링하는 것이 위에서 언급한 한계를 해결하는 유망한 전략을 개발하고자 하였다. 본 학위논문에서는, 헬리코이드 간의 플라즈모닉 커플링(즉, CR)과 에너지 재분배 측면에서 카이랄 빛-물질 상호작용을 이해함으로써 나노 광학 카이랄 센싱의 원리를 해석할 수 있는 카이랄 섭동 이론을 이용하여 카이랄 빛-물질 상호작용을 크게 증폭시켜 육안으로도 카이랄성을 감지할 수 있는 새로운 카이랄 센싱 플랫폼을 제시하고자 한다.

본 연구실에서 개발된 생체 분자를 사용하여 자유로운 카이랄 광특성 조절이 가능한 카이랄 금 나노 입자 (헬리코이드)를 대량 합성하는 전략의 개발은 다양한 응용 분야에서 카이랄 플라즈모닉 나노구조체를 실용적으로 활용하는 길을 열었다. 본 학위 연구에서는 이러한 플라즈모닉 나노 입자의 광특성은 입자 간의 결합 공명을 이용하여 증폭하고 최적화 될 수 있다. 증폭된 플라즈몬 공명의 대표적인 방법으로는, 입사광의 파장 주기로 플라즈모닉 나노 입자를 2D 로 정렬하면 LSPR 과 회절 모드 간의 혼성화를 유발할 수 있으며, 이는 나노 입자의 집단 공명을 유발할 수 있다. 집단 공명은 플라즈몬 공명의 품질을 개선할 수 있으며, 효과적으로 입사광을 2D 표면을 따라 가이딩 함으로써 빛-물질 상호작용을 증폭시키고 플라즈모닉 센서의 민감도를 향상시키는 유용한 전략으로 간주되었다. 그러나, 2D 정렬된 카이랄 플라즈모닉 나노구조체에서의 집단 공명과 그로 인한 CD 응답은 2D 및 주기적으로 정렬된 카이랄 플라즈모닉 나노 구조체의 제작 어려움으로 인해 알려지지 않은 영역에 존재한다. 본 학위 논문에서, 우리는 콜로이드 합성된 헬리코이드를 2D 로 정렬하는 방법론을 개발하고, 광학 헬리시티 밀도(빛의 카이랄 필드)의 효과적인 집적을 위한 제작된 나노 구조체의 광특성을 분석했습니다. 본 연구를 통해 제작된 2D 헬리코이드 결정의 경우, LSPR 과

회절 모드 간의 모드 혼성화를 제어하는 것이 간단하고 쉬워서, 집단 공명 모드를 형성하고 2D 헬리코이드 결정에서 강한 카이랄 광응답을 유발할 수 있다. 특히, 400 nm 주기성으로 정렬된 180-nm 크기의 헬리코이드는 원형편광 빛(CPL)의 60 도 기울어진 입사에서 최적의 카이랄 광응답을 보였다.

카이랄 플라즈모닉 구조체을 카이랄 센서로 활용하는 기존 연구들은 카이랄 플라즈모닉 나노구조체에 의한 광학 헬리시티의 향상을 통한 분자 CD 의 증강에 초점을 맞추고 있다. 그러나, 카이랄 플라즈모닉 나노구조체에 의한 단순한 광학 헬리시티 밀도의 증강과 분자 CD 와 플라즈몬 공명 파장 간의 스펙트럼 불일치는 센서 특성의 재현성 문제를 야기한다. 본 학위논문에서는 2D 헬리코이드 결정의 강한 카이랄 광반응과 그로 인한 광학 헬리시티 밀도를 극도로 민감한 카이랄 센싱 플랫폼으로서의 응용을 위한 연구를 진행하였다. 432 회전 대칭 카이랄 형태를 가진 헬리코이드의 카이랄 광 특성은 집단 공명 파장에서 TE 와 TM 모드의 겹침을 유발함으로써 2 차원상 나노 입자간 커플링이 발생하는 상황에서도 그들의 카이랄성이 유지될 수 있다. 또한, TE/TM 모드의 원형 편광 빛(CPL)과 같은 위상 차이는 전자기(EM) 시뮬레이션을 통해 식별되었으며, 이로 인해 2D 헬리코이드 결정의 유도 전기 쌍극자가 실시간 회전함이 확인되었다. 더욱이, 이러한 전기 쌍극자의 집단적인 회전은 헬리코이드가 2D 로 정렬된 표면을 따라 산란된 전기장 쌍극자의 집단적인 회전을 유발하며, 이는 2D 헬리코이드 결정의 집단 공명이 균일한 카이랄 산란 필드(즉, 균일하고 강한 광학 헬리시티 밀도)를 생성함을 시사한다. 본 학위논문에서는 기존의 분자 CD 증강이론과 다르게, 균일하고 강한 광학 헬리시티 밀도를 카이랄 센싱에 실제로 적용하기 위해, 분자 CD 증강이 아닌 카이랄 분자 에너지의 섭동을 카이랄 플라즈모닉 나노구조체의 CD 반응에 연관시킬 수 있는 새로운 카이랄 섭동 이론을 개발하였다. 이러한 결과들은 2D 헬리코이드 결정의 균일하고 강한 광학 헬리시티가 카이랄 빛-물질 상호작용을 증강시키는 데 중요한 요인이며, 이로 인해

플라즈모닉 구조체에 대한 분자의 카이랄 섭동이 증가하므로, 민감한 카이랄 센싱에 필수적임을 보인다.

현재 카이랄 플라즈모닉 나노 구조체에 의한 카이랄 센싱에 대한 연구는 재현성 문제로 인해 센서 특성의 실험적 증거를 제공하기보다는 이론적으로 센서 특성을 입증하고 있는 추세이다. 분자의 방향, 상대 농도, 위치가 달라짐에 따라 결과적인 광학 응답이 상이하게 발생한다. 이러한 맥락에서, 우리는 2D 헬리코이드 결정을 기반으로 한 새롭게 개발된 카이랄 센싱에 대한 이론적 해석의 신뢰성을 실험적으로 검증하였다. 본 학위논문에서, 우리는 대표적 아미노산인 프롤린 분자에 대한 2D 헬리코이드 결정의 분자 카이랄성 선택적인 CD 응답을 확인하였다. 또한, CD 응답의 변화 정도는 프롤린 분자의 다양한 농도와 부피에 대해 유지되었으며, 검출 한계를 수 mM 및 수 μL 범위로 달성하였다. 더욱이, 분자 카이랄성 선택적인 CD 응답은 2D 헬리코이드 결정의 카이랄성 선택적 편광 색 변화를 유도하여 분자 카이랄성의 육안 판별도 가능하게 하였다.

2D 헬리코이드 결정의 강하고 균일한 광학 헬리시티 밀도는 2D 헬리코이드 결정 위에서 DNA-RNA 혼성화 및 단백질 구조 변화를 동반하는 생체 기작에서 발생하는 카이랄성 변화의 검출도 가능케 하였다. 본 학위연구에서는 마이크로 RNA(mRNA)와 단백질 복합체와 같은 다양한 종류의 생체 분자의 카이랄성 변화를 검출하기 위한 2D 헬리코이드 결정의 집단 CD 의 확장성과 실질적 적용 가능성을 확인하였다. mRNA 와 단백질 복합체에 대한 카이랄 센싱 실험을 실시하기 위해, 각 생체분자는 특정 특이적 상호작용을 통해 2D 헬리코이드 결정에 고정되었고, DNA 와 단백질 구조 변화 유발제 등의 결합 대상이 결합되었을 때 각 생체 분자의 구조가 변화하면서 집단 CD 의 변화를 감지하고자 하였다. 이를 통해, mRNA 와 단백질 복합체의 카이랄성이 변할 때 집단 CD 응답의 파장과 강도가 변화한다는 것을 확인하였고, 이를 통해 분자의 종류에 상관없이 2D 헬리코이드 결정의

카이랄성 변화 검출 가능성을 확인하였습니다. 또한, 2D 헬리코이드 결정은 반사형 광학 시스템을 사용하는 상용 표면 플라즈몬 공명(SPR) 센싱 시스템에 통합 될 수 있음을 보였으며, 그 결과 집단 CD 응답과 그들의 카이랄성 선택적 CD 변화를 기존 상용화된 광학계에서도 확인할 수 있었다.

결론적으로, 본 학위논문에서는 2D 헬리코이드 결정의 제작과 집단 공명 및 CD 에 대한 특성파악을 실험, 시뮬레이션, 이론의 관점에서 달성하였다. 또한, 아미노산, DNA, 단백질을 포함한 다양한 생체 분자 카이랄성 검출을 통해 본 학위연구를 통해 밝혀진 2D 헬리코이드 결정의 카이랄성 민감도가 분석물의 부피, 사용되는 광학계에 관계없이 통용될 수 있는 결과임을 입증하였다. 이러한 결과는 초 고민감도 분자 카이랄성 검출을 위한 새로운 카이랄 플라즈모닉 나노입자 시스템의 개발과 연구가 카이랄 플라즈모닉 구조체 기반의 실제 및 실질적인 카이랄 센싱 응용을 용이하게 할 것이라고 기대한다.

주요어: 카이랄성, 2차원 정렬된 카이랄 나노 입자 (2D 헬리코이드 결정), 헬리코이드, 432 대칭성, 원편광 이색성, 집단 공명, 집단 CD, 광학 헬리시티 밀도, 카이랄 섭동 이론.

학번: 2018-28151

# 감사의 글

5년 반이라는 긴 시간 동안 많은 분의 응원과 도움 덕분에 박사과정을 통해 연구를 배우고 한층 더 성장할 수 있었습니다. 그동안 저를 이끌어주시고 소중한 경험을 만들어 주신 여러 교수님과 선후배, 동료, 친구, 그리고 가족들에게 진심을 담아 감사의 말씀을 드립니다.

먼저 가장 오랜 시간 동안 저를 지도해 주시며 연구자로서 첫 걸음을 뗄 수 있도록 해주신 남기태 교수님께 가장 큰 감사의 인사를 드립니다. 부족한 저를 이끌어주시고 성장할 수 있도록 격려해주신 덕분에 박사과정 동안 좋은 연구 기회들을 얻을 수 있었습니다. 교수님께 배운 연구에 임하는 자세, 연구 방법, 그리고 문제를 해결하는 전략들은 제가 앞으로 어려움이 닥쳤을 때 이겨낼 수 있는 자양분이 될 것이며 항상 앞서서 보여주시는 연구에 대한 열정과 끈기, 직관은 앞으로도 저를 성장시킬 수 있는 거름이 되리라 믿습니다. 그동안 지도해 주셔서 감사드리며 앞으로도 좋은 연구자, 자랑스러운 제자가 될 수 있도록 더 발전하겠습니다.

또한 귀한 시간 내어 저의 학위 심사를 허락해 주시고 귀중한 코멘트와 조언을 아낌없이 주신 심사위원 교수님 그리고 박사님 분들, 김미영 교수님, 이명재 교수님, 박성규 박사님, 유은아 박사님께 대단히 감사드립니다. 학위 심사 과정을 잊지 않고 깊이 되새기며 더 성장할 수 있도록 하겠습니다. 박사 과정을 통해 뵙게 된 여러 교수님들과 연구원님들께도 감사드립니다. 광학과 플라즈모닉스에 대해 무지할 때 아낌 없는 조언과 디스커션을 해주신 이승우 교수님, 박규환 교수님, 유석재 교수님, 그리고 이제는 교수님이 되신 허지혁 박사님, 임은지 연구원님께 깊이 감사드립니다. 아직 연구의 결실을 맺지 못했지만 끊임없는 도전정신과 열정을 보여주시는 정대홍 교수님, 이호영 교수님, 박홍규 교수님, 김동하 교수님, 소재필 박사님, 이순재 연구원님, 강하은 연구원님,  이성균 연구원님께 감사드립니다. 저의 첫 연구 논문 작성과정에 큰 도움을 주신 윤태영 교수님, 이민형 교수님, 김창원 박사님,

김태균 연구원님, 정재렬 연구원님께 감사한 마음을 전합니다. 하나의 연구과제로 시작해 미래를 바꿀 수 있는 기술을 연구하는데 큰 도움주신 송윤주 교수님, 최준일 교수님, 박정훈 교수님, 권민상 교수님, 유필진 교수님, 박경수 교수님, 한건호 연구원님, 정윤돈 연구원님, 유제승 연구원님, 최혁진 연구원님, 김동현 연구원님, 최용우 연구원님께 감사한 마음을 전합니다.

긴 학위 과정 동안 함께해준 BMNL 연구실 식구들에게도 큰 감사를 드립니다. 아무것도 모르는 1 년차 학생일때부터 하나씩 차근차근 가르쳐 주셨던 선배 박사, 석사님들, 이재훈, 김영혜, 양기동, 정희윤, 이혜은, 안효용, 이윤영, 조남헌, 김혜온, 임상원, 최승우, 홍정석, 정희윤, 서홍민, 박승학, 조강희, 남궁석, 이종우, 오레나, Dr. Bala, Dr. Ashim, Dr. Jiawei, Dr. Qianqian, 장준호, 하탁래, 주미송, 이강규, 서다혜, 임예찬, 이규민, 고창완, 김성호, 김정원 님들께 진심으로 감사드립니다. 선 후배 님들이 있었기에 학위 과정을 잘 마칠 수 있었습니다. 연구실 생활을 넘어 기쁨, 슬픔을 모두 공유하고 힘든 시기를 잘 버틸 수 있게 도와준 이윤호, 김정은, 이무영, 샘, 최원일, 조욱현 연구원님들께 감사함을 전합니다. 이들이 있었기에 행복할 수 있었고, 좌절하더라도 꾸준히 연구에 정진할 수 있었습니다.

소중한 플라즈몬 팀 사람들에게 특별한 감사의 마음을 전합니다. 먼저 아무것도 모르는 저를 이끌어 주시고 제가 가장 많이 의지하고 모든 면에서 저의 멘토로 삼았던 플라즈몬팀의 어머니 이혜은 박사님께 깊은 감사의 마음을 전합니다. 비록 짧은 시간이었지만 박사님께 배우고 함께 연구할 수 있어 영광이었습니다. 항상 그래 오셨듯이 지금 하고 계신 연구가 잘 마무리되어 원하시는 바를 꼭 이루시기 기원 드립니다. 실질적으로 저를 가장 많이 도와주셨고 제가 심적으로나 연구적으로나 가장 많이 의지했던 안효용 박사님께 깊은 감사의 마음을 전합니다. 아무것도 모르는 저에게 차근차근 연구가 무엇인지, 어떻게 연구를 해야 하는지 고민하고 있을 때 가장 먼저 다가와 알려주셔서 감사합니다. 안효용 박사님의 따듯한 말과 진심어린 조언이 아니었다면 지금의 학위 과정을 마치지 못했을 것입니다. 힘든 시기를 보내고 계시지만, 늘 그래 오셨듯

잘 해결 하시리라 믿고 원하시는 바를 꼭 이루시길 바랍니다. 플라즈몬 팀의 분위기 메이커 이윤영 박사님께도 감사의 마음을 전합니다. 연구뿐 아니라 심적으로 항상 좋은 분위기와 기분을 만드는 것이 얼마나 중요한지 알려주셔서 감사합니다. 가장 힘들었던 시기에 이윤영 박사님의 유쾌하고 따듯한 조언이 아니었다면 학위 과정을 마무리하지 못했을 것 같습니다. 박사님의 성품이라면 어디서 무엇을 하시던 모두 잘 해내시리라 믿습니다. 플라즈몬 팀이 가장 위태한 시기에 등장해주신 조남헌 박사님께 깊은 감사를 드립니다. 너무나 뛰어난 연구 및 정리 능력으로 한때는 많이 시기하고 질투하던 때가 있었지만 오랜 시간 박사님과 함께 연구, 생활하며 많은 것을 배웠고 위태롭던 저의 학위 시기에 많은 의지가 되어 주셨습니다. 어려운 연구 주제로 고군분투하고 계시지만 박사님의 능력이라면 분명 잘 해내시리라 믿어 의심치 않고, 가까운 미래에 원하시는 바를 달성하여 뵙기를 바랍니다. 저의 유일한 박사 동기이자 어수선한 연구실 생활 가운데 항상 차분한 성품으로 맡은 바를 성실하고 차분히 해내시는 배려심의 아이콘 김혜온 박사님, 저의 학위 과정을 지켜주시고 힘들 때 찾아와 아낌없는 조언을 해주신 남궁석 박사님, 광학 테이블을 본격적으로 사용할 수 있도록 도와주신 이종우 교수님, 남다른 연구 센스를 가진 임상원 박사님께 감사함을 전합니다. 스마트함과 남다른 유머 코드로 연구실 생활을 즐겁게 만들어준 임예찬 연구원님, 발표를 너무 잘하고 남다른 정리 능력으로 훌륭한 교수가 될 이윤호 연구원님, 울보이긴 하지만 연구에 대한 열정이 넘치는 김정원 연구원님, 때로는 감당 안될 만큼 기쁨을 전파하는 서다혜 연구원님, 선배에게 항상 깍듯한 김성호 연구원님께 깊이 감사함을 전합니다. 차기 플라즈몬 팀 팀장이자 후배이지만 항상 배울점이 많고 능력이 너무 많은 한정현 연구원님께 특별한 감사함을 전합니다. 가장 힘든 시기에 구원 투수처럼 나타나 큰 도움을 주고 심적으로나 연구적으로나 우수함을 보여주어 많은 귀감이 되었습니다. 큰 도움이 되지 못해 아쉽고, 연구실에 함께 있을 시간이 얼마 남지 않았다는 것이 슬프지만 항상 그래왔듯 학위 과정을 잘 해낼 수 있으리라 믿어 의심치 않습니다. 도움이 필요할 땐 언제든 연락해도 좋고 연구실에 없더라도 자주 연락하고 지낼 수 있는 좋은 인연이 되길 진심으로 바랍니다. 새로이 골드

팀에 합류하여 벌써부터 우수한 연구 능력을 보여주는 하인한 연구원님, 편견 없이 꾸준하고 성실하게 연구에 임하는 이수민 연구원님, 끈기있는 모습으로 악착같이 연구하는 조은정 연구원님, 새로운 주제로 힘들어 하지만 잘 해낼 조성훈 연구원님, 짧은 시간이라 많은 이야기를 나누지 못해 아쉽지만 모두 원하시는 바를 이루기를 기원합니다.

BMNL 연구실에서 저의 마지막을 함께 빛내주신 현 멤버들께도 깊은 감사를 드립니다. 연구실 초창기부터 많은 것들을 도와주시고 고생하신, 같이 긴 학위과정을 끝내 더 뜻깊은 장준호 박사님, 따듯한 마음과 신기한 능력을 가지신 홍정석 박사님, 항상 열심히 하시고 멋진 교수가 되실 최승우 박사님, 어려운 연구를 열심히 해내고 있는 박경도 연구원님, 4차원 적인 매력이 있는 동기 김정은 연구원님, 방장일로 고생이 많은 이무영 연구원님, 타지에서 연구하느라 고생이 많은 샘 연구원님, 조용조용하지만 열심히 연구에 정진하고 있는 최원일 연구원님, 많은 일들로 인해 고통받고 있지만 훌륭한 연구자가 될 조영인 연구원님, 엉뚱하지만 맡은 바 최선을 다하는 이창현 연구원님, 곧 석사 학위를 마치고 넓은 세계로 나아갈 김현재 연구원님, 많은 이야기를 나눠보지는 못했지만 더 멋지게 성장할 이준서, 유현지, 김정현, 구정우, 김경태 연구원님, 같이 연구실 생활을 했던 모든 분들에게 진심으로 감사한 마음을 전합니다. 앞으로 항상 좋은 일들이 있기를 바라고 훌륭한 연구를 통해 더욱 성장하기를 기원합니다.

무엇보다도 멀리 떨어져 있는 아들에게 항상 격려와 응원을 아끼지 않으신 부모님께 진심으로 감사드리며 사랑하는 마음을 보내드립니다. 두 분의 아낌없는 지원이 없었다면 이 학위 과정을 마칠 수 없었을 것입니다. 앞으로 더 멋진 인생을 펼쳐나갈 동생 원상이, 그리고 저를 위해 항상 기도하고 응원해주는 예지 누나께도 큰 감사를 드립니다. 떨어진 거리와 상관없이 저를 위해 마음 써 주시고 힘내라고 응원해주신 성진이, 울산 룸메이트들 면우, 광호 (진우), 혜성, 창현, 현재, 여러 친구분들께도 감사의 마음을 전합니다 정말 고맙고, 항상 행복하기를 바랍니다.

이렇게 많은 분들의 도움이 있어 이 학위 과정을 마칠 수 있었습니다. 이러한 도움이 빛날 수 있도록 앞으로도 멈추지 않고 연구에 정진하겠습니다. 다시 한 번 모든 분들께 진심으로 감사드립니다.

2023 년 8월

김령명